Forschungszentrum Karlsruhe
in der Helmholtz-Gemeinschaftt

Wissenschaftliche Berichte
FZKA 7241

Evaluation of ITER Design Criteria applied to RAFM Steels

Final Report
Tasks: TW2-TTMS-005b, D2 & TW5-TTMS-005, D8

R. Sunyk, J. Aktaa

Institut für Materialforschung
Programm Kernfusion
Association Forschungszentrum Karlsruhe/EURATOM

August 2006

Forschungszentrum Karlsruhe
in der Helmholtz-Gemeinschaft
Wissenschaftliche Berichte
FZKA 7241

Evaluation of ITER Design Criteria applied to RAFM Steels

Final Report
Tasks: TW2-TTMS-005b, D2 & TW5-TTMS-005, D8

Rudolf Sunyk, Jarir Aktaa

Institut für Materialforschung
Programm Kernfusion
Association Forschungszentrum Karlsruhe/EURATOM

Forschungszentrum Karlsruhe GmbH, Karlsruhe
2006

This work, supported by the European Communities under the contract of Association between EURATOM and Forschungszentrum Karlsruhe, was carried out within the framework of the European Fusion Development Agreement.
The views and opinions expressed herein do not necessarily reflect those of the European Commission.

Forschungszentrum Karlsruhe GmbH
Postfach 3640, 76021 Karlsruhe

Mitglied der Hermann von Helmholtz-Gemeinschaft
Deutscher Forschungszentren (HGF)

ISSN 0947-8620

urn:nbn:de:0005-072415

Abstract

In the first line, the aim of the activity represented in this work is an application of two advanced material models to a simulation of the test blanket module (TBM) undergoing cyclic thermal and mechanical loadings. The first model is thereby the ABAQUS standard combined non-linear isotropic-kinematic hardening model whereas the second is a viscoplastic material model considering material damage and being newly implemented as an ABAQUS user material (UMAT).

Material parameters for both models are adjusted using results of isothermal tensile and cyclic experiments performed at Forschungszentrum Karlsruhe GmbH (FZK) on EUROFER 97. As is generally known, EUROFER 97 is an important blanket material for the future fusion reactor and belongs to reduced activation ferritic-martensitic steels (RAFM), which soften under cyclic loading in contrast to austenitic steels exhibiting cyclic hardening.

Moreover, the work is focused on the application of some existing design rules considered for austenitic steels and further evaluation of the rules by comparison of their predictions with results of cyclic simulations using the advanced material models mentioned above. Thereby, some important allowable stress limits are calculated under consideration of the cyclic softening of RAFM.

Finally, new considerations concerning a mock-up experiment allowing to verify the advanced material models used in the present work and to assess a capability of the actual TBM design are represented here.

key words: blanket; test blanket module; reduced activation; ferritic-martensitic steel; EUROFER 97; structural design code; cyclic softening; stress categorization; ratcheting; high-temperature design rules; fatigue; first wall materials

Überprüfung der Rechmässigkeit der Verwendung von ITER-Designregeln bei Auslegung von Bauteilen aus RAFM-Stählen.

Zusammenfassung

Die in dieser Arbeit präsentierte Aktivität ist ausgerichtet auf die Anwendung von zwei recht komplizierten Materialmodellen an die Simulation vom Testblanketmodul unter der Einwirkung von thermischen und mechanischen Lasten. Das erste Modell ist dabei ein standardmässiges kombiniertes nichtlineares isotropisch-kinematisches Verfestigungsmodell aus der ABAQUS-Bibliothek, während das Andere ein gekoppeltes viskoplastisches Deformation/Schädigungsmodell ist, das als ein anwenderdefiniertes Material (UMAT) in ABAQUS implementiert wurde.

Die Materialparameter für beide Modelle wurden aufgrund von Experimentaldaten aus den isothermischen zyklischen Zugversuchen angefittet, die bei verschiedenen Temperaturen am Forschungszentrum Karlsruhe GmbH (FZK) an EUROFER 97 durchgeführt wurden. Es ist allgemein bekannt, dass der Stahl EUROFER 97 ein wichtiges Material für die erste Wand der zukünftigen Fusionsreaktoren konzipiert wurde. Dieses Material gehört zu den so genannten niedrigaktivierenden ferritisch-martensitischen Stählen (RAFM), die im Gegensatz zu den austenitischen Stählen eine zyklische Entfestigung aufweisen.

Weiterhin ist diese Arbeit schwerpunktmässig auf den Einsatz von einigen existierenden Designregeln fokussiert, die ursprünglich für austenitische Stähle formuliert wurden. Die ausgewählten Regeln sollen dabei evaluiert werden, indem ihre Aussagen mit den Ergebnissen der zyklischen Simulation unter Verwendung der o.g. Materialmodelle verglichen werden. Nebenbei sind auch einige wichtige zulässige Spannungsintensitäten unter Berücksichtigung der zyklischen Entfestigung von RAFM hergeleitet worden.

Ein Mock-Up-Experiment soll für die Zwecke der Verifizierung der verwendeten Materialmodelle sowie der Bewertung der Tauglichkeit der vorgeschlagenen TBM-Designs dienen. Neue Überlegungen bezüglich eines solchen Mock-Up-Experiments sind auch in dieser Arbeit dargestellt.

key words: blanket; test blanket module; reduced activation; ferritic-martensitic steel; EUROFER 97; structural design code; cyclic softening; stress categorization; ratcheting; high-temperature design rules; fatigue; first wall materials

Contents

Chapter 1

Introduction

This work is a part of the development activity of the ITER test blanket module (TBM). A determination of high-temperature design rules considering creep-fatigue is the final aim of this activity. According to the present-day vision, the TBM should be manufactured from a reduced-activation ferritic-martensitic (RAFM) steel EUROFER 97, which exhibits severe softening during cyclic loading, in contrast to austenitic steels. This abnormal behavior leads to a necessity to revise the traditional formulation of some important design rules, especially related to the protection against the C-type damage such as the well-known $3S_m$ rule.

Such a revision requests, firstly, a wide experimental data base and, secondly, an advanced material model able to describe the realistic behavior of the material. The fulfillment of both these requirements as well as acute needs of blanket designers for renewed rules thus form positive initial conditions for the appearance of the work presented. We have recently reported the results of first simulations using the advanced materials models, see Sunyk & Aktaa [14, 13].

The report is structured as follows. Firstly, we give a detailed description of material models used for simulations and represent the original experimental data using to adjust unknown material parameters. Then, we represent the 2D discretized finite element model of TBM and results of thermal simulations being performed to obtain temperature distributions in the model depending on the plasma heating as well as the temperature in cooling channels. After this, we investigate conditions causing an appearance of any inelastic response in the structure after the 1^{st} operating cycle. In the next chapter, we discuss a behavior of TBM during first 600 operating cycles simulated using both material models. In the following chapter, we calculate some important stress intensity limits under consideration of the material softening mentioned above, verify some important design rules according to SDC-IC [1] and compare predictions of the rules with results of the cyclic simulations performed separately. Finally, we represent our considerations concerning a mock-up experiment, which would allow to verify the advanced material models used in the present work and to assess a capability of the actual TBM design. Numerous additional illustrations and diagrams are placed in appendix.

Chapter 2

Material Models

To simulate a realistic behavior of the TBM, two different material models have been used in the finite element simulations: the standard combined non-linear isotropic-kinematic hardening model, see ABAQUS user's manual [2] ch. 11.2.2, and a viscoplastic material model accounting also for material damage and implemented as a user material subroutine (UMAT), see J. Aktaa & R. Schmitt [7].
Experimental data stemming from a life time study of the EUROFER 97 at $450°C$ $(723\,K)$, $550°C$ $(823\,K)$ and $650°C$ $(923\,K)$ performed by J. Aktaa & R. Schmitt [7] as well as at room temperature (RT) provided by M. Weick [16] have been used to adjust material parameters required for both material models. Some chosen cycles recorded at $650°C$ $(923\,K)$ during isothermal uniaxial tensile tests with the predefined total strain of 1.5% are depicted in fig. 2.1 on the left-hand side. Thereby, the material softening cycle by cycle is evident. The decrease of the maximum tensile stress with the increasing accumulated plastic strain is shown also in fig. 2.1, on the right.

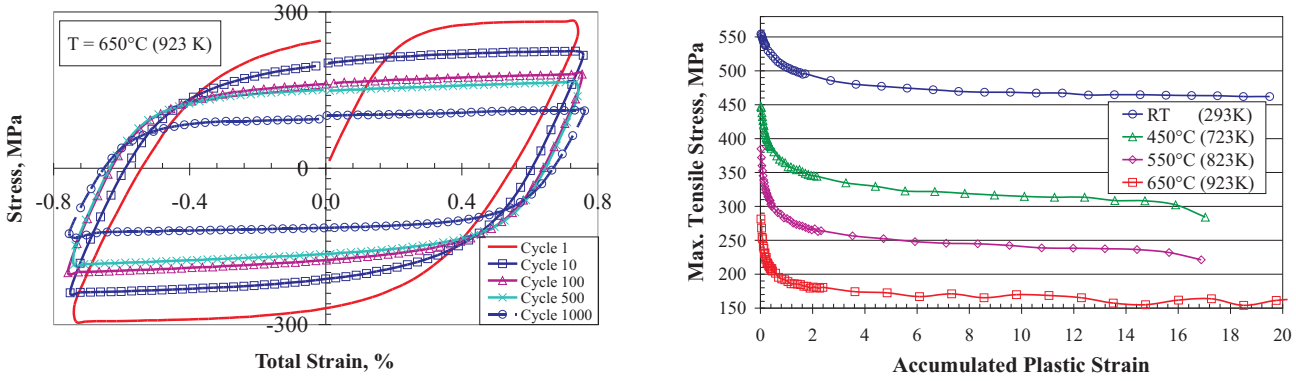

Figure 2.1: Results of isothermal uniaxial tensile tests: chosen cycles recorded at $650°C$ $(923\,K)$ (on the left) and the maximum tensile stress as a function of the accumulated plastic deformation (on the right).

2.1 ABAQUS Standard Combined Hardening Model

For the metals subjected to cyclic loading, ABAQUS provided a non-linear isotropic-kinematic hardening model. This model is able to account e.g. for the Bauschinger effect, cyclic hardening/softening with plastic shakedown, as well as for ratcheting. Here, we give a short description of the model based on the ABAQUS manual cited above.

2.1.1 Theoretical Background

The total strain rate can be decomposed into the elastic, plastic and thermal strain rates:

$$\dot{\boldsymbol{\epsilon}}^{tot} \doteq \dot{\boldsymbol{\epsilon}}^{el} + \dot{\boldsymbol{\epsilon}}^{pl} + \dot{\boldsymbol{\epsilon}}^{th} \,, \tag{2.1}$$

whereby the elastic part is captured within the linear elasticity as

$$\boldsymbol{\sigma} = \mathbb{E}^{el} : \boldsymbol{\epsilon}^{el} \tag{2.2}$$

and the thermal part is given by the following conventional expression:

$$\boldsymbol{\epsilon}^{th} = \alpha \, [T - T_0] \, \boldsymbol{I} \,. \tag{2.3}$$

Here, $\mathbb{E}^{el}$ denotes the elastic 4^{th}-order tangent operator, $\boldsymbol{I}$ is the identity tensor, T and T_0 are the current and the reference temperatures respectively; finally, α is the thermal extension coefficient. The yield condition is given in terms of the usual von Mises plasticity

$$f\left(\boldsymbol{\Sigma}\right) \doteq \sqrt{\frac{3}{2}\boldsymbol{\Sigma}^{dev} : \boldsymbol{\Sigma}^{dev}} = \sigma^0 \tag{2.4}$$

with the deviatoric part of the overstress $\boldsymbol{\Sigma}$ defined as

$$\boldsymbol{\Sigma} \doteq \boldsymbol{\sigma} - \boldsymbol{\Omega} \tag{2.5}$$

and the backstress or the kinematic shift $\boldsymbol{\Omega}$. The size of the elastic range is denoted as σ^0. The rate of plastic flow is given here by the associated plastic flow rule

$$\dot{\boldsymbol{\epsilon}}^{pl} = \dot{\bar{\epsilon}}^{pl} \, \frac{\partial \left[f\left(\boldsymbol{\Sigma}\right) - \sigma^0 \right]}{\partial \boldsymbol{\sigma}} \tag{2.6}$$

with the equivalent rate of plastic flow

$$\dot{\bar{\epsilon}}^{pl} \doteq \sqrt{\frac{2}{3}\dot{\boldsymbol{\epsilon}}^{pl} : \dot{\boldsymbol{\epsilon}}^{pl}} \,. \tag{2.7}$$

Equations (2.1) - (2.7) are common for a wide class of plasticity models. The model-specific assumptions concerning the evolution of hardening and based on the work of Lemaitre and Chaboche [11] are reviewed below. The size of the elastic range σ^0 is defined as a function of the equivalent plastic strain

$$\bar{\epsilon}^{pl} \doteq \sqrt{\frac{2}{3}\boldsymbol{\epsilon}^{pl} : \boldsymbol{\epsilon}^{pl}} \,,$$

temperature T and field variables f_i:

$$\sigma^0 \left(\bar{\epsilon}^{pl}, \, T, \, f_i \right) = \sigma|_0 + Q\left(T, \, f_i\right) \left[1 - e^{-b\left(T, \, f_i\right) \, \bar{\epsilon}^{pl}} \right] \tag{2.8}$$

with the yield surface size at zero plastic strain $\sigma|_0$ and material parameters Q and b, which should be adjusted using experimental data. Thereby, Q is the maximum change in the size of the yield surface and b defines the rate at which the size of the yield surface changes with the development of plastic straining.
The evolution of the kinematic component $\boldsymbol{\Omega}$ is given by a combination of the linear hardening Ziegler law, see Ziegler [17] [1], and the relaxation or dynamic recovery term $\gamma \, \boldsymbol{\Omega} \, \dot{\bar{\epsilon}}^{pl}$, which introduces the non-linearity:

$$\dot{\boldsymbol{\Omega}} = \frac{C}{\sigma^0} \, \dot{\bar{\epsilon}}^{pl} \, \boldsymbol{\Sigma} - \gamma \, \boldsymbol{\Omega} \, \dot{\bar{\epsilon}}^{pl} + \frac{1}{C} \, \boldsymbol{\Omega} \, \dot{C} \tag{2.9}$$

Here, the initial kinematic hardening modulus C and the rate of the decrease of the kinematic hardening modulus with the increasing plastic deformation γ should be calibrated again from cyclic tests. Note that in general C is a function of temperature and field variables. If this dependence on the field variables is omitted, the last term in (2.9) vanishes.

[1] Rice [12] generalized this law as $\dot{\boldsymbol{\Omega}} = \dot{\mu}[\boldsymbol{\sigma} - \boldsymbol{\Omega}] + h \, \boldsymbol{\Omega} \, \dot{T}$.

2.1.2 Adjustment of Material Parameters

Integration of (2.9) over a half cycle yields the following expression:

$$\Omega = \frac{C}{\gamma}\left[1 - e^{\gamma\,\bar{\epsilon}^{pl}}\right] . \tag{2.10}$$

Parameters C and γ for the kinematic part of the hardening can be determined by fitting of this expression to $1/4$ of the first cycle, see fig. 2.2, on the left. Other two parameters Q and b defining the isotropic hardening should be determined by fitting of (2.8) to the overstress curves represented as functions of the accumulated plastic strain, see fig. 2.2, on the right. The determined values are collected in table A.1, see appendix A.1. To

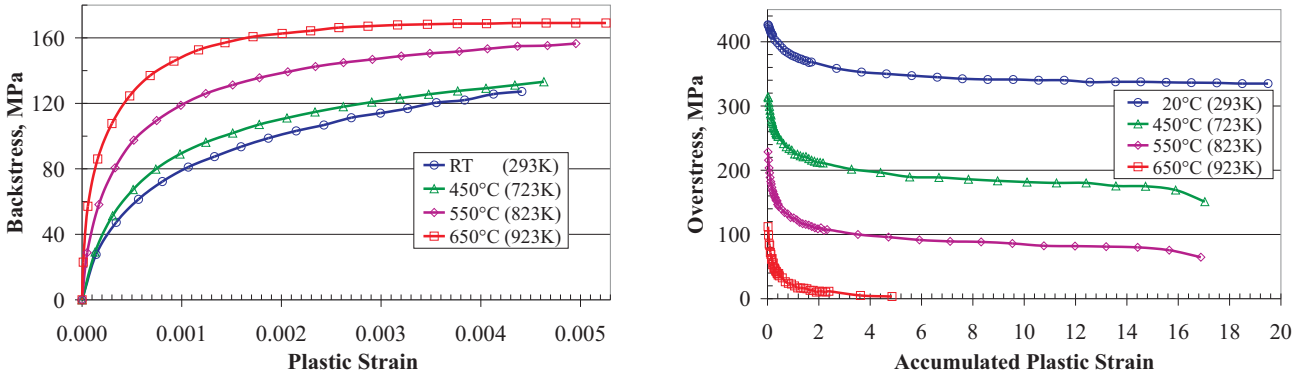

Figure 2.2: Experimental data used to determine model parameters: $1/4$ of the first cycle (on the left) for the kinematic hardening and the overstress as a function of the accumulated plastic strain for the isotropic hardening at four different temperatures.

verify the adjusted parameters, a strain-controlled cyclic test has been simulated at three different temperatures using a simple 2D finite element (FE) model depicted in fig. 2.3. Thereby, the total strain range has been set to 1.5%. Results of the simulation shown evidently a very good agreement with the experimental data.

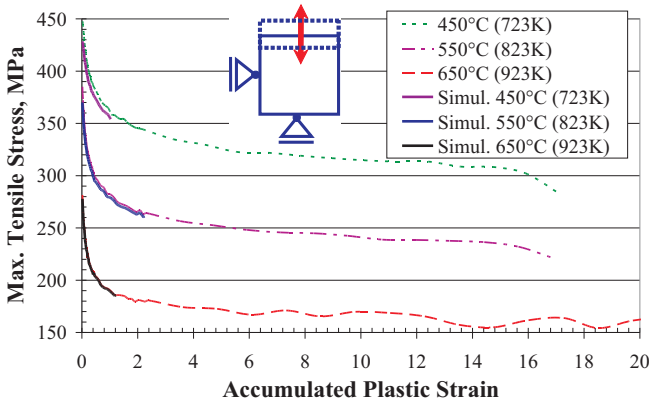

Figure 2.3: Verification of the material parameters by FE simulation.

2.2 A Coupled Viscoplastic Material Model

A usual operating mode of ITER contains hold times at high temperatures (HT), which should be significant for a formation of creep-induced defects in the TBM. The proposed viscoplastic model combines a deformation model suitable to describe the undamaged material and a damage model to describe the material behavior up to the failure. Thereby, the failure of a material point is defined by the macro crack initiation at that point, i.e. the life time covers the time needed for micro crack initiation and its propagation up to a macro crack.

2.2.1 Theoretical Background

To describe damage, a simplified version of the ISRM (inelastic strain rate modified) model used by Aktaa and Schinke [6] has been applied in the present work. The simplification is based on the assumption using experimental observations that damage accumulates linearly under varying loading. The ISRM model has been applied successfully to numerous simulation of metallic alloys at HT also in a post-irradiated state , see e.g. Aktaa and Schinke [6] and Aktaa et al. [4]. The model is thus capable to describe creep, fatigue as well as the creep-fatigue interaction. In the simplified ISRM model, the evolution of the internal state variable $\mathcal{D}$ describing damage and ranges between 0 for the undamaged material and 1 for the totally damaged material is given by the following expression, see Aktaa et al. [4]:

$$\dot{\mathcal{D}} = \left\langle \frac{\chi(\boldsymbol{\sigma})}{A} \right\rangle^{r} \dot{\bar{\epsilon}}^{in} \, [1-\mathcal{D}]^{-\kappa} \tag{2.11}$$

with the unknown damage parameters A, r and κ and the equivalent rate of inelastic flow $\dot{\bar{\epsilon}}^{in}$ defined as in (2.7). $\chi(\boldsymbol{\sigma})$ is thereby given by the following expression:

$$\chi(\boldsymbol{\sigma}) \doteq \alpha_1 \, \sigma_I + \alpha_2 \, \boldsymbol{\sigma} : \boldsymbol{I} + [1-\alpha_1-\alpha_2] \, \sigma_{eq} \tag{2.12}$$

with the maximum principal stress σ_I, the equivalent von Mises stress

$$\sigma_{eq} \doteq \sqrt{\frac{3}{2} \, \boldsymbol{\sigma}^{dev} : \boldsymbol{\sigma}^{dev}}$$

and two additional material parameters α_1 and α_2. Here, $\boldsymbol{\sigma}^{dev}$ is the deviatoric part of the stress tensor $\boldsymbol{\sigma}$. The brackets $\langle\,\rangle$ denote that damage does not vary if $\chi(\boldsymbol{\sigma})$ becomes negative. Finally, damage remains constant if no inelastic deformation occurs.

Within the continuum damage mechanics approach, deformation and damage can be coupled by substitution of the stress $\boldsymbol{\sigma}$ by an effective stress $\tilde{\boldsymbol{\sigma}}$. Both tensors are connected by the following expression, see Lemaitre [10]:

$$\tilde{\boldsymbol{\sigma}} = \frac{\boldsymbol{\sigma}}{1-\mathcal{D}} \, . \tag{2.13}$$

The elastic-viscoplastic material model proposed is the model of Chaboche [8] with a modification capturing the complex cyclic softening behavior of RAFM, see Aktaa & Schmidt [7]. The model belongs to the so called unified deformation models describing viscoplasticity without the separation into the time-dependent creep and the time-independent plasticity, see Walker [15], so that $\dot{\boldsymbol{\epsilon}}^{pl}$ should be substituted by $\dot{\boldsymbol{\epsilon}}^{in}$ in (2.1). Under consideration of damage, the elasticity law (2.2) can be rewritten as

$$\boldsymbol{\sigma} = [1-\mathcal{D}] \, \mathbb{E}^{el} : \boldsymbol{\epsilon}^{el} \tag{2.14}$$

In general, equations (2.3) and (2.4) remain unchanged. However, the overstress $\boldsymbol{\Sigma}$ in (2.4) has another definition than in (2.5):

$$\boldsymbol{\Sigma} \doteq \frac{\boldsymbol{\sigma}}{\psi \, [1-\mathcal{D}]} - \boldsymbol{\Omega} \tag{2.15}$$

with the isotropic softening variable ψ described below. The following flow rule is used within the model instead of (2.6):

$$\dot{\boldsymbol{\epsilon}}^{in} = \frac{3}{2} \left\langle \frac{f\,(\boldsymbol{\Sigma}) - \sigma^0}{Z} \right\rangle^{n} \frac{\boldsymbol{\Sigma}}{f\,(\boldsymbol{\Sigma})} \tag{2.16}$$

with the unknown material parameters Z and n [2]. The isotropic softening variable ψ is subdivided into two parts ψ_1 and ψ_2 allowing a description of the non-saturating part and the non-linear part of the cyclic softening respectively:

$$\psi \doteq \psi_1 + \psi_2 \;\; : \quad \psi_1|_{t=0} = 0 \quad \text{and} \quad \psi_2|_{t=0} = 1 \tag{2.17}$$

[2] The operator $\langle\,\rangle$ is defined as follows: $\langle x \rangle \doteq [\, x + |x| \,]/2$

The change of each part is given by a separate evolution equation:

$$\dot{\psi}_1 = -h\,\dot{\bar{\epsilon}}^{in} \tag{2.18}$$

$$\dot{\psi}_2 = c\,[\psi_s - \psi_2]\;\dot{\bar{\epsilon}}^{in} - r_\psi\;|\psi_2 - \psi_r|^{m_\psi - 1}\;[\psi_2 - \psi_r] \tag{2.19}$$

with

$$\psi_s \doteq 1 - \psi_{s,\infty}\left[1 - e^{-c_s \max\limits_{-\infty<\tau<t} \bar{\epsilon}^{in}(\tau)}\right] \tag{2.20}$$

to capture the memorized increase of the cyclic softening capacity with increasing amplitude of inelastic strain, the equivalent inelastic strain

$$\bar{\epsilon}^{in}(\tau) \doteq \sqrt{\frac{2}{3}\boldsymbol{\epsilon}^{in}(\tau) : \boldsymbol{\epsilon}^{in}(\tau)}$$

and seven material parameters: h, c, ψ_r, $\psi_{s,\infty}$, r_ψ, m_ψ, c_s.
Finally, the change of the kinematic hardening is described by an appropriate evolution equation, cf. (2.9):

$$\dot{\boldsymbol{\Omega}} = \frac{2}{3}\,H\,\dot{\boldsymbol{\epsilon}}^{in} - D\,\boldsymbol{\Omega}\,\dot{\bar{\epsilon}}^{in} - R\left[\frac{3}{2}\boldsymbol{\Omega} : \boldsymbol{\Omega}\right]^{[m-1]/2}\boldsymbol{\Omega} \tag{2.21}$$

with the new unknown parameters R, D, H and m. Last terms in (2.19) and (2.21) represent static recoveries of the isotropic softening and the kinematic hardening respectively, which could be observed under creep, relaxation or a cyclic loading with a hold time.

2.2.2 Adjustment of Material Parameters

For the determination of the set of material parameters, they have been subdivided into several subsets. Thereby, members of each subset exhibit a strong correlation with respect to (wrt.) each other and cannot be determined separately. A stepwise identification of parameters is performed by a minimization of the error between the model and the material response using the following error function, see Aktaa [3]:

$$\chi^2 = \sum_{m=1}^{n_{exp}} \sum_{n=1}^{n_{dat\,m}} \left[\frac{\sigma_{mn}^{model} - \sigma_{mn}^{experiment}}{n_{dat,\,m}}\right]^2 \tag{2.22}$$

with a number of experiments for each subset n_{exp} and a number of data points from the experiment m used for the fitting. The optimization code MINUIT from the CERNLIB has been used.
The parameter identification has been performed according to the strategy presented above in the following order [3]:

step 1 determine parameters k, Z, n, H and D by fitting the model response to the first cycles (stress-strain curves) of the LCF tests without and with the hold time; thereby other parameters have been set to negligible values and fixed;

step 2 determine parameters R and m by fitting the model response to the stationary creep rates data; the parameters k, Z, n, H and D are thereby set to their values adjusted during the step 1; other parameters remain fixed at negligible levels;

step 3 determine parameters h, c, $\psi_{s,\infty}$ and c_s by fitting of the model response to the cyclic softening curves (peak stress vs. number of cycle) of the LCF tests without the hold time up to the half failure time; thereby all already determined parameters are set to their values adjusted during the step 1 and 2 whereas other parameters remain fixed at negligible levels;

[3] Initial values have been estimated on the basis of experience and first assessments of experimental data.

step 4 determine parameters r_ψ, ψ_r and m_ψ by fitting of the model response to the cyclic softening curves of the LCF tests with hold times up to the half failure time; other parameters are handled as in the previous steps;

step 5 determine parameters A, r and κ by fitting of the model response to the cyclic softening curves of the LCF tests without hold times up to the failure time; other parameters are handled as in the previous steps.

Parameters determined for the EUROFER 97 at $450°C$ $(723\,K)$ and $550°C$ $(823\,K)$ as well as for F82H at $450°C$ $(723\,K)$, $550°C$ $(823\,K)$ and $650°C$ $(923\,K)$ according to the procedure described above are listed in appendix A.1.

Fig. 2.4 demonstrates the quality of the adjustment for EUROFER 97 [4]. Indeed, the stress-strain behavior within the first cycle can be quite well captured by the model for different total strain ranges, see fig. 2.4, on the left. On the other hand, the complex softening behavior is also well described by the model, see fig. 2.4, on the right.

A good agreement between the simulation and experiment can also be achieved for the damage (lifetime) behavior, see fig. 2.5. The differences between the calculated and measured lifetimes lie within a range of factor two except for the tests with the lifetime lying in the transition range to the high cycle fatigue (HCF), see fig. 2.5, on the right. In the HCF regime, the ISRM damage model is expected to underestimate the lifetime, see also Aktaa & Munz [5], and is however a conservative save prediction.

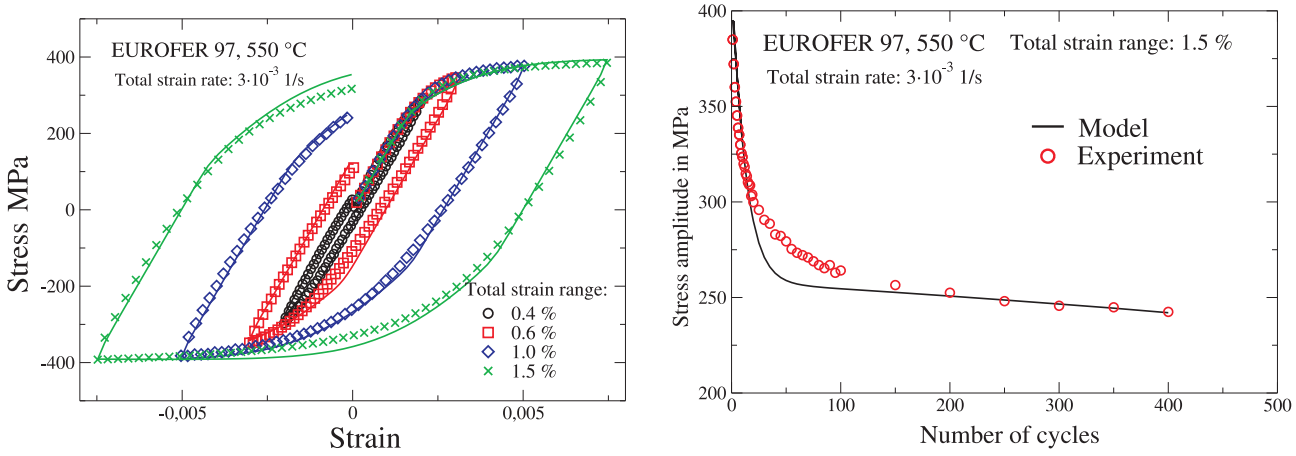

Figure 2.4: Comparison between material (markers) and model (line) responses for the stress-strain hysteresis for different strain ranges (on the left) and for the variation of the stress amplitude with the increasing number of cycles (on the right) of a strain-controlled LCF tests.

[4] For more plots we refer to the report [7].

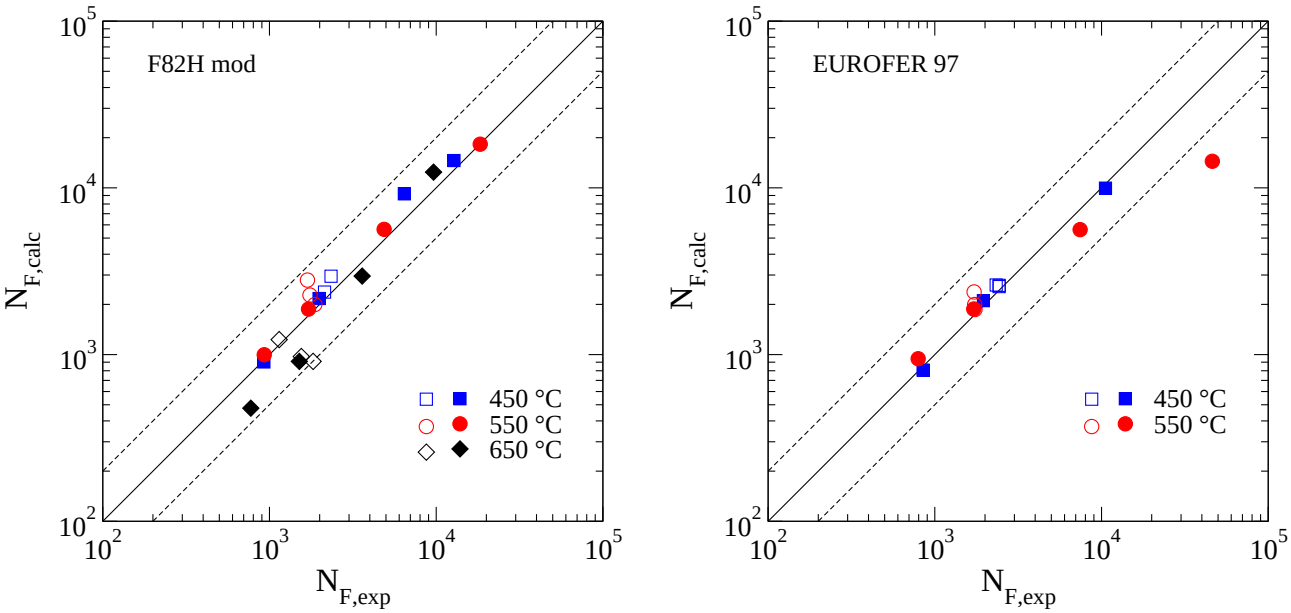

Figure 2.5: Comparison between numbers of cycles to failure calculated using the coupled deformation-damage model with those determined experimentally for F82H (on the left) and EUROFER 97 (on the right) during LCF tests without (solid symbols) and with the hold time (open symbols).

Chapter 3

Determination of the Elastic Limit

3.1 Finite Element Model

To verify the material model described above, a 2D model of a quarter of the TBM has been created according to the current design and meshed using PATRAN. The model is shown in fig. 3.1 together with mechanical constraints (symmetry boundary conditions). The only external mechanical load in the non-accident operating mode is the hydrostatic pressure of $80bar = 8MPa$ in all cooling channels.
First simulations using plain strain elements CPE8 have exhibited non-physically high out-of-plane stresses, which have a numerical source. For those simulations where thermal stresses occur, ABAQUS provides a so called generalized plane strain element formulation, which accounts for an elongation in the out-of-plane direction and thus avoids enormously high non-physical out-of-plane stresses , see ABAQUS user's manual [2] ch. 13.1.2. The 8-node generalized plane strain elements CPEG8 have been used here for this reason.

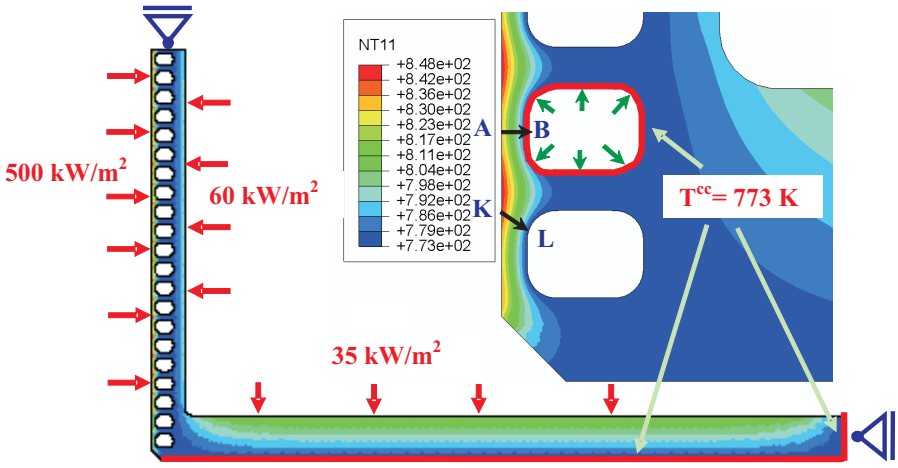

Figure 3.1: The FE model of the TBM with mechanical and thermal constraints and loadings; the represented temperature distribution (K) is due to the depicted thermal constraints and loads; the paths AB and KL are used for the stress categorization as described below.

3.2 Thermal Simulation

During the operating mode, the model should account for a heat flux of 250 up to 500 kW/m^2 (peak) on the plasma-facing side as well as a heat flux of 60 kW/m^2 and of 35 kW/m^2 on the vertical and horizontal interior respectively due to breeder units, see fig. 3.1. For reason of simplicity, temperature boundary conditions

depicted in fig. 3.1 have been considered in the simulations. [1]
In order to determine acceptable loads, the behavior of the TBM should be simulated under consideration of different temperature distributions. To obtain such distributions, thermal simulation has been performed for four values of plasma heating: $250\ kW/m^2$ (the usual operating mode), $500\ kW/m^2$, $750\ kW/m^2$ and $1000\ kW/m^2$, as well as for three different temperatures in the cooling channels (T^{cc}): $673\ K$, $773\ K$ and $873\ K$. The heating due to the breeder unit remains thereby constant. Results of a thermal computation for the plasma heating of $500\ kW/m^2$ and $T^{cc} = 773\ K$ are shown also in fig. 3.1 as an example of the typical temperature distribution with the constant temperature in the cooling channels.

3.3 Mechanical Simulations using various Plasma Heating and Pressure in Cooling Channels (no cycling)

By variation of both the temperature in cooling channels and plasma heating, a critical pressure has been determined using both material models. The critical pressure is thereby defined as the minimum pressure causing any inelastic deformation after the first heating i.e. after half of the first cycle for the ABAQUS-own material model and after the whole first cycle for the viscoplastic material model.
The critical pressure is shown in fig. 3.2 for both material models as a function of the plasma heating and the temperature in the cooling channels T^{cc}. Evidently, the critical pressure is strongly dependent on the tempera-

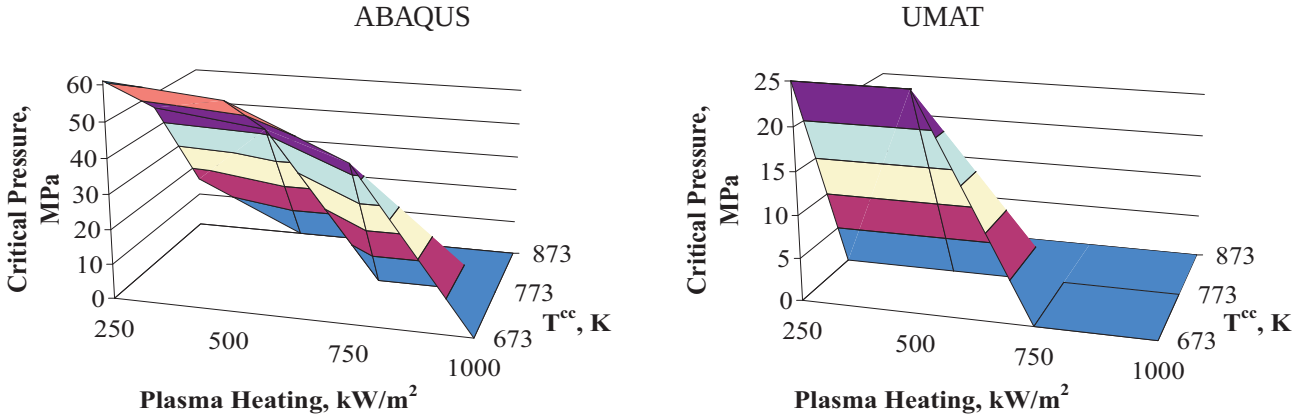

Figure 3.2: The critical pressure as a function of plasma heating and the temperature in cooling channels obtained using the ABAQUS-own material model (on the left) and the UMAT (on the right).

ture in the cooling channels and relatively slightly on plasma heating up to $450 - 500\ kW/m^2$ approximately. Increasing plasma heating takes however a leading influence on the critical pressure whereas the temperature in the cooling channels plays a decreasing role and, finally, plastic deformation occurs for all T^{cc} without pressure due to the temperature gradient alone if plasma heating reaches approximately $750\ kW/m^2$ or $1000\ kW/m^2$ for the UMAT and the ABAQUS-own material model respectively.
For this heating, plastic deformation is localized in a narrow band along the plasma-facing side, see fig. 3.3 (on the left). A high pressure causes an additional plastic deformation located in a left bottom or left top corners of the 1^{st} or 2^{nd} cooling channels if the pressure in the channels reaches a critical value discussed above, see fig. 3.3 (on the right). The magnitude of the pressure-induced plastic strain becomes thereby higher than the magnitude of the pure thermal plastic strain.
With the aim of better understanding, the data are also presented in diverse 2D plots. For instance, fig. 3.4 shows the critical pressure depending on plasma heating for different temperatures in the cooling channels obtained using both material models.

[1] In the reality, the temperature distribution in the cooling channels is not homogeneous; the inhomogeneity can cause additional temperature gradients, see section 6. However, the consideration of the phenomenon is a challenge for further simulations.

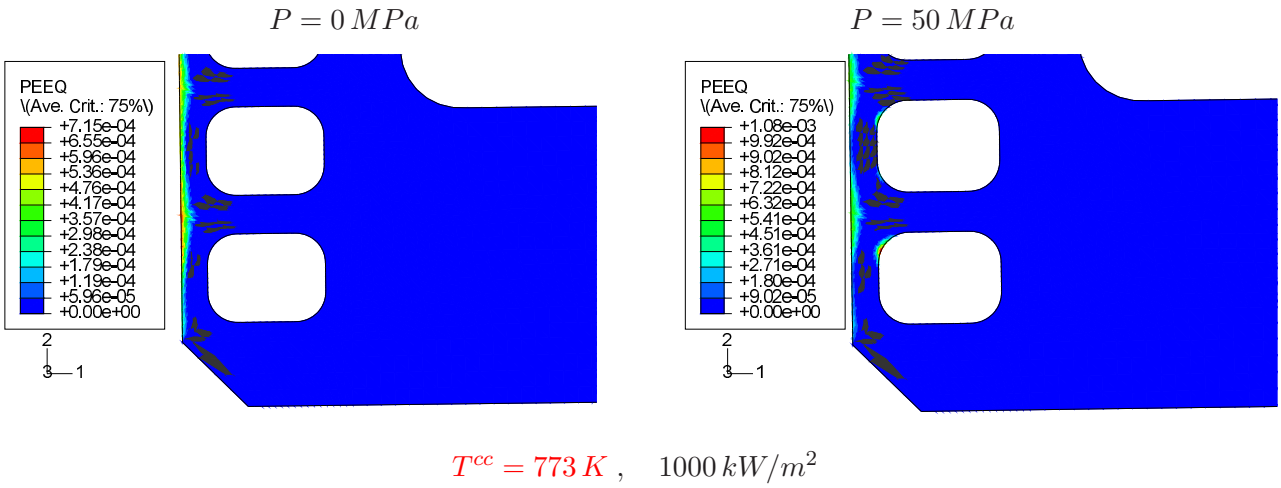

Figure 3.3: Distribution of the equivalent plastic strain in the most loaded region of the TBM for plasma heating of $1000\ kW/m^2$ at $T^{cc} = 773\,K$ in the absence of pressure (on the left) and at the pressure of $50\,MPa$ obtained using the ABAQUS-own model.

Another cross-section of the 3D plot in fig. 3.2 is shown in fig. 3.5. Here, the critical pressure is plotted as functions of T^{cc} for different values of plasma heating. The plots confirm the proposition about the slight dependence of the critical pressure on plasma heating up to approx. $500\ kW/m^2$.
3D plots in fig. 3.6 illustrate the maximum von Mises stress in the model corresponding to the critical pressure again as a function of plasma heating and T^{cc}; figs. 3.7 and 3.8 represent 2D cross-sections of these plots. Evidently, the user-defined material model (UMAT) leads to lower values of the maximum stress due to relaxation during hold times. Diagrams in fig. 3.7 show a dominant influence of plasma heating on the maximum von Mises stress for high values of plasma heating (at least from $750\,kW/m^2$. The UMAT yield even an absolute independency of the maximum von Mises stress from T^{cc} for $T^{cc} \geq 773\,K$, see additionally the right-hand side diagram in fig. 3.8. Furthermore, both diagrams in fig. 3.8 show that the critical von Mises stress corresponding to $1000\,kW/m^2$ changes in a relatively narrow band. It means that T^{cc} plays a secondary role in this case. This proposition concerns also the case of $750\,kW/m^2$ computed using the UMAT.
The UMAT leads evidently to more conservative results, which should be probably more correct due to taking into account of a high-temperature creep.
The maximum von-Mises stress as a function of T^{cc} is shown in fig. 3.9 at the constant pressure of $8\,MPa$ corresponding to the usual operating mode and for different values of plasma heating. Except for $1000\,kW/m^2$, the maximum von Mises stress depends rather on plasma heating and is almost non-sensitive to the variation of T^{cc} at this pressure. Note that both models lead thereby to quantitatively well comparable results.
This particular result can however be generalized using the following plots: the maximum von-Mises stress vs. the pressure in cooling channels for different T^{cc} represented separately for each value of plasma heating, see fig. A.1 in appendix A.2. It is easy to see that, except for $750\,kW/m^2$ and $1000\,kW/m^2$, the von Mises stress remains independent of T^{cc} and is controlled by the pressure in cooling channels up to a pressure, which is characteristic for each value of plasma heating. This characteristic pressure decreases with the increasing plasma heating and remains higher than $8\,MPa$ up to $500\,kW/m^2$. Both models lead to quantitatively similar results for $T^{cc} \geq 773\,K$ and heating values up to at least $500\,kW/m^2$. Simulations with a higher plasma heating exhibit however a dependency on a material model.
To illustrate the plots presented, we give some contour plots of the distribution of the von Mises stress over a most loaded region in the model. These plots are intended to show, how the pressure influences the stress distribution and also to detect critical regions where the von-Mises stress becomes maximum and causes plastic deformation. For instance, fig. 3.10 illustrates a distribution of the von Mises stress corresponding to the critical pressure at $T^{cc} = 773\,K$ under consideration of plasma heating of $250\,kW/m^2$ (on the left) and $1000\,kW/m^2$,

see also the 3D plot on the left-hand side in fig. 3.2.
As shown in the left-hand side in fig. A.2 in appendix A.3 , plasma heating without the pressure causes a high equivalent stress along the plasma-faced side. The value of this stress is strongly dependent on plasma heating. On the other hand, an overlaying of the pressure leads to a shift of the highest loaded area to corners of the cooling channels, see fig. A.2, the right-hand side. The dependency of the maximum values on the heating becomes thereby not as strong as if the pressure is absent.

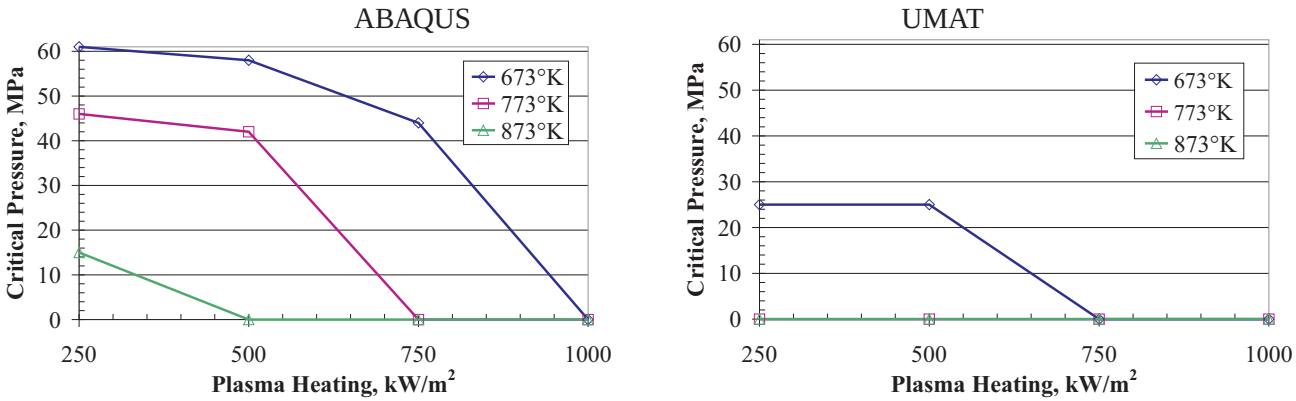

Figure 3.4: The critical pressure as a function of plasma heating for different temperatures in cooling channels obtained using the ABAQUS standard model (on the left) and the coupled deformation-damage model.

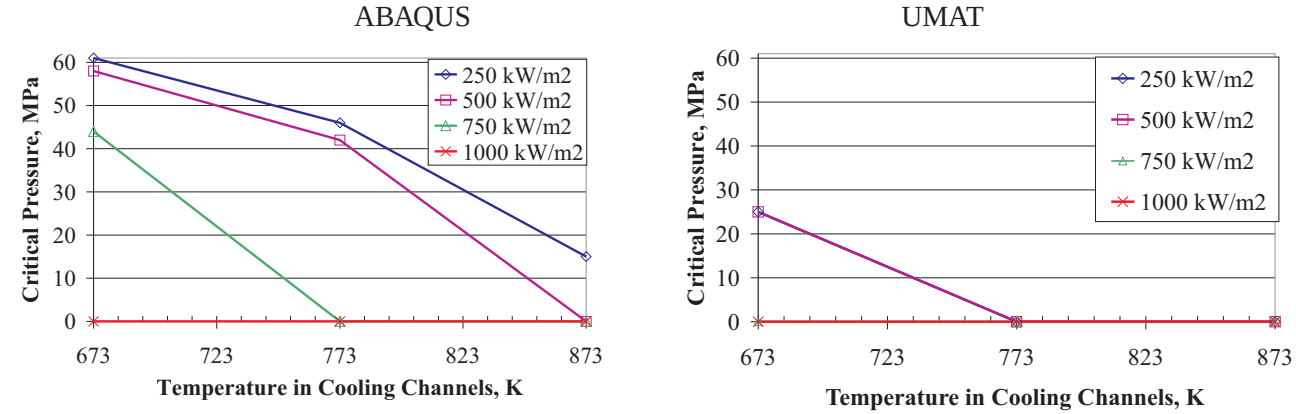

Figure 3.5: The critical pressure as a function of the temperature in cooling channels for different values of plasma heating obtained using the ABAQUS standard model (on the left) and the coupled deformation-damage model.

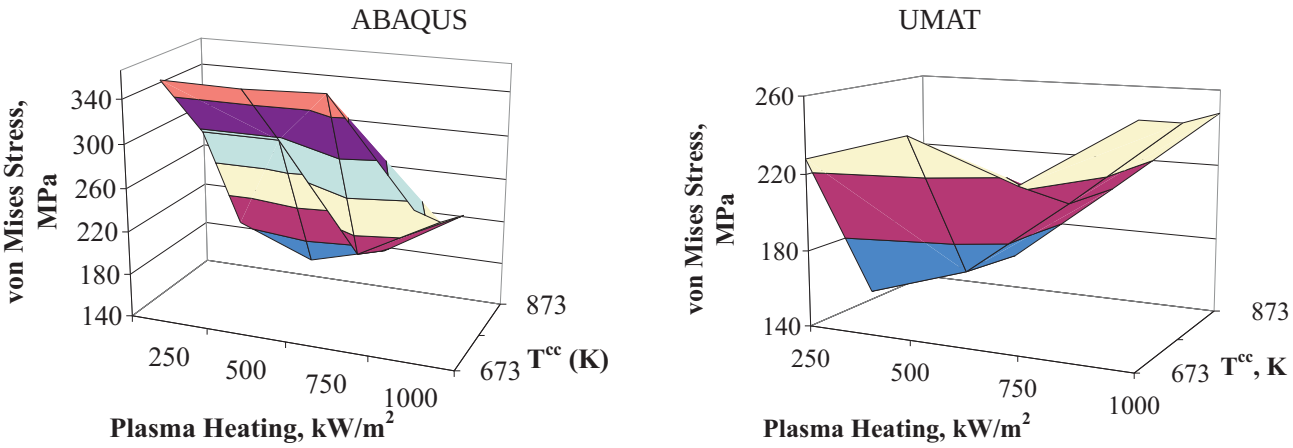

Figure 3.6: The corresponding maximum von Mises stress as a function of plasma heating and the temperature in cooling channels obtained using the ABAQUS-own material model (on the left) and the UMAT.

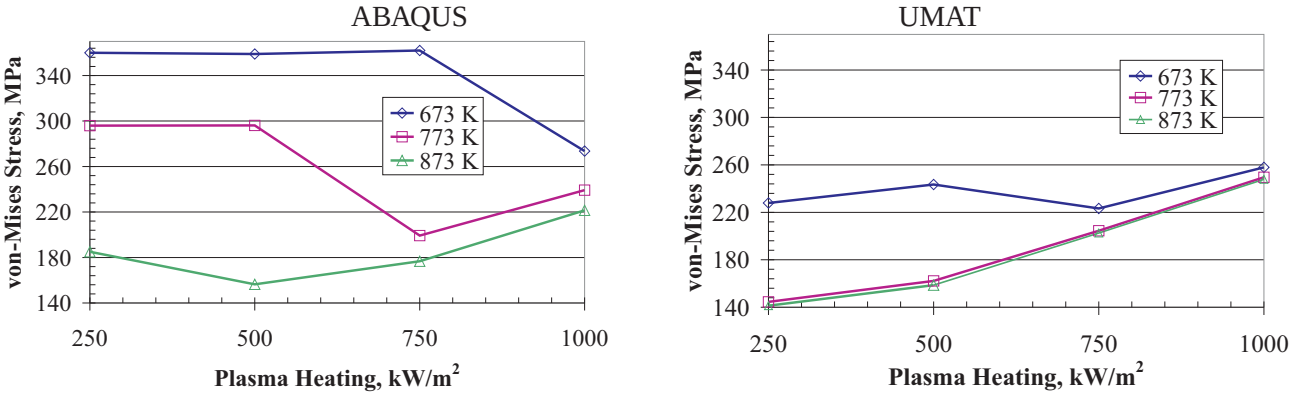

Figure 3.7: The maximum von Mises stress corresponding to the critical pressure as a function of plasma heating for different temperatures in cooling channels obtained using the ABAQUS standard model (on the left) and the coupled deformation-damage model.

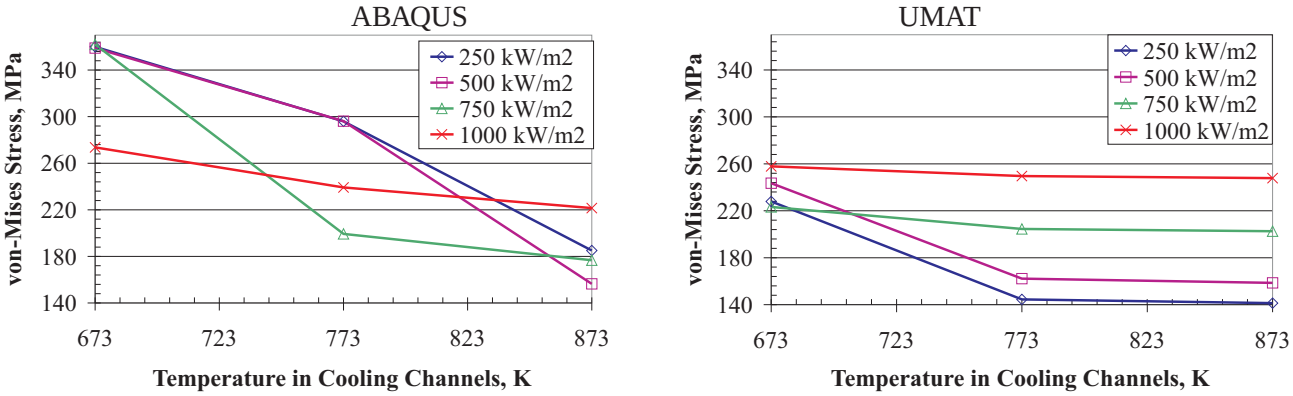

Figure 3.8: The maximum von Mises stress corresponding to the critical pressure as a function of the temperature in cooling channels obtained using the ABAQUS standard material model (on the left) and the coupled deformation-damage model for different values of plasma heating.

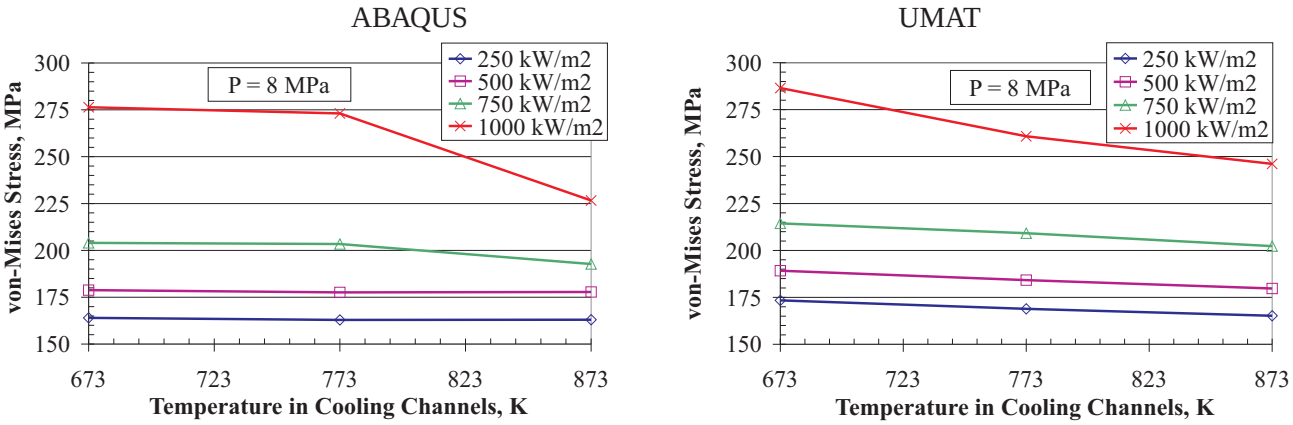

Figure 3.9: The maximum von-Mises stress as a function of the temperature in cooling channels obtained using the ABAQUS standard material model (on the left) and the UMAT for different values of plasma heating at the constant pressure of $8\,MPa$.

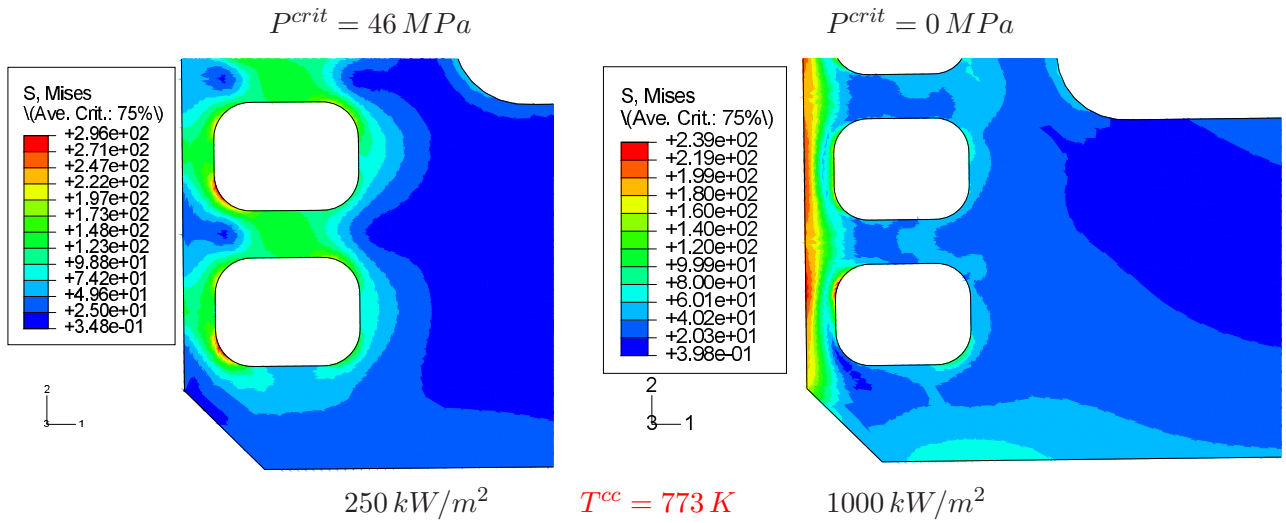

Figure 3.10: distribution of the von Mises stress corresponding to the critical pressure at $T^{cc} = 773\,K$ under consideration of plasma heating of $250\,kW/m^2$ (on the left) and $1000\,kW/m^2$.

Chapter 4

Simulations of the Cyclic Behavior of TBM

The cyclic behavior of the TBM model has been studied again using both the ABAQUS-own material model described above and the UMAT. Thereby, the following load case has been considered: $T^{cc} = 600° C\ (873\,K)$; the plasma heating $750\,kW/m^2$ and the coolant pressure $P = 50\,MPa\ (500\,bar)$. It was assumed on the basis of the study reported in the previous section that such abnormal high loads should cause an important amount of inelastic deformation.
Each cycle consists of four steps: (1) heating and application of the pressure, $30\,sec$; (2) holding at the high temperature (HT), $400\,sec$, (3) cooling to RT, $100\,sec$ and, finally (4) holding at RT for $1400\,sec$. Note that steps (2) and (4) are not relevant for the ABAQUS-own time-independent material model.
We have simulated a few hundred cycles using both material models (300 with the ABAQUS-own material

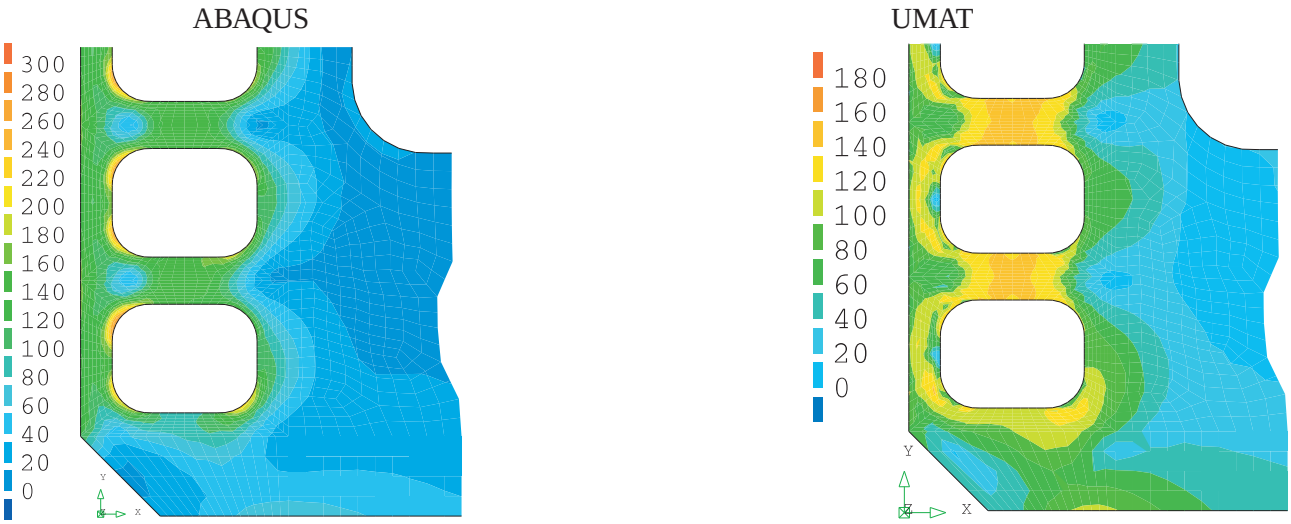

$\sigma_{vm}^{max} = 287\,MPa$ $\sigma_{vm}^{max} = 154\,MPa$

Figure 4.1: A distribution of the von Mises stress after the heating within the cycle 300 obtained using the ABAQUS standard material model (on the left) as well as the UMAT under consideration of plasma heating of $750\,kW/m^2$, $T^{cc} = 873\,K$ and the pressure in cooling channels of $50\,MPa$

and 600 with the UMAT). Because of the high computing time and huge memory capacity needed, it seems unrealizable to continue such a simulation until the material fails (approximately 6000 to 10000 cycles). Fortunately, the method proposed in [9] by Kiewel, Aktaa & Munz allows the simulation of such number of cycles by extrapolation of simulation data. However, it is a challenge for a further activity.
Figs. 4.1 and 4.2 [1] show distributions of the von Mises stress and the equivalent plastic strain respectively after the heating within the cycle 300 obtained using the ABAQUS standard material model (on the left) as well as

[1] A change of the distributions step by step is shown in appendix A.4 for the cycle 300.

the UMAT under consideration of loadings described above. Both material models yield qualitatively similar stress distributions. However, the ABAQUS standard model leads to a double stress compared to the UMAT, see fig. 4.1. On the other hand, the maximum equivalent plastic strain obtained using UMAT is considerably (approx. factor 10) higher than the corresponding value provided by other material model, see fig. 4.2. This observation can be explained in terms of the stress relaxation due to the consideration of creep within the UMAT. The results have been also generated in a table format along the paths AB and KL depicted in fig. 3.1. An ex-

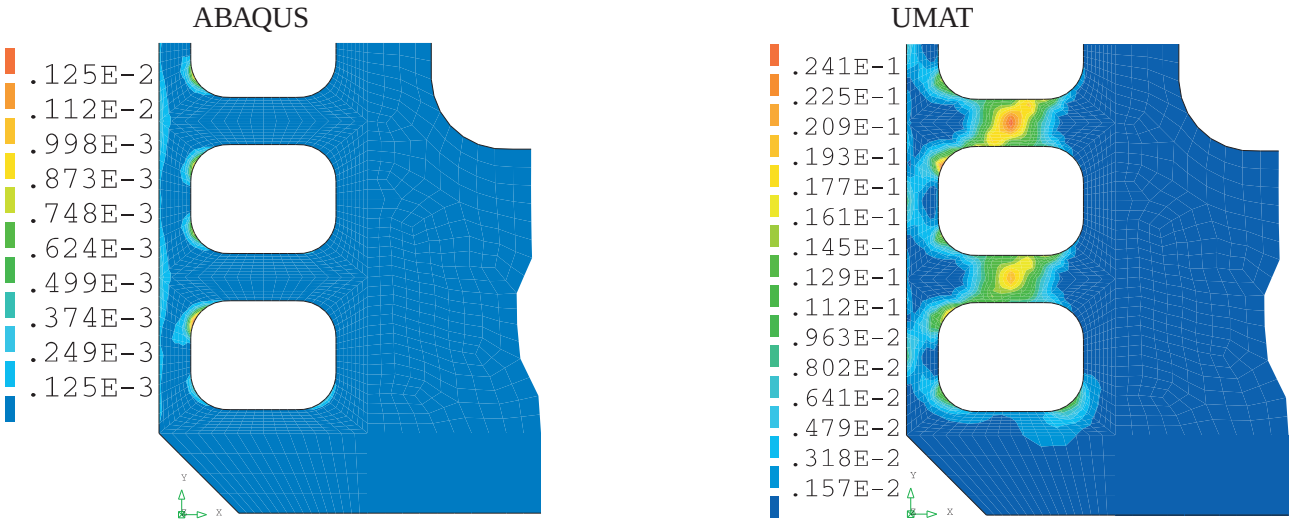

$\overline{\epsilon}_{pl}^{max} = 1.37E-3$ $\overline{\epsilon}_{pl}^{max} = 2.57E-2$

Figure 4.2: A distribution of the equivalent plastic strain after the heating within the cycle 300 obtained using the ABAQUS standard material model (on the left) as well as the UMAT under consideration of plasma heating of $750\,kW/m^2$, $T^{cc} = 873\,K$ and the pressure in cooling channels of $50\,MPa$

amination of the contour plots has shown that the most loaded region in the model is the vicinity of the point L in the path KL. Fig. 4.3 shows a change of the damage variable near this point during first 600 cycles. Thereby, distributions of the damage variable $\mathcal{D}$ are shown additionally for the cycles 100 and 300. A damaged area lies thereby again near the point L.

Additional plots in appendix A.5 depict the change of both the von Mises stress and the equivalent plastic

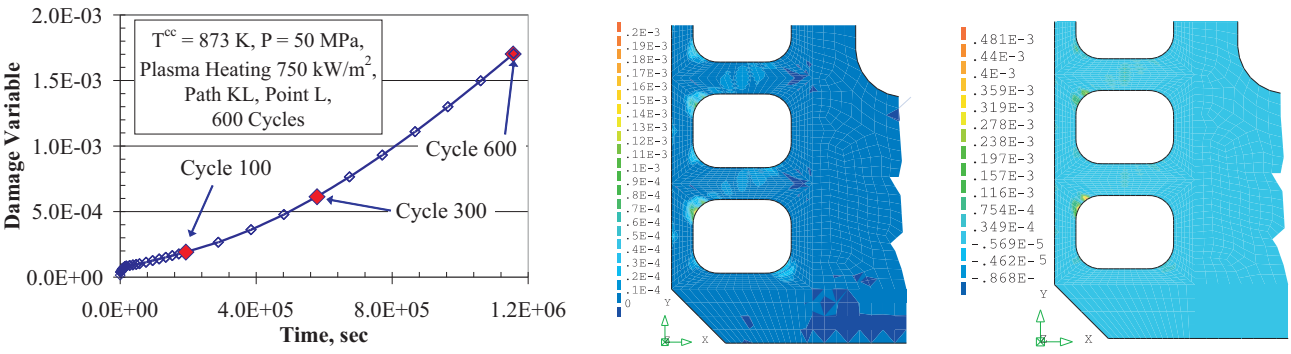

$\mathcal{D}_{UMAT}^{max} =$ $1.82E-4$ $5.22E-4$

Figure 4.3: A change of the damage variable $\mathcal{D}$ near the point L during first 600 cycles together with its distribution in the most loaded region after the cycles 100 and 300 obtained using the UMAT under consideration of plasma heating of $750\,kW/m^2$, $T^{cc} = 873\,K$ and the pressure in cooling channels of $50\,MPa$

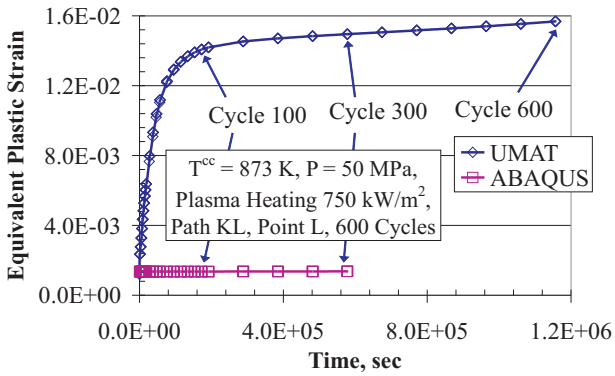

Figure 4.4: The change of the maximum equivalent plastic strain among all values along the path KL, see fig. 3.1, cycle by cycle during the first 300 and 600 cycles computed using the ABAQUS-own material and the UMAT respectively.

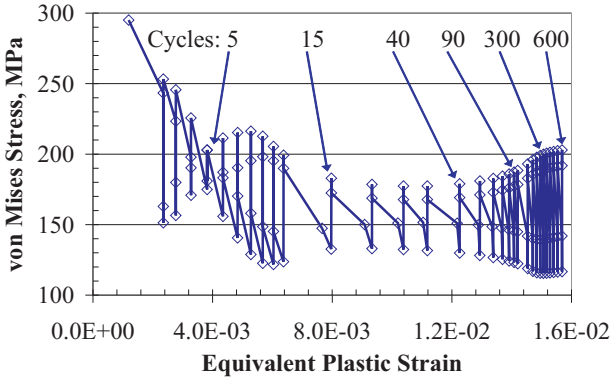

Figure 4.5: Von Mises stress as a function of the accumulated plastic strain computed using the UMAT for the first 600 cycles.

strain along KL for some chosen cycles up to 300 and 600 for the ABAQUS standard model and for the UMAT respectively. The ABAQUS standard model yield only a negligible increase of the accumulated plastic strain as well as a negligible relaxation of the von Mises stress. Contrariwise, an application of the UMAT leads to both an increase of the equivalent plastic strain and a relaxation of the von Mises stress. However, both parameters seem to reach saturated values corresponding to a non-ratcheting behavior.

This convergence can be also observed in the plot representing a change of the maximum equivalent plastic strain near the point L within the first 300 and 600 cycles for the ABAQUS-own material and the UMAT respectively, see fig. 4.4. Furthermore, a presentation of the equivalent stress as a function of the accumulated plastic strain shown in fig. 4.5 corresponds rather to a non-ratcheting behavior. However, to get a definite answer, the extrapolation method mentioned above should be applied.

It is difficult to compare both material models on the basis of the simulation performed due to relatively long hold times at HT, which are significant for creep. For this reason, we have simulated 100 cycles without the hold time at HT and RT i.e. each cycle consists of only two steps: the heating during 30 sec and the cooling during 100 sec. A follow-up examination shows however that even in this case both material models yield quite different results. Indeed, diagrams in fig. 4.6 show that the UMAT yields considerably greater plastic strain even without the hold time. Note that both models lead to quite similar values of the plastic strain after the first heating, see the right-hand side diagram in fig. 4.6. As follows from this diagram, the hold time at HT provides for a significant amount of plastic strain. Nevertheless, the difference between results obtained using the UMAT becomes not as dramatical as between results yielded by different models already after the first 100 cycles.

Fig. 4.7 illustrates the change of the von Mises stress near the point L during 100 cycles. It it easy to recognize that a gap between the results obtained using different material models becomes significant already after the first five cycles.

Figs. 4.8 and 4.9 illustrate an influence of the hold time on simulation results if the UMAT is used. Not later than at this place, it becomes plausible that the ABAQUS own material model is unfortunately inappropriate to describe the component behavior under cyclic loadings partly at HT. Consequently, only the more conservative results obtained based on an application of the UMAT are used below for the verification of some design rules.

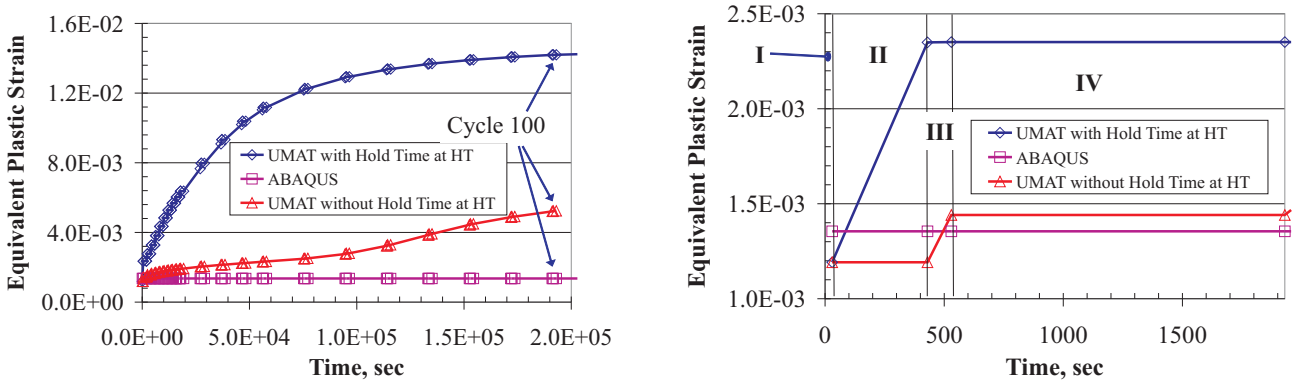

Figure 4.6: On the left: a change of the equivalent plastic strain near the point L during first 100 obtained using the ABAQUS standard model and the UMAT with and without hold times under consideration of plasma heating of $750\,kW/m^2$, $T^{cc} = 873\,K$ and the pressure in cooling channels of $50\,MPa$; on the right: the first cycle.

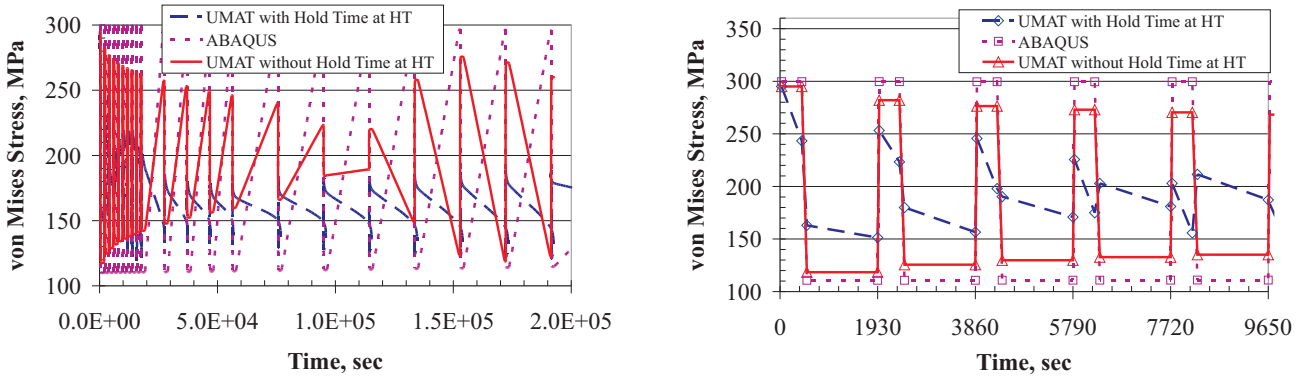

Figure 4.7: On the left: a change of the von Mises stress near the point L during first 100 obtained using the ABAQUS standard model (dotted line) and the UMAT with (dashed line) and without (solid line) hold times under consideration of plasma heating of $750\,kW/m^2$, $T^{cc} = 873\,K$ and the pressure in cooling channels of $50\,MPa$; on the right: first five cycles.

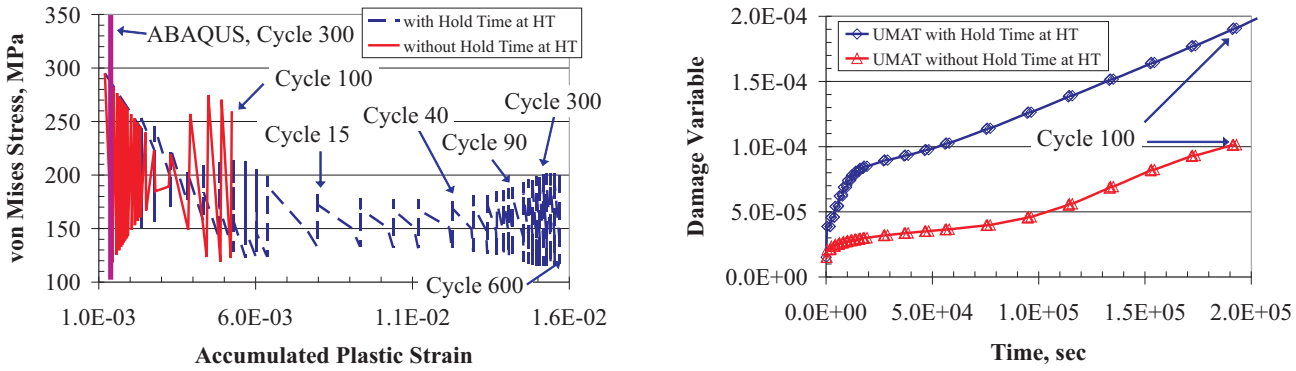

Figure 4.8: Von Mises stress as a function of the accumulated plastic strain computed using the UMAT for the first 100 cycles with (dashed line) and without (solid line) the hold time at HT; the data obtained using of the ABAQUS standard model are shown for comparison.

Figure 4.9: Evolution of the damage variable $\mathcal{D}$ during the first 100 cycles with (dashed line) and without (solid line) the hold time at HT computed using the UMAT.

Chapter 5

Verification of Design Rules

The aim is now to compare the results discussed above with a prediction of some design rules based on linear-elastic simulations. To apply the design rules, different material limits should be evaluated. There are the allowable primary membrane stress intensity S_m, the allowable primary plus secondary membrane stress intensity S_e, the allowable total stress intensity S_d for low temperature rules as well as the primary stress creep usage fraction U_t for high temperature rules.

5.1 Calculation of Material Limits

Firstly, we calculate the material limits mentioned above under consideration of the experimental data obtained in the uniaxial cyclic tensile tests represented in section 2.

5.1.1 The allowable primary membrane stress intensity

According to ITER SDC-IC [1], subsection IC 2723, S_m is the lowest stress intensity at a given temperature [1] among the time-independent strength quantities:

$$S_m \doteq \min\left\{\frac{1}{3}S_u\,,\,\frac{2}{3}S_y\right\} \tag{5.1}$$

with the minimum [2] ultimate tensile strength S_u as well as the minimum yield strength S_y.
Available S_m values do not consider a change of the tensile strength and yield stress under a cyclic loading. This change can however be taken into account if S_m is calculated on the basis of the experimental data reported by J. Aktaa and R. Schmitt in [7]. Note that the available maximum achieved tensile stress has been used here for calculations instead of the ultimate tensile strength. To obtain the needed tensile strengths, isothermal tensile tests should be performed after e.g. 10, 20 etc. cycles.
The new value,calculated in such manner, is represented in fig. 5.1 together with the available S_m values from ITER SDC-IC [1], appendix A. It was thereby assumed that each cycle is $1930\ sec = 0.54\ h$ long. To avoid a misunderstanding, the value has been labeled as S_m^*.
As follows from the diagrams in fig. 5.1, ITER SDC-IC [1], appendix A provides too high values of S_m. Unfortunately, it is not straightforward to compare directly cycles in tensile experiments carried out at a constant temperature on small specimens with operating cycles of a component including mechanical pressure in cooling channels and possibly high temperature gradients. For this reason, we have calculated only one S_m^* value for each temperature and labeled it as S_m^C, whereby the subscript C denotes that the value should be applied if C-type loadings appear in contrast to S_m values valid for M-type loadings. This value corresponds to a cycle number $N_f/2$ highlighted in fig. 5.1 and is representative for the given temperature. S_m^* becomes therewith a transient value and is not applied below. As follows from diagrams depicted on the left in fig. 5.2, the value

[1] A dependence on the neutron fluence in not considered here.
[2] The minimum value between the values at the room and at the given temperature.

exhibits a very similar behavior as a function of temperature with the reference S_m values. A gap between the curves increases with increasing temperature as shown again in fig. 5.2, on the right. Thereby, the gap increases almost linearly at HT beginning with $450°C\,(723\,K)$. The reduction of the allowable stress intensity due to cyclic softening should definitively be considered in design estimations if C-type loadings are considered.

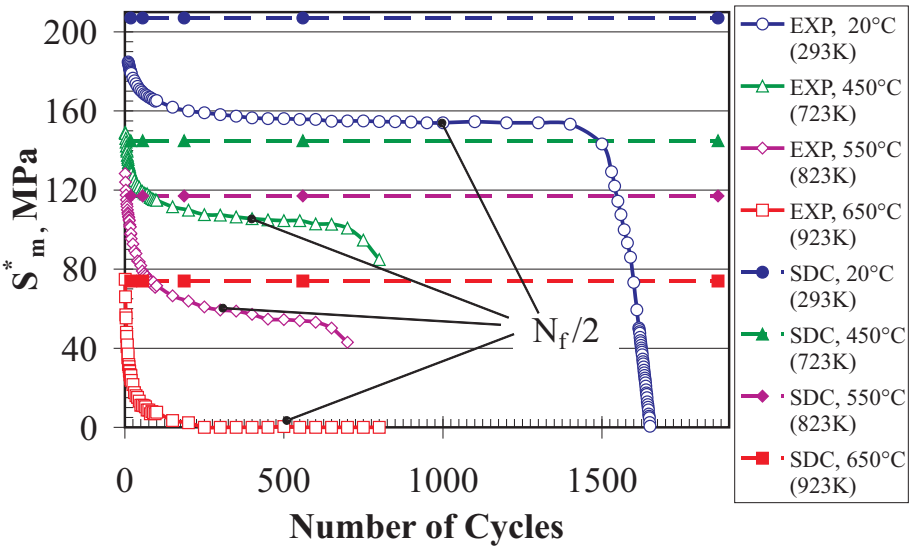

Figure 5.1: Change of S_m^* under cyclic loading at RT, $450°C$ $(723\,K)$, $550°C$ $(823\,K)$ and $650°C$ $(923\,K)$; available data for these temperatures are also given for comparison.

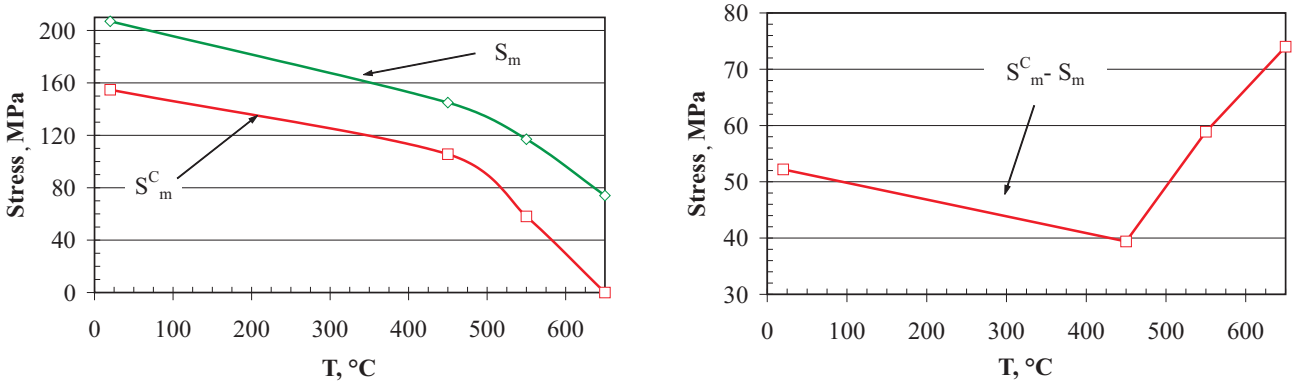

Figure 5.2: On the left: the change of S_m^C with temperature up to $650°C$ $(923\,K)$; available data for these temperatures S_m are also given for comparison; on the right: the difference between S_m^C and S_m.

5.1.2 The allowable primary plus secondary membrane stress intensity

The allowable primary plus secondary membrane stress intensity S_e is defined as, see ITER SDC-IC [1], subsection IC 2724,

$$S_e \doteq \begin{cases} \frac{1}{3}S_u(T_m) + \frac{1}{3}\frac{E(T_m)}{2\,r_1}\left[\epsilon_u(T_m) - 0.02\right] & \text{if } \epsilon_u(T_m) \geq 2\% \\ \frac{1}{3}S_u(T_m) & \text{if } \epsilon_u(T_m) < 2\% \end{cases} \tag{5.2}$$

with the minimum ultimate tensile strength S_u, the Young's modulus E, the minimum uniform elongation [3] ϵ_u and the elastic follow-up factor $r_1 = 4$ (the conservative value). All the parameters should be evaluated at the

[3]The plastic component of the engineering strain at the time when the necking begins; the values are reported in ITER SDC-IC [1], appendix A for the EUROFER 97.

thickness averaged temperature T_m. It turned out that $\epsilon_u(T_m) < 2\%$ if $T_m \geq 425° \, (698K)$. The change of the elastic modulus with temperature obtained from the cyclic experiments reported above is depicted in fig. 5.3. The allowable stress intensity calculated according to (5.2) under consideration of the S_u values from the cyclic experiment and labeled as S_e^C similar to S_m^C is shown in fig. 5.4 as a function of temperature together with the values based on S_u available in ITER SDC-IC [1], appendix A. Note that the S_e limit must not be evaluated for ductile materials. Nevertheless, here we check also the fulfillment of this criterion.

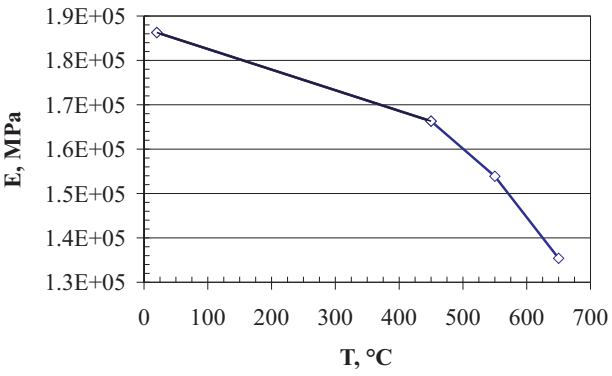

Figure 5.3: Change of the elastic modulus E with the increasing temperature.

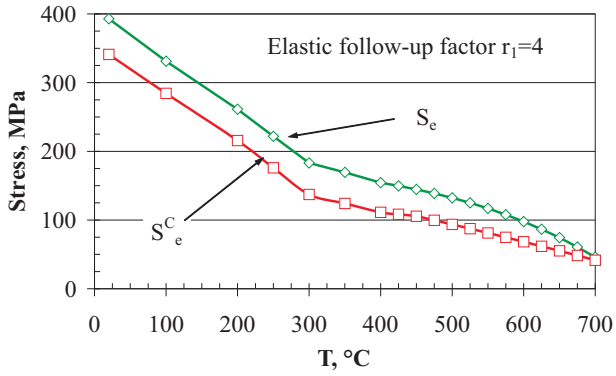

Figure 5.4: Change of S_e^C with temperature up to $700°C \ \ (973\,K)$; data computed on the basis of available values for the ultimate tensile strength S_u and the minimum uniform elongation ϵ_u for these temperatures are also given for comparison.

5.1.3 The allowable total stress intensity

According to ITER SDC-IC [1], subsection IC 2725, the allowable total stress intensity is given by the following expression:

$$S_d \doteq \frac{2}{3}\left[S_u(T_m) + \frac{E(T_m)}{r}\,\frac{\epsilon_{tr}(T_m)}{TF}\right] \tag{5.3}$$

with E, S_u and T_m are defined in the previous section and the minimum true strain at rupture ϵ_{tr} is given for EUROFER 97 in ITER SDC-IC [1], appendix A. The triaxiality factor TF is defined as the ratio of the hydrostatic stress to the von Mises norm and normalized to unity for an uniaxial tension. In the calculation of S_d, we have used $TF = 2.01$, which is the maximum positive TF value within the first 600 cycles simulated using the UMAT, see fig. 5.5. The elastic follow-up factor takes different values in dependency on whether the peak stress F is included to the total stress intensity:

- the peak stress F is included $\overline{P_m + P_b + Q + F}$

$$r_2 \doteq \max\{K_T\,, 4\} \tag{5.4}$$

- the peak stress F is excluded $\overline{P_m + P_b + Q}$

$$r_3 \doteq \begin{cases} \infty & \text{if } \epsilon_u(T_m) \leq 2\% \\ 4 & \text{if } \epsilon_u(T_m) > 2\% \end{cases} \tag{5.5}$$

whereby K_T is the elastic stress concentration factor. Here, we have assumed $r_2 = 4$ for all calculations. The change of S_d calculated using S_u values from both the cyclic tests and ITER SDC-IC [1], appendix A as a function of temperature is depicted in fig. 5.6. The value calculated on the basis of the cyclic tensile tests is labeled again as S_d^C. It turned out that values corresponding to $r_3 \neq \infty$ are very sensitive with respect to ϵ_{tr}

and TF. In the case if the peak stress is not considered in the total stress intensity and ϵ_u is less than 2% i.e. $T_m \geq\approx 425°C\,(698\,K)$, $r_3 = \infty$ and (5.3) takes an especially simple format depending neither on ϵ_{tr} nor on TF:

$$S_d \doteq \frac{2}{3} S_u(T_m) \tag{5.6}$$

Similar to the S_e limit, the S_d limit also must not be evaluated for ductile materials. Nevertheless, here we check also the fulfillment of this criterion for the particular case described above.

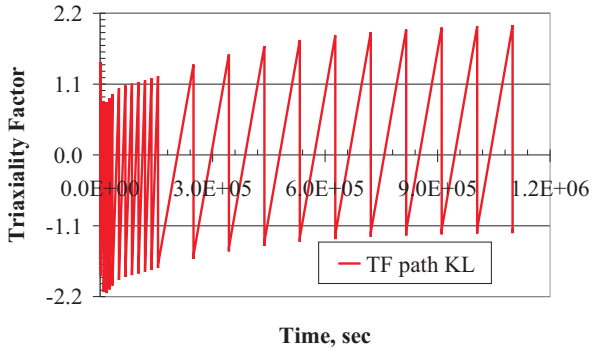

Figure 5.5: Change of the triaxiality factor TF along the path KL within the first 600 cycles computed using the UMAT.

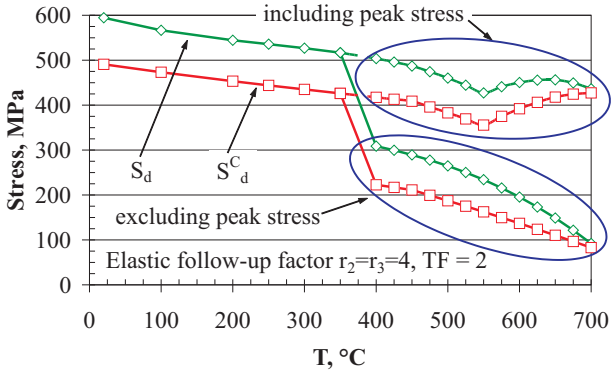

Figure 5.6: Change of S_d^C with temperature up to $700°C$ $(973\,K)$; data computed on the basis of available values for the ultimate tensile strength S_u and the minimum true strain at rupture ϵ_{tr} for these temperatures are also given for comparison.

5.2 Stress Categorization

To separate primary and secondary stresses, linear-elastic simulations have been performed for three load cases: thermal and mechanical loads acting together and separated. A comparison of the results obtained allows the recognition that the influence of plasma heating is partially compensated by the coolant pressure. Results of these simulations have been linearized automatically along the paths discussed above using the corresponding option of the ABAQUS VIEWER.

5.3 Design Rules chosen for Evaluation

Within the frame of the work presented, the following low-temperature design rules have been evaluated:

- rules for prevention of immediate plastic collapse and plastic instability (M-type damage)

$$\overline{P_m} \leq S_m \tag{5.7}$$

$$\overline{P_m + P_b} \leq K_{eff}\, S_m \tag{5.8}$$

- the rule for prevention of immediate plastic flow localization (M-type damage)

$$\overline{P_m + Q_m} \leq S_e \quad \text{(elastic analysis)} \tag{5.9}$$

$$\epsilon_{m1}^{pl} \leq \frac{\epsilon_u\,(T_m)}{2} \quad \text{(elastic-plastic analysis)} \tag{5.10}$$

- the rule for prevention of immediate local fracture due to exhaustion of ductility (M-type damage)

$$\overline{P_m + P_b + Q} \;\leq\; S_d \tag{5.11}$$

- the rule for prevention of progressive deformation or ratcheting (C-type damage)

$$\overline{P_m + P_b} + \left[\overline{\Delta P}_{max} + \overline{\Delta Q}_{max}\right] \;\leq\; 3\, S_m \quad \text{(elastic analysis)} \tag{5.12}$$

$$\epsilon^{pl}_{m1} \;\leq\; 0.5\, \lambda_1 \min_{T_m} \{\epsilon_u\,(T_m)\} \quad \text{(elastic-plastic analysis)} \tag{5.13}$$

Note that all overlined expressions above mean the von Mises norm defined as

$$\overline{\sigma} \doteq \sqrt{1/2}\, \left[\left[\sigma_{11} - \sigma_{22}\right]^2 + \left[\sigma_{22} - \sigma_{33}\right]^2 + \left[\sigma_{33} - \sigma_{11}\right]^2 + 6\, \left[\sigma^2_{12} + \sigma^2_{23} + \sigma^2_{31}\right]\right]^{1/2}$$

Furthermore, K_{eff} is the effective bending shape factor, which ranges in general between 1.0 and 2.0. In the case of an irradiated material, $K_{eff} = K = 1.5$, where K is the usual bending shape factor used in the RCC-MR and in the ASME code. ϵ^{pl}_{m1} denotes the significant mean plastic strain defined in ITER SDC-IC [1], subsection IC 2616 as the greatest positive principal strain of the membrane strain tensor ϵ_m. Furthermore, $\lambda_1 = 0.3$ is the safety factor for the level A. Besides these three factors, the following conventional notations are used here: $\overline{P_m}$, $\overline{P_m + P_b}$ and $\overline{P_m + Q_m}$ denote the primary membrane stress intensity, the primary membrane plus bending stress intensity as well as the primary plus secondary membrane stress intensity excluding plasma disruption loadings, respectively; $\overline{P_m + P_b + Q}$ is the total stress intensity excluding the peak stress F. $\overline{\Delta Q}_{max}$ and $\overline{\Delta P}_{max}$ are the maximum in the thickness secondary (thermal) stress intensity range and the stress intensity range due to disruption loadings (here not considered). Possibly, $\overline{\Delta P}_{max}$ should also include the stress intensity range due to the change of the pressure in cooling channels. Furthermore, the low-temperature Bree-diagram rule has been also evaluated:

$$Y \;\leq\; \begin{cases} 1/X & \text{if } 0.0 \leq X \leq 0.5 \\ 4[1 - X] & \text{if } 0.5 \leq X \leq 1.0 \end{cases} \tag{5.14}$$

Thereby,

$$\begin{array}{rcl} X & \doteq & \overline{P_m}/S_y \\ Y & \doteq & \left[\overline{\Delta P}_{max} + \overline{\Delta Q}_{max}\right]/S_y \end{array} \tag{5.15}$$

Here, S_y is the average of the minimum yield strength evaluated at the minimum and maximum thickness-averaged temperatures and fluences during the cycle calculated along the supporting line segments.
We have also evaluated two high-temperature rules based again on the linear-elastic analysis:

- Creep effects

$$U_t\left(\overline{P_m}\right) \;\leq\; 1 \tag{5.16}$$

$$U_t\left(\overline{P_m + P_b/K_t}\right) \;\leq\; 1 \tag{5.17}$$

with the creep usage fraction for primary stress U_t, see ITER SDC-IC [1], subsection IC 2764 and the creep bending shape factor $K_t \doteq \left[K_{eff} + 1\right]/2$.

5.4 Evaluation of the Low-Temperature Design Rules

The maximum values required for evaluation of (5.7)-(5.12) except for (5.10) are collected in table 5.1. An easy comparison shows that none of the five criteria is fulfilled even for values stemming from ITER SDC-IC [1], appendix A at $T^{cc} = 600°C\ (873\,K)$. If a stress intensity limit value at the average temperature along the path (approx. $625°C$ or $899\,K$) is considered, the difference becomes more essential. The stress intensity limit values for this temperature calculated on the basis of the cyclic experiments are out of any competition. However, we should note that the average temperature appearing in the simulation presented cannot be considered

as a usual operating temperature lying at approximately $500°\,C\,(773\,K)$-$550°\,C\,(823\,K)$. In addition to the tables, fig. 5.7 illustrates the change of S_m^C, $K\,S_m^C$ and $3\,S_m^C$ from RT up to $650°C$ or $923\,K$ when S_m^C becomes zero. We have also represented all stress limits together for the aim of comparison, see fig. 5.8.
An application of (5.14) shows that the less conservative Bree-diagram rule is fulfilled for three different temperatures from $873\,K$ to $923\,K$, see table 5.2. Nevertheless, criterion (5.12) should also be satisfied before an application of the high-temperature $3\,S_m$ rule, see ITER SDC-IC [1], subsection IC3541.3.

An evaluation of both (5.10) and (5.13) rules requires a calculation of the significant mean plastic strain

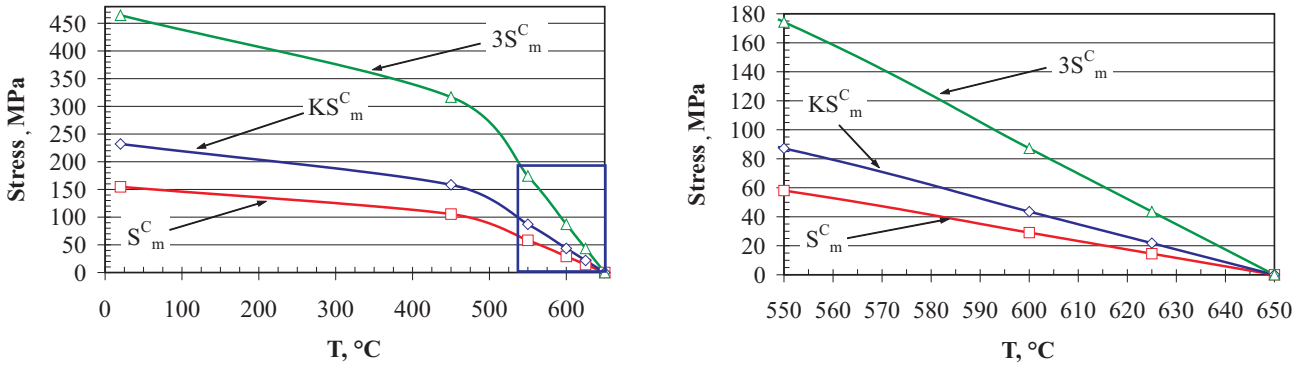

Figure 5.7: Change of S_m^C, $K\,S_m^C$ and $3\,S_m^C$ with temperature. The region $550°\,C$ to $650°\,C$ is shown more detailed in the right-hand side diagram.

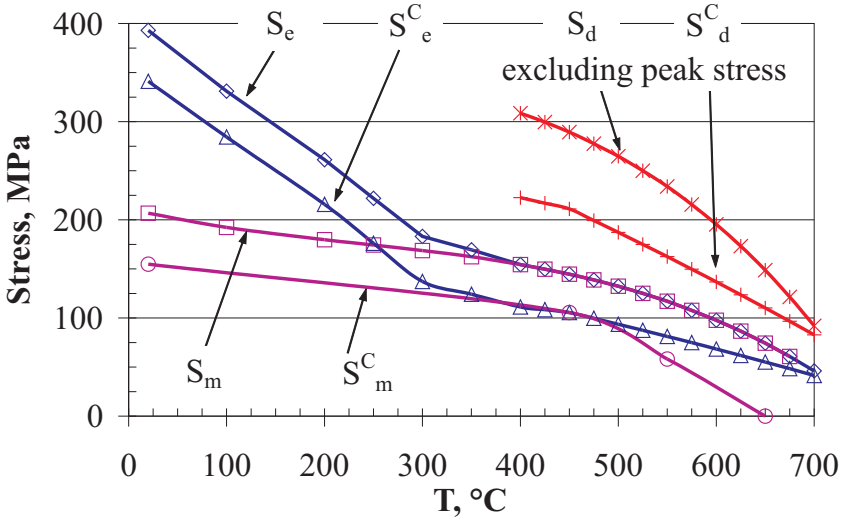

Figure 5.8: Comparison of the material stress limits as functions of temperature

ϵ_{m1}^{pl}. Fig. 5.9 illustrates the change of ϵ_{m1}^{pl} along the path KL within the first 600 cycles simulated using the UMAT. The maximum value corresponds to the last simulated cycle and lies at 0.37%. The rule (5.10) requires however a maximum significant mean plastic strain obtained under a monotonic loading multiplied by a safety factor given in ITER SDC-IC [1]. Unfortunately, this value is not available so that we use the more conservative value reported above. This value should be compared with the half of the uniform elongation ϵ_u at the thickness-averaged temperature T_m i.e. at approximately $625°\,C\,(898\,K)$ in our case. Available values of ϵ_u are represented in fig. 5.10 in dependence on the temperature, whereby averaged values are given by the upper curve whereas the lower curve connects the minimum values. A half of the minimum value corresponding to T_m is approximately 0.40%. It means that (5.10) is fulfilled even with the conservative value of ϵ_{m1}^{pl}.
The rule (5.13) requires a minimum value of ϵ_u for all times during the total operating period. As follows from fig. 5.10, $\min_{T_m}\{\epsilon_u\,(T_m)\} = 0.5$ at $T_m = 600°\,C\,(873\,K)$. Therewith, (5.13) is not fulfilled since $0.5 \cdot 0.3 \cdot 0.5 = 0.075 < 0.370$.

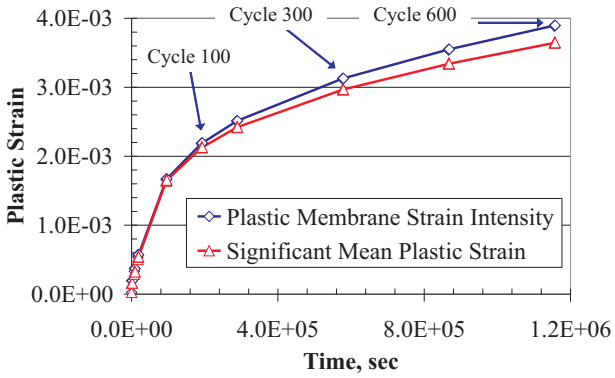

Figure 5.9: Change of the significant mean plastic strain ϵ^{pl}_{m1} along the path KL within the first 600 cycles simulated using the UMAT.

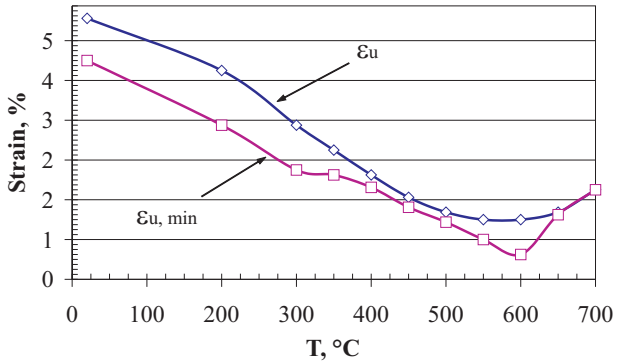

Figure 5.10: Available values of the uniform elongation ϵ_u as a function of temperature up to $700°C\ (973\,K)$; the upper curve is a result of an averaging among all experimental data, the lower curve connects the minimum values (source: ITER SDC-IC [1], appendix A).

5.5 Evaluation of the High-Temperature Design Rules

In general, the HT design rules should be evaluated first if the low-temperature criteria are fulfilled. It is not the case but nevertheless we evaluate the rules (5.16) and (5.17) to show how U_t can be estimated.
A time-dependent allowable stress intensity for primary stresses S_t is needed to calculate U_t and defined in ITER SDC-IC [1], subsection IC 2726 as a temperature and time-dependent stress intensity limit

$$S_t \doteq \min\left\{\frac{2}{3}\sigma_{crp}\,,80\%\sigma_{tertiary}\,,\sigma_{1\%}\right\}. \tag{5.18}$$

Here, σ_{crp} is the minimum stress corresponding to average creep rupture time t at the temperature T, $\sigma_{tertiary}$ is the minimum stress causing the tertiary creep to time t at the temperature T and, finally, $\sigma_{1\%}$ is the minimum stress to cause the creep strain of $\min\{1\%\,,\epsilon_C/5\}$ with the total elongation at rupture ϵ_C determined from uniaxial isothermal tensile creep tests.
The creep usage fraction for the primary stress U_t generalizes the S_t for the case if the stress or the temperature depends on time. To compute U_t, the operating time should be subdivided into N time intervals [4] , whereby only those time intervals should be considered, for which the temperature is higher than a defined temperature corresponding to the beginning of non-negligible creep processes. Such temperature lies at $425°\,C\,(698\,K)$ for the EUROFER 97, see ITER SDC-IC [1], appendix A. For each interval j of the duration t_j should be found the highest temperature T_j and the highest total stress intensity $\overline{\sigma_j}$. For these stress and temperature, the maximum allowable time $t_{s,\,j}$ should be obtained from the S_t curves, see fig. 5.11, the left-hand side diagram. U_t is then defined as the following sum:

$$U_t \doteq \sum_{j=1}^{N}\frac{t_j}{t_{s,\,j}}\,. \tag{5.19}$$

In the case of the linear-elastic simulation, all cycles are evidently identical so that we can consider only one cycle consisting of four steps described in section 4. The highest temperature reaches thereby $715°\,C\,(988\,K)$; we use here however the thickness-average temperature of approximately $625°\,C\,(898\,K)$. The duration t_1 of the interval above $425°\,C\,(698\,K)$ is equal approximately to $454.2\,sec.$ The required in (5.16) and (5.17) maximum stress intensities take the following values within the interval: $\overline{P_m} = 117\,MPa$; $\overline{P_m + P_b/K_t} = 163.6\,MPa$. Simple analysis of the S_t curves in the right-hand side diagrams in fig. 5.11 shows that the

[4] For the aim of plausibility, we use here $N = 1$. Generally, this assumption is however incorrect.

Table 5.1: Maximum absolute values of the categorized stress components and their combinations among all values for the chosen paths together with the corresp. values of the available S_m and calculated S_m^C stress intensity limits; the units are MPa.

$\overline{P_m}$	$S_m^{898\,K}$	$S_m^{C\,898\,K}$	$S_m^{873\,K}$	$S_m^{C\,873\,K}$
117.0	87.0	14.5	98.0	29.1
$\overline{P_m + P_b}$	$K\,S_m^{898\,K}$	$K\,S_m^{C\,898\,K}$	$K\,S_{mt}^{873\,K}$	$K\,S_m^{C\,873\,K}$
179.7	130.5	21.8	147.0	43.6
$\overline{P_m + Q_m}$	$S_e^{898\,K}$	$S_e^{C\,898\,K}$	$S_e^{873\,K}$	$S_e^{C\,873\,K}$
129.9	86.6	61.8	97.7	68.4
$\overline{P_m + P_b + Q}$	$S_d^{898\,K}$	$S_d^{C\,898\,K}$	$S_d^{873\,K}$	$S_d^{C\,873\,K}$
260.9	173.1	123.6	195.3	136.8
$\overline{P_m + P_b} + \overline{\Delta Q_{max}}$	$3\,S_m^{898\,K}$	$3\,S_m^{C\,898\,K}$	$3\,S_m^{873\,K}$	$3\,S_m^{C\,873\,K}$
179.7+215.8=395.5	261.0	43.6	294.0	87.2

Table 5.2: Application of the Bree-diagram rule.

$T\,,K$	$S_y\,,MPa$	X	$1/X$	$4[1-X]$	Y
873	282	0.41	2.41	-	0.77
898	250	0.47	2.14	-	0.86
923	214	0.55	-	1.81	1.01

maximum allowable time at the average temperature under the load of $117\,MPa$ is approximately 3 hour. The criterion (5.16) is then fulfilled if N does not exceed 22 cycles. The second criterion (5.17) cannot be fulfilled for the average temperature. It becomes true first for $575°\,C\,(848\,K)$ if $N \leq 16$. If we however consider that the life time of the component should be approximately $1E+4$ cycles, it becomes evident that the high-temperature criterion is not fulfilled. The result colud be probably enhanced if we would subdivide the whole time interval into several shorter intervals. It would be reasonable first if the low-temperature criteria would be fulfilled.

Thus, the chosen design rules predict (a) the plastic collapse and plastic instability , (b) the probable plastic flow

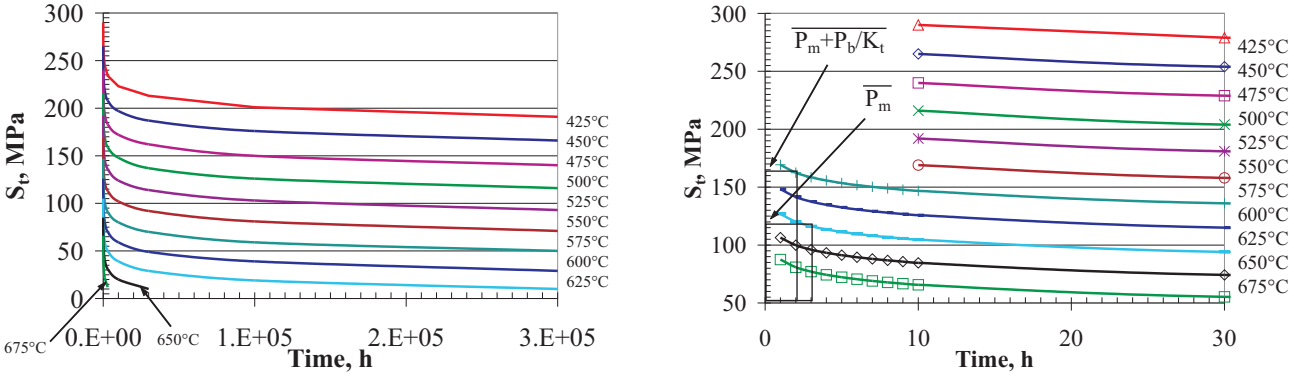

Figure 5.11: S_t curves needed to calculate the creep usage fraction for primary stress $U_t(\overline{P_m})$ and $U_t(\overline{P_m + P_b/K_t})$.

localization, (c) the local fracture due to the exhaustion of ductility as well as (d) the probable accumulation of plastic deformation. The prognoses confront however with simulation results using of the viscoplastic material model that includes damage, which show rather a non-ratcheting behavior at least for the first 600 cycles. However, as mentioned above, to obtain a more definite result, the extrapolation method proposed by Kiewel, Aktaa and Munz [9] should be applied and, on the other hand, all design criteria should be checked according to the scheme given in ITER SDC-IC [1], subsection IC 3030.

Chapter 6

Considerations concerning the Mock-Up Experiment

In this section, we propose a relatively simple mock-up model of the TBM and perform an investigation, how a variation of some geometrical and loading parameters influences an accumulation of inelastic deformation as well as an evolution of the damage in the model. Thereby, we use the coupled deformation-damage material model described in section 2.2.

6.1 Model Assumptions

According to our proposition, the box-shaped model has three cooling channels as depicted in fig. 6.1. The coolant pressure P is firstly assumed to be constant and equal to $100\,bar = 10\,MPa$. The coolant temperature should vary from channel to channel in accordance with the reality in the TBM. In the study, we consider the following four cases:

1. $T_1 = 300°C\ (573\,K)$ & $T_2 = 350°C\ (623\,K)$
2. $T_1 = 350°C\ (623\,K)$ & $T_2 = 300°C\ (573\,K)$
3. $T_1 = T_2 = 300°C\ (573\,K)$
4. $T_1 = T_2 = 350°C\ (623\,K)$

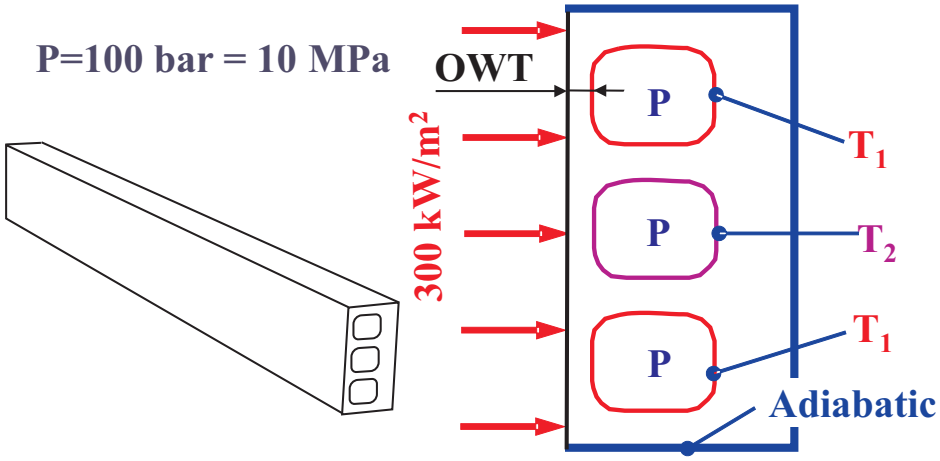

Figure 6.1: The geometry of the proposed mock-up model together with the mechanical and thermal loads (on the right).

The cycles are chosen similar to the working cycles of the TBM:(1) heating and application of the pressure, $30\,sec$; (2) holding at the high temperature (HT) t^{HT}_{hold}, (3) cooling to RT, $100\,sec$ and, finally, (4) holding at RT

for $600\,sec$. Thereby, t_{hold}^{HT} is evidently relevant for the amount of inelastic deformation and has for this reason been chosen as the 1^{st} design parameter. The outer wall thickness (OWT) has been chosen as the 2^{nd} design parameter and changes in the range of $1\,mm$ to $5\,mm$.
Thus, within the frame of the work presented we have simulated first 50 cycles for $OWT = 1.0\,mm\,;\ 2.0\,mm$; $3.5\,mm\,;\ 5.0\,mm$ and $t_{hold}^{HT} = 600\,sec\,;\ 1800\,sec$; $3600\,sec\,;\ 7200\,sec$ on the basis of a 2D model. The temperature distribution as well as the linear-elastic behavior have been simulated however on the basis of a 3D model.

6.2 The Finite Element Discretization

The finite element model includes only a half of the total component. Fig. 6.2 depicts a FE discretization if $OWT = 3.5\,mm$ corresponding to the current design of the TBM. We have used 8-node linear brick elements C3D8 and 8-node biquadratic quadrilateral generalized plain strain elements CPEG8 for the 3D and 2D FE models, respectively. The corresponding diffusive heat transfer elements DC3D8 and DC2D8 have been used for thermal simulations.

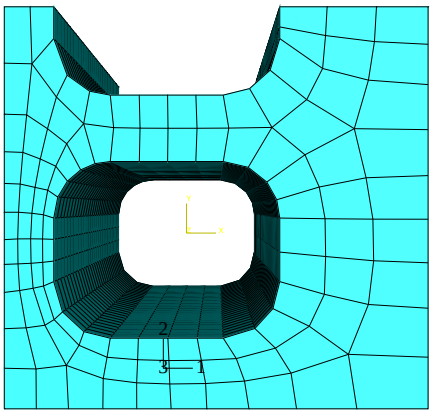

Figure 6.2: The discretized 3D finite element model for $OWT = 3.5\,mm$.

6.3 Thermal Simulations (3D)

For the aim of simplicity, we suppose that the temperature is constant at the surface of each cooling channel also for a 3D model. As shown in fig. 6.1, the front side of the model undergoes a heat irradiation of $300kW/m^2$ remaining constant for all simulations performed. For other outer surfaces, the adiabatic boundary condition is considered, see fig. 6.2. Typical temperature distributions in the model with the $OWT = 3.5\,mm$ computed for the cases 1 to 4 are shown in fig. 6.3 [1].
The maximum temperature in the model is depicted on the left-hand side diagram in fig. 6.4 as a function of the OWT for all four cases. It turned however out that the cases 3 and 4 are uninteresting since they care only for a small difference between the minimum and maximum temperatures in the model, see the right-hand side diagram in fig. 6.4. Evidently, the temperature gradient becomes highest in the case 2. Thus, only the cases 1 and 2 are used for the modeling represented below.

6.4 Linear-Elastic Simulations (3D)

Using the temperature distributions described in the previous section, we have firstly computed a material response on the basis of a linear-elastic material model. The influence of the coolant pressure and the plasma heating on the stress and strain distributions has been thereby studied for the cases if both these loadings act

[1] For temperature distributions in models with different OWT we refer to appendix B.1

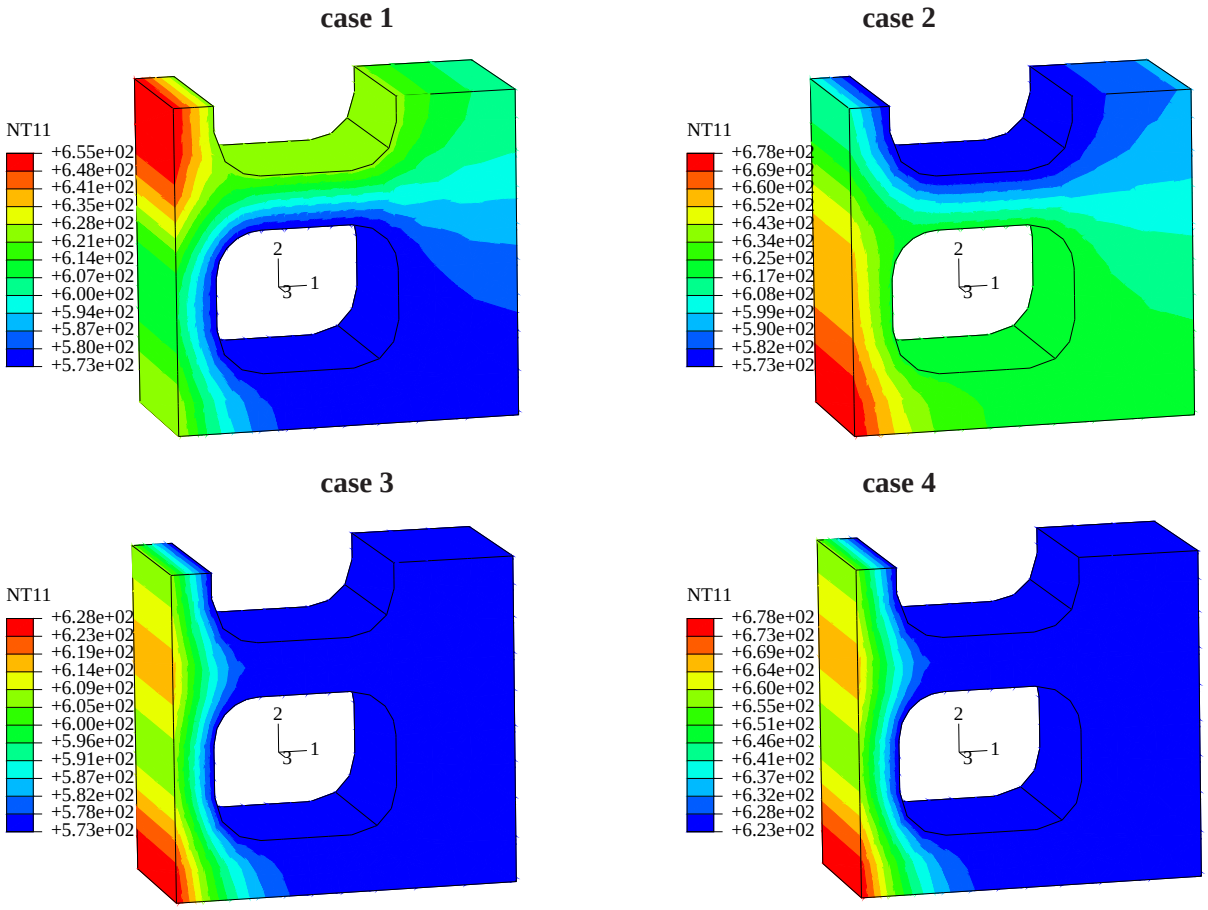

Figure 6.3: An example of the temperature distribution (in K) in the model with the $OWT = 3.5\,mm$ calculated for the cases 1 (on the left) and 2.

simultaneously and separate. The corresponding contour plots are placed in appendix B.1.
Diagrams represented in fig. 6.5 allow the understanding, how the loadings influence the maximum von Mises stress and the total strain depending on the OWT. The $OWT = 1.0\,mm$ provides for the highest von Mises stress placed in the thin outer wall. For the same reason i.e. due to the thick outer wall, the von Mises stress is influenced by the coolant pressure fewest if $OWT = 5.0\,mm$. For all load cases, the temperature gradient provides for the main amount of the total strain.

6.5 The Behavior under Cyclic Loading (2D)

6.5.1 Dependence on the Hold Time at HT

As mentioned above, we have simulated 50 working cycles with the different hold time at the high temperature t_{hold}^{HT} for the 2D models with the different OWT using the UMAT. Distributions of the von Mises stress, the magnitude of the accumulated inelastic strain and the damage variable after the holding at HT if $t_{hold}^{HT} = 7200\,sec$ are collected in appendix B.2. The plots are thereby qualitatively representative for all t_{hold}^{HT} checked.
The plots allow the finding some critical points depicted explicitly in fig. 6.6 together with mechanical boundary conditions. Indeed, the pairs of points 1-1 & 4-1 as well as 2-1 & 2-2 are critical if $OWT = 1.0\,mm$ and $OWT = 2.0\,mm$ for the case 1 and 2, respectively. For $OWT = 3.5\,mm$ and $OWT = 5.0\,mm$, the pairs 2-1 & 3-1 and 2-2 & 5-1 are critical in the case 1 and 2, respectively. However, the highest damage occures in the points 2-1 & 2-2 if $OWT = 3.5\,mm$ and in the points 3-1 & 5-1 if $OWT = 5.0\,mm$. Important is thereby the fact that the stress/strain/damage distributions are qualitatively similar for these two OWTs.

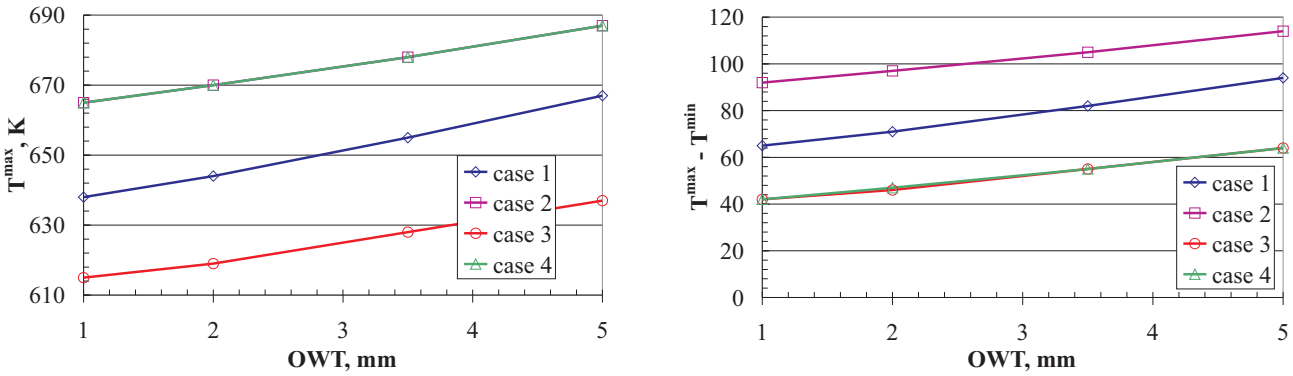

Figure 6.4: The maximum temperature (on the left) and the temperature difference in the model depending on the OWT for different surface temperatures in the cooling channels (cases 1 to 4).

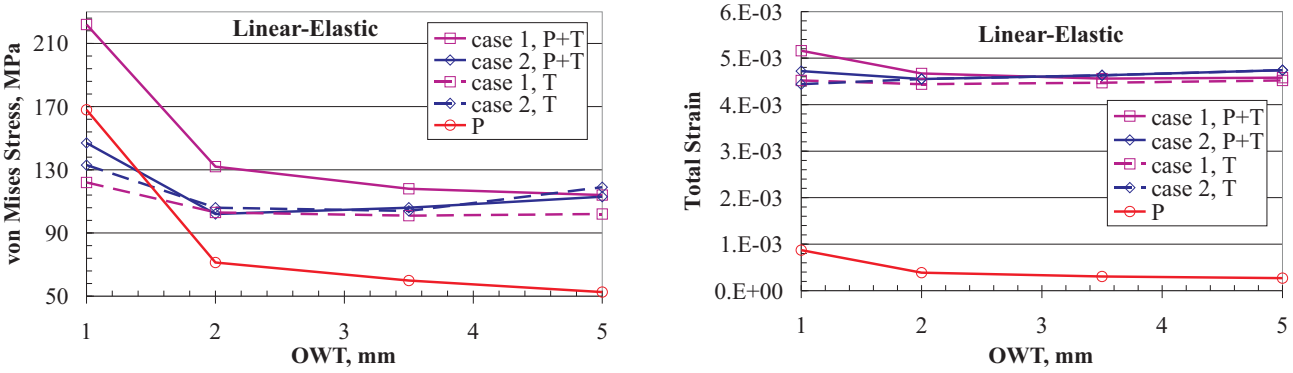

Figure 6.5: Maximum von Mises stress (on the left) and maximum total strain in the model caused by both the coolant pressure and the plasma heating acting together and separate computed as a function of the OWT for the cases 1 and 2.

An amount of inelastic strain is represented in fig. B.7 for the cases 1 and 2. It is easy to see that the inelastic strain exhibits only a slight dependence on the hold time whereas the OWT plays a main role in this process. Thereby, the maximum inelastic strain occurs if $OWT = 1.0\,mm$. Note also that the case 2 leads to a significant amount of inelastic strain if $OWT = 5.0\,mm$.

The diagrams drown to a larger scale in fig. 6.8 allow the recognition that $OWT = 3.5\,mm$ provides for a minimum amount of inelastic strain. This fact is important for TBM designers. Within the frame of the work presented, we are however aimed to reach a failure of the mock-up model within as short as possible time. Thereby, the mock-up model and the TBM should have similar critical areas. According to actual propositions, the TBM has the outer wall thickness of exactly $3.5\,mm$. It means that $OWT = 5.0\,mm$ combined with the case 2 is more appropriate for the mock-up model than $OWT = 1.0\,mm$ in combination with the case 1 in spite of the higher grade of damage in the last case.

The next step is to choose the optimum hold time at HT. Thereby, we compare only two cases providing for a highest damage: $OWT = 1.0\,mm$ and $OWT = 5.0\,mm$. Diagrams in fig. 6.9 represent an evolution of the accumulated inelastic strain in the actual critical point during the first 50 cycles with the different hold time at HT only for two important combinations: $OWT = 1.0\,mm$ & case 1 (on the left) and $OWT = 5.0\,mm$ & case 2 [2]. Evidently, the combination $OWT = 5.0\,mm$ & case 2 provides for an amount of inelastic strain and

[2]Similar plots containing additionally evolutions of the von Mises stress and damage for all combinations are collected in appendix B.3. The plots show definitely that the combination $OWT = 5.0\,mm$ & case 1 is absolutely uninteresting due to the almost elastic material response even after 50 cycles; the combination $OWT = 1.0\,mm$ & case 2 does not provides for as high damage as the combination $OWT = 1.0\,mm$ & case 1.

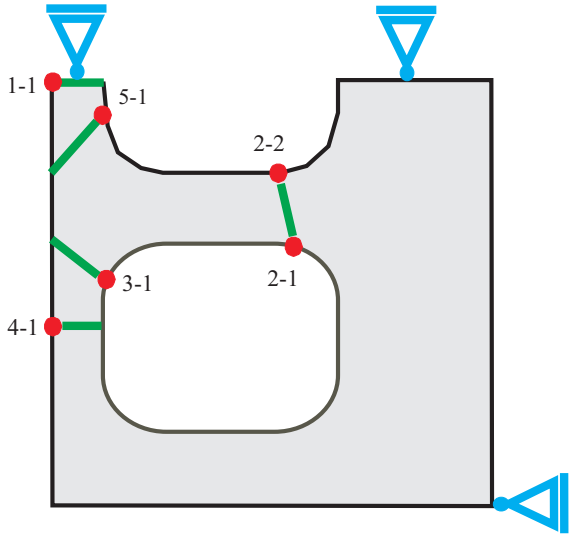

Figure 6.6: Critical points and categorization paths in the 2D finite element model where a localization of inelastic strain and damage occurs. The mechanical constraints are also depicted. Note that only one node is constrained at the bottom right corner.

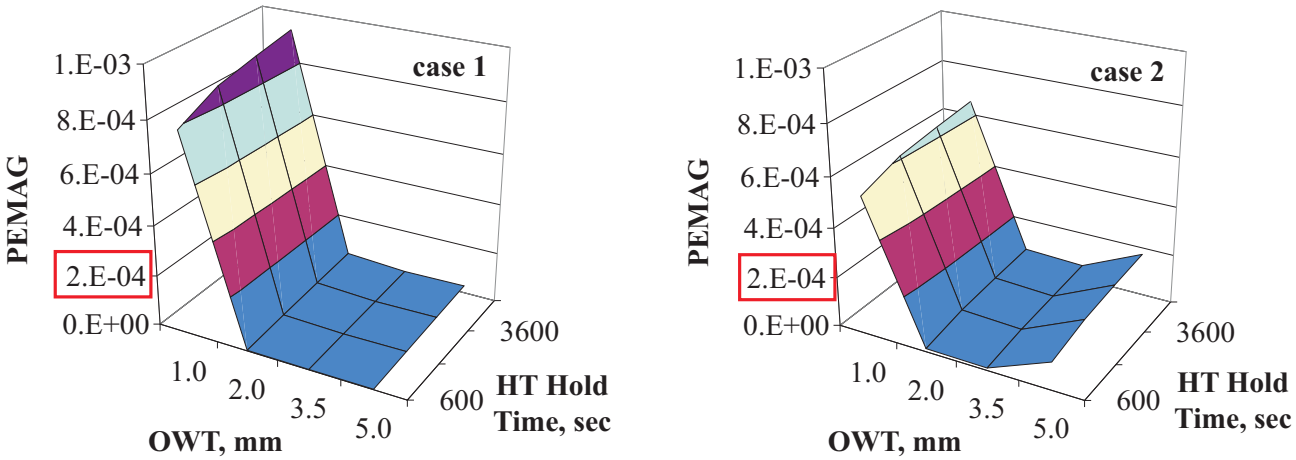

Figure 6.7: The maximum magnitude of inelastic strain in the model depending on two design parameters: t_{hold}^{HT} and OWT.

damage [3] , which is absolutely comparable with the amount reached in the combination $OWT = 1.0\,mm$ & case 1. An important conclusion is thereby that t_{hold}^{HT} influences the accumulation of inelastic strain slightly so that it does not make sense to use the hold times longer than $1800\,sec$.
This proposition is confirmed by evolutions of the von Mises stress depicted in fig. 6.10. Indeed, the stress becomes almost independent of the hold time already after the first 10 - 20 cycles. Note thereby that the cycle with $t_{hold}^{HT} = 7200\,sec$ is approximately 6 times longer than the cycle with $t_{hold}^{HT} = 600\,sec$.

6.5.2 Dependence on the Coolant Pressure

Thus, we have chosen the following combination for a further investigation: $OWT = 5.0\,mm$ & case 2 & $t_{hold}^{HT} = 1800\,sec$. Next, we investigate the sensitivity of the material response concerning the coolant pressure P_{cc} for the chosen combination. Recall that $P_{cc} = 10\,MPa$ was used in all previous simulations.

An analysis of diagrams in fig. 6.11 yield a strong dependence of the von Mises stress, the accumulated plastic strain and the damage variable on the coolant pressure. Thereby, maximum values depend on P_{cc} almost linearly, see fig. 6.12. It means that the coolant pressure should be chosen as high as allowed by the

[3] The corresponding diagrams for the damage variable are represented in fig. B.14.

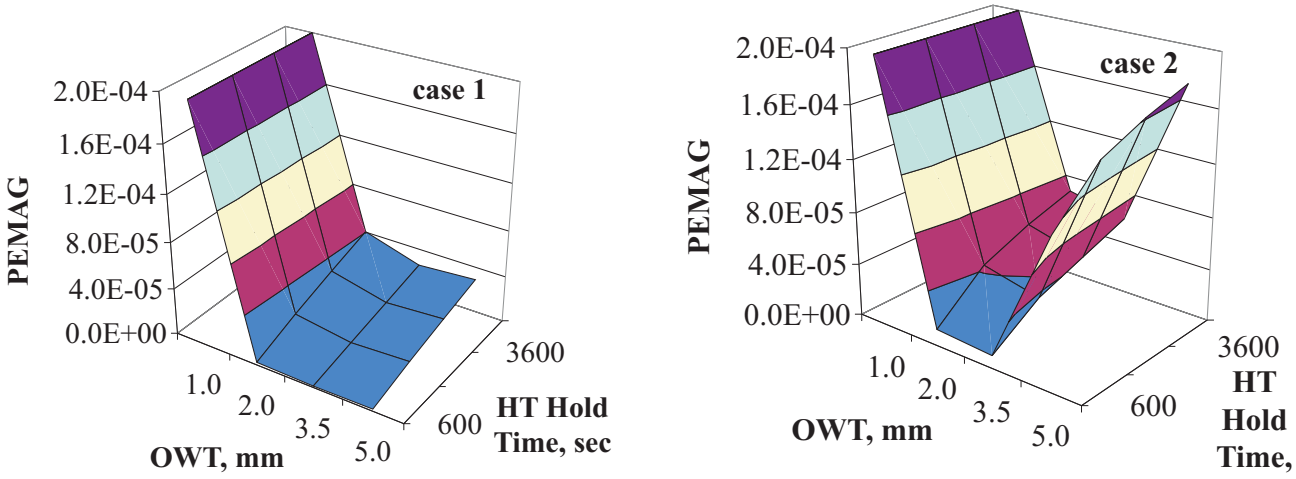

Figure 6.8: Details of fig. B.7: the magnitude of inelastic strain ranges up to $2E-4$.

experimental set-up, at least however $10 - 15\,MPa$.

6.5.3 Dependence on the Temperature Difference in the Cooling Channels

All previous studies have assumed the constant temperatures in cooling channels reported in the beginning of the current chapter: $T_1 = 350°C\ (623\,K)$ & $T_2 = 300°C\ (573\,K)$ corresponding to the case 2. In this subsection, we investigate a change of the material response caused by the change of T_1 as well as the coolant pressure. Thereby, we have simulated additionally the following cases: $T_1 = 450°C\ (723\,K)$ & $T_1 = 550°C\ (823\,K)$ as well as $P_{cc} = 10\,MPa\,,\ 20\,MPa\,,\ 30\,MPa$. Note that $T_2 = 300°C\,(573\,K)$ remains unchanged as well as $t^{HT}_{hold} = 1800\,sec$ and $OWT = 5.0\,mm$.
The new computed temperature distributions corresponding to $T_1 = 450°C\ (723\,K)$ and $T_1 = 550°C\ (823\,K)$ are compared with the previously discussed case $T_1 = 350°C\ (623\,K)$ in fig. 6.13.
The surfaces in fig. 6.14 represent a maximum magnitude of the accumulated inelastic strain (on the left) and the damage variable (on the right) as functions of the coolant pressure and the difference between temperatures in cooling channels. The surfaces can be seen therewith as a generalization of the curves given in fig. 6.12. For the aim of plausibility, we use cross sections of the surfaces for further study, see fig. 6.15. The damage variable and also the accumulated plastic strain is influenced by change in $\Delta T \equiv T_1 - T_2$ evidently stronger than by change in P_{cc}: both internal variables lie within the same order of magnitude for all values of P_{cc} if $\Delta T = const$ and change within approximately 3 orders of magnitude if ΔT increases at constant P_{cc}. For instance, the maximum damage after 50 working cycles is almost independent of the coolant pressure if $\Delta T = 250\,K$. It means that the experimental set-up should be enhanced rather in the way of increasing of the maximum allowable coolant temperature, whereby the coolant pressure can lie at $10\,MPa\ (100\,bar)$. Even if ΔT becomes 100 degrees, the maximum damage increases by approximately 2 orders of magnitude. In other words, the combination $\Delta T = 150\,K$ & $P_{cc} = 10\,MPa$ is more favorable than the combination $\Delta T = 50\,K$ & $P_{cc} = 30\,MPa$ and differs insufficiently from the combination $\Delta T = 150\,K$ & $P_{cc} = 30\,MPa$.
The evolution of the accumulated plastic strain and the damage variable during the first 50 working cycles is shown in fig. 6.16 for different values of ΔT and P_{cc}. The data points used in figs. 6.12 and 6.15 correspond thereby to the cycle 50. Another argument to use higher ΔT follows from the analysis of contour plots depicted in appendix B.4. Indeed, if $\Delta T = 150\,K$ or more, the highest damage occur in the point 2-1 (cf. fig. 6.6) like in the case $OWT = 3.5\,mm$ proposed by designers. Recall that $\Delta T = 50\,K$ leads to the appearance of the highest damage in the point 5-1.

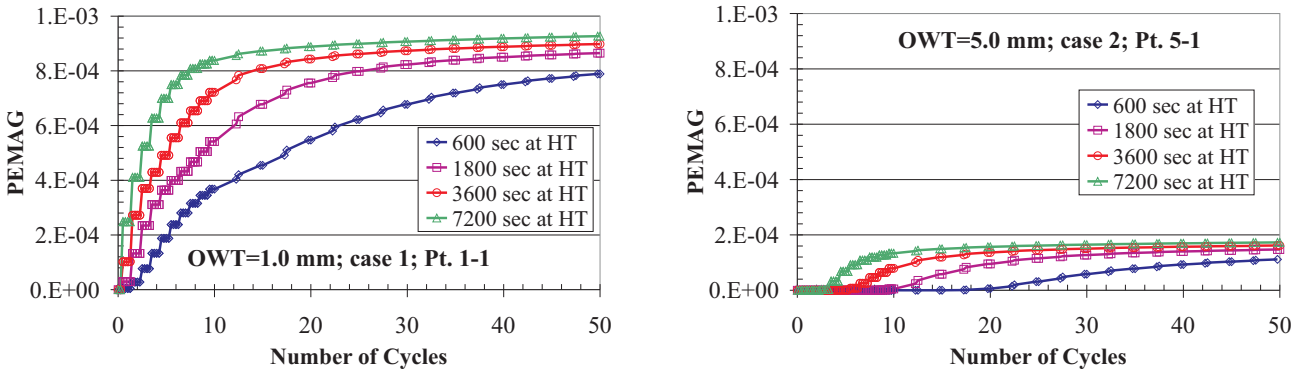

Figure 6.9: An evolution of the amount of inelastic strain in the actual critical point during the first 50 cycles with different t_{hold}^{HT} for the following combinations: $OWT = 1.0\,mm$ & case 1 (on the left) and $OWT = 5.0\,mm$ & case 2.

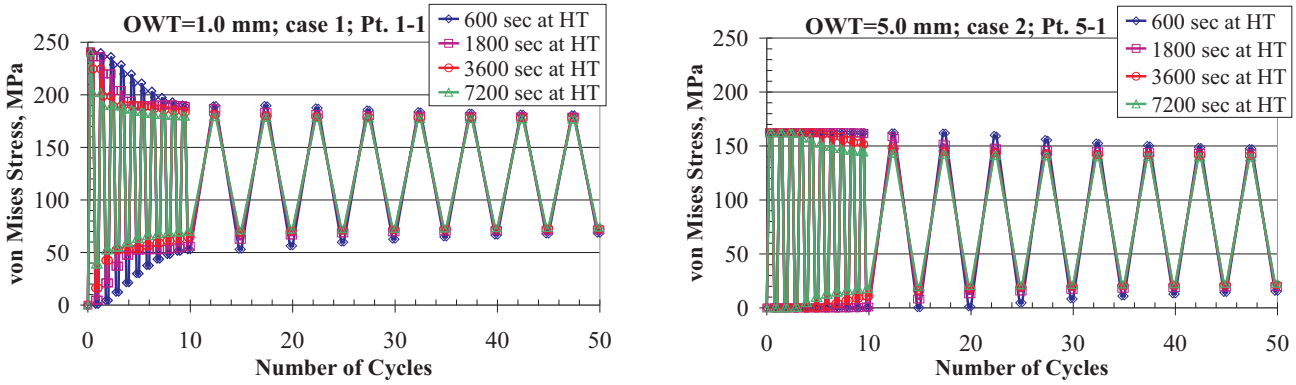

Figure 6.10: An evolution of the von Mises stress in the actual critical point during the first 50 cycles with different t_{hold}^{HT} for the following combinations: $OWT = 1.0\,mm$ & case 1 (on the left) and $OWT = 5.0\,mm$ & case 2.

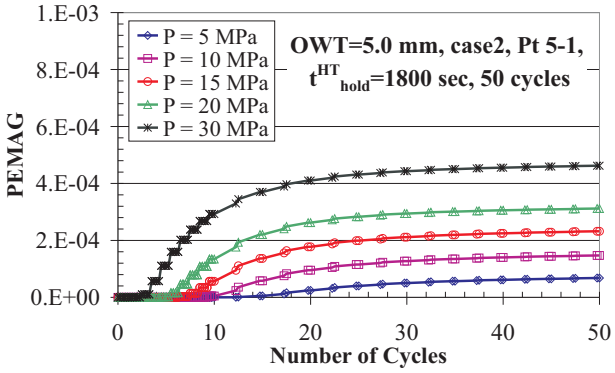

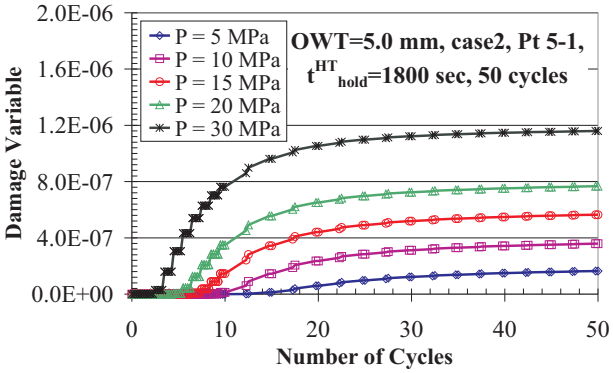

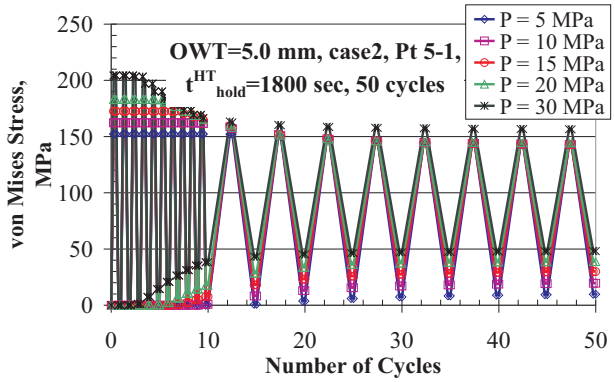

Figure 6.11: Evolutions of the accumulated inelastic strain (top left), damage variable (top right) and von Mises stress for different coolant pressure during the first 50 cycles with $t^{HT}_{hold} = 1800\,sec$ for the following combination: $OWT = 5.0\,mm$ & case 2.

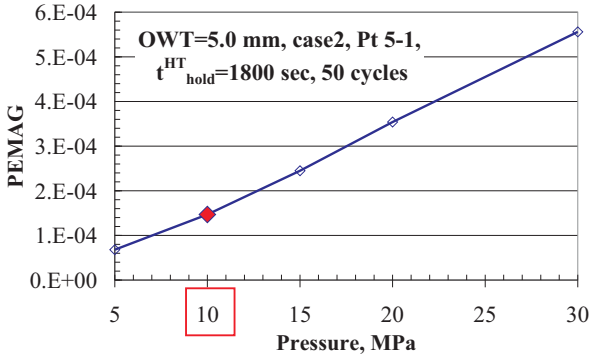

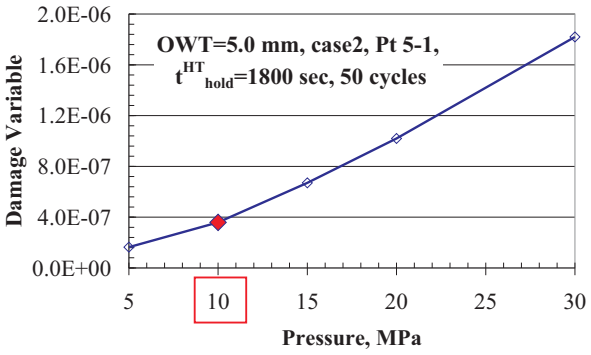

Figure 6.12: The maximum accumulated inelastic strain (on the left) and the maximum damage variable after the first 50 cycles with $t^{HT}_{hold} = 1800\,sec$ as functions of the coolant pressure. The data point corresponding to the coolant pressure used in previous simulations are red-highlighted.

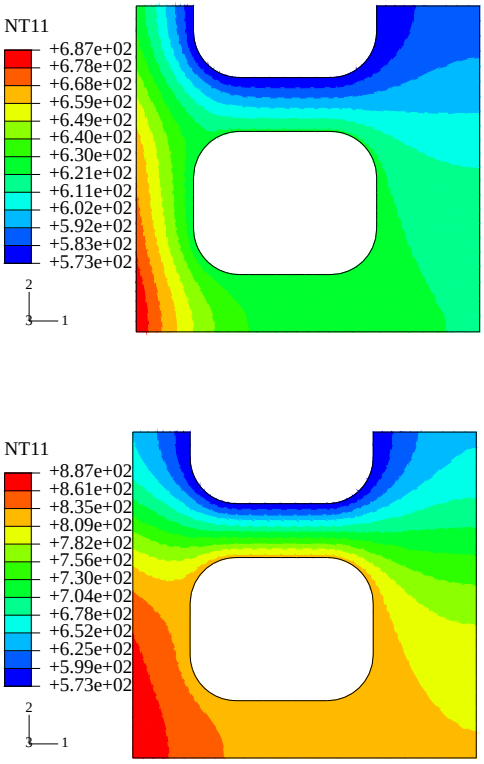

Figure 6.13: Temperature distributions computed using a 2D FE model for three different temperatures in cooling channels corresponding to the case 2: $T_1 = 350°C$ $(623\,K)$ & $T_2 = 300°C$ $(573\,K)$ (top left figure); $T_1 = 450°C$ $(723\,K)$ & $T_2 = 300°C$ $(573\,K)$ (top right figure); $T_1 = 550°C$ $(823\,K)$ & $T_2 = 300°C$ $(573\,K)$ (bottom left figure).

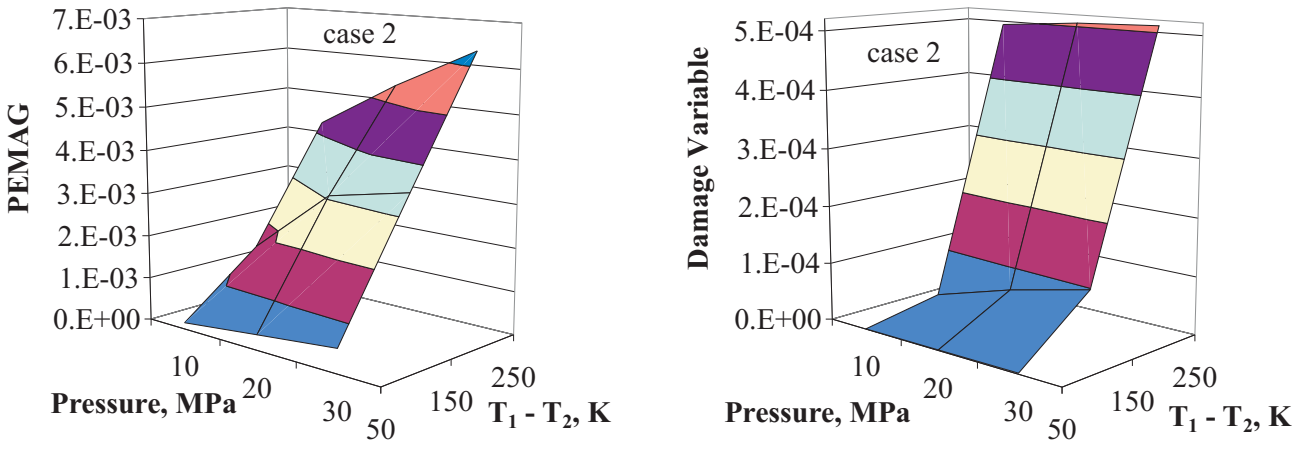

Figure 6.14: Maximum magnitude of inelastic strain (on the left) and damage variable (on the righgt) in the model after the first 50 cycles depending on the coolant pressure P_{cc} and the temperature difference $\Delta T \equiv T_1 - T_2$ between the cooling channels; thereby the following combination is considered: $OWT = 5.0\,mm$ & case 2 & $t_{hold}^{HT} = 1800\,sec$

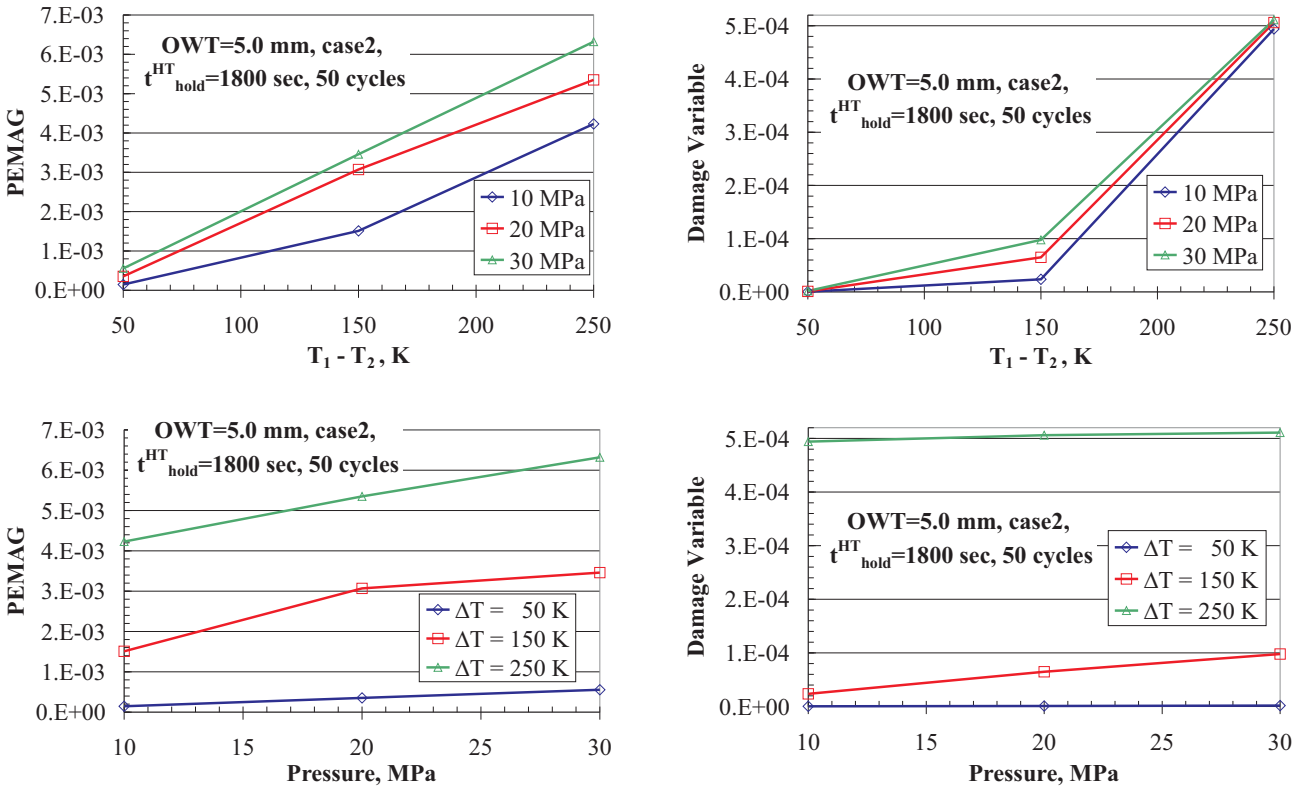

Figure 6.15: Cross sections of the surfaces depicted in fig. 6.14.

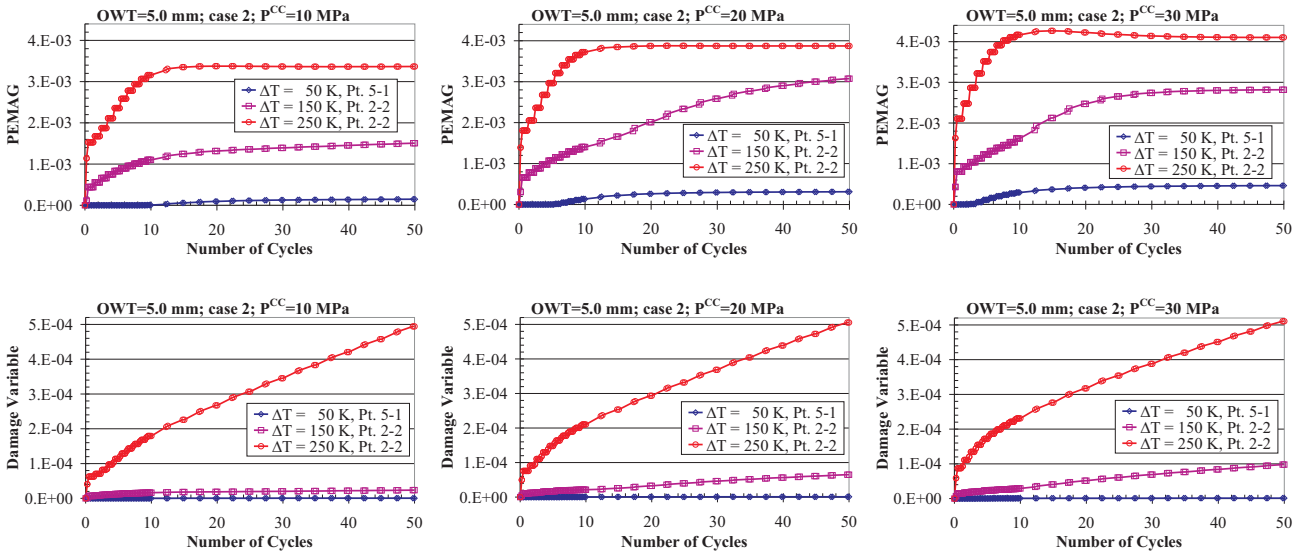

Figure 6.16: Evolutions of the accumulated inelastic strain (top row) and damage variable (bottom row) within the first 50 working cycles for different ΔT and P_{cc}.

Chapter 7

Conclusions and Outlook

In the present work, material parameters required for the non-linear kinematic-isotropic hardening ABAQUS standard material model have been determined. These parameters have been used together with a coupled deformation-damage viscoplastic material model to determine the coolant pressure causing plastic deformation as a function of the temperature in the cooling channels and the plasma heating. Furthermore, the cyclic behavior of the TBM has been simulated using both material models. It turned out that the ABAQUS standard material model used is not appropriate enough to describe behavior of components undergoing different loadings at HT for a longer time. However, this time-independent material model can be involved for simulations under monotonic loadings to verify the low-temperature rules for the M-type damage requiring a pure plastic strain part without the creep part.

On the other hand, some important design rules have been applied to the model and their predictions have been compared with results of the cyclic simulations. It thereby turned out that the criterions are not fulfilled, even if the conventional limit values of stress intensities are used. The newly calculated values of allowable stress intensities S_m^C, S_e^C and S_d^C accounting for the cyclic softening of the EUROFER 97 lead to a larger gap between the target and actual results.

An investigation of the temperature dependence of the allowable stress intensities shows that cyclic loadings lead to a reduction of conventional values of e.g. S_m by approximately 40-$80\,MPa$. For this reason, we would recommend to use the available values to design a component underlying to monotonic loadings and the proposed values S_m^C if cyclic loadings occur.

The results of the cyclic simulations exhibit neither plastic collapse nor ratcheting after the first 600 cycles. This discrepancy could mean that the criterions could be possibly too conservative for EUROFER 97 and should be revised. The suggestion, however, requires a further in-depth study including a verification of all (elastic and elastic-plastic) design rules preventing both the M-type and C-type damage, a consideration of the effects of irradiation, the hydrogen effect, and corrosion effect by the coolant as well as the possible changes in the actual TBM geometry.

On the basis of several thermal, linear-elastic and cyclic simulations based on a coupled deformation damage material model with consideration of creep we propose the following parameters for the mock-up model of the TBM, cf. fig. 6.1:

- case 2 for the surface temperature of the cooling channels i.e. $T_1 = 450°C\ (723\,K)$ & $T_2 = 300°C\ (573\,K)$ [1];
- the outer wall thickness $OWT = 5.0\,mm$;

[1] Evidently, higher $T_1 = 550°C\ (823\,K)$ results sufficiently in a reduction of the number of cycles up to the failure of the model. The temperature should be however realizable experimentally.

- the hold time at the high temperature $t_{hold}^{HT} = 1800\,sec$;
- the coolant pressure P_{cc} at least $10\,MPa$ i.e. $100\,bar$.

If $T_1 = 450°C\ (723\,K)$ is not realizable and only $T_1 = 350°C\ (623\,K)$ can be reached experimentally, P_{cc} should be increased up to at least $15 - 20\,MPa$ i.e. $150 - 200\,bar$.

For the modeling, we have used geometrical parameters corresponding to actual propositions of TBM designers. Among all these parameters, we have varied only the outer wall thickness OWT. The heating of the front side is considered to be constant and equal to $300\,kW/m^2$. We recall also another model assumption concerning the constant temperature over the total surface of a cooling channel. Thereby, surface temperatures in different cooling channels should not be equivalent, see fig. 6.1.

We also found out that t_{hold}^{HT} influences damage amount only slightly in contrast to OWT and P_{cc} and, on the other hand, ΔT influences damage more sufficient than P_{cc}.

Further design propositions can occur due to a variation of other geometrical parameters, plasma heating, a simulation of more cycles using both the RESTART option and the extrapolation method. Moreover, the temperature on the surface of the cooling channels is not constant and should be determined on the basis of a thermo-hydraulic simulation.

Appendix A

Additions to the TBM Part

A.1 Parameters for both Material Models.

Table A.1: Parameters for the ABAQUS standard hardening material model; $\gamma = 1150$ for all T.

$T\,,K$	293	723	823	923
$C\,,MPa$	147200	153922	180590	194900
$Q\,,MPa$	-104.00	-133.00	-145.00	-108.77
b	0.89	1.05	1.80	3.70

Table A.2: Parameters for the coupled deformation-damage material model

Material	F82H mod			EUROFER 97	
$T\,,°C$	450	550	650	450	550
$E\,,\,MPa$	176170	160000	137450	166300	153890
$k\,,\,MPa$	5.57	1.3E-6	2.14E-5	175	6E-6
$Z\,,\,MPa \cdot sec^{1/n}$	391.6	524	600	177.6	428
n	31.8	11.7	6.66	13.7	12.6
$H\,,\,MPa$	104823	78708	75646	115508	98391
D	619	692	1046	704	764
$R\,,\,MPa^{1-m} \cdot sec^{-1}$	1.0E-21	9.9E-17	8.0E-17	4.0E-17	1.0E-16
m	8.67	0.428	0.397	6.1	0.428
h	1.70E-3	1.87E-3	4.25E-3	1.85E-5	9.80E-4
c	6.30	5.02	6.21	1.82	3.62
$r_\psi\,,\,sec^{-1}$	8.27E-5	1.03E-4	2.00E-5	7.00E-5	1.00E-4
ψ_r	0.501	0.519	1E-4	0.622	0.542
m_ψ	1.0	1.0	1.0	1.0	1.0
$\psi_{s,\infty}$	0.308	0.346	0.377	0.293	0.350
c_s	2452	3000	2814	2764	2507
$A\,,\,MPa \cdot sec^{1/r}$	2293	1592	1391	2202	2057
r	2.91	2.64	2.34	2.91	2.25
κ	33.51	12.64	12.44	33.51	12.25

A.2 Maximum von Mises Stress vs. Pressure in Cooling Channels.

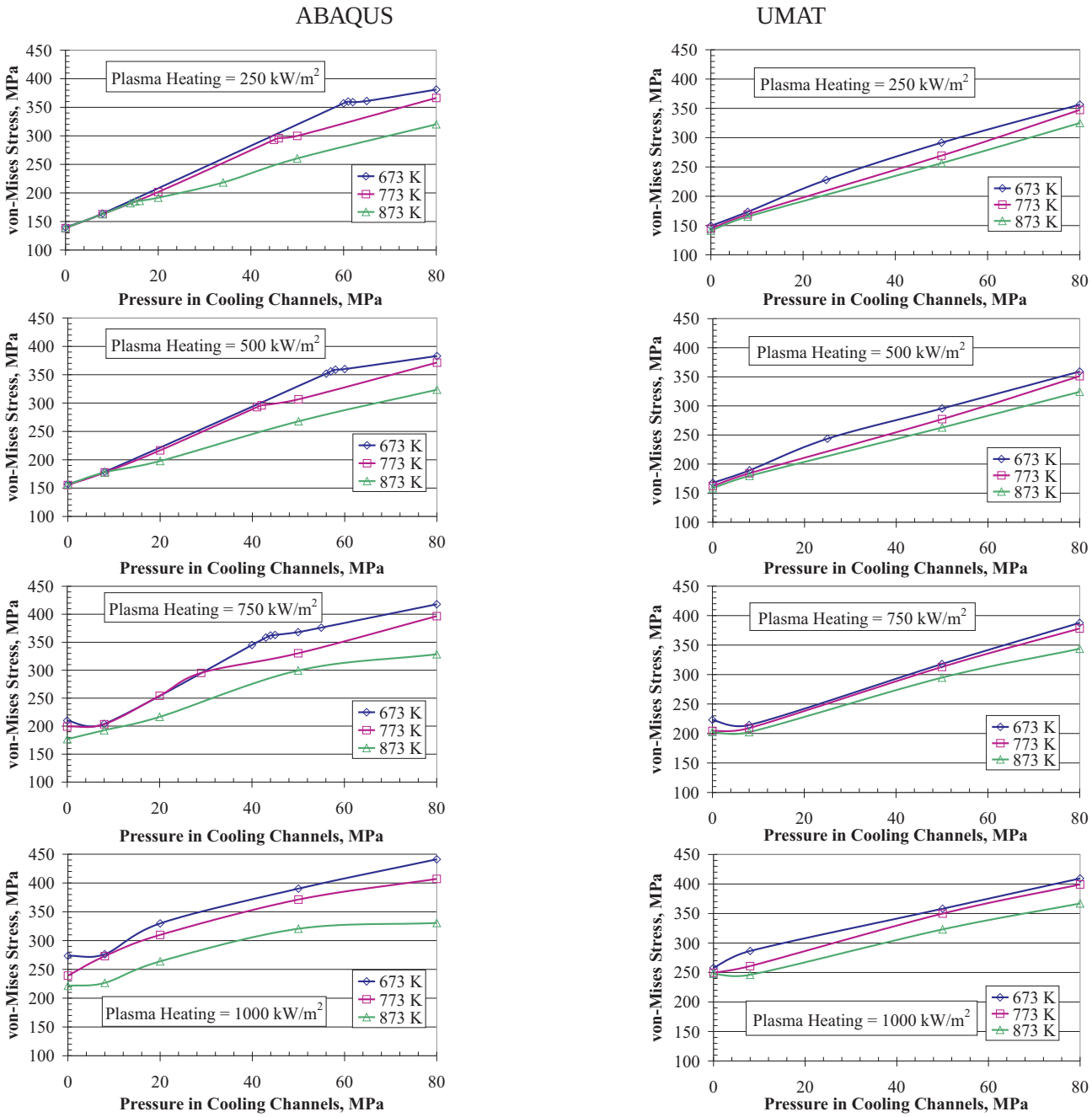

Figure A.1: The max. von Mises stress as a function of the pressure in cooling channels obtained using the ABAQUS standard material model (the left column) and the UMAT for different values of the plasma heating and different T^{cc}.

A.3 Distribution of the von Mises Stress at $T^{cc} = 773\,K$ after the 1^{st} Cycle for Different Values of the Plasma Heating and two Levels of the Pressure obtained using the ABAQUS Standard Material Model

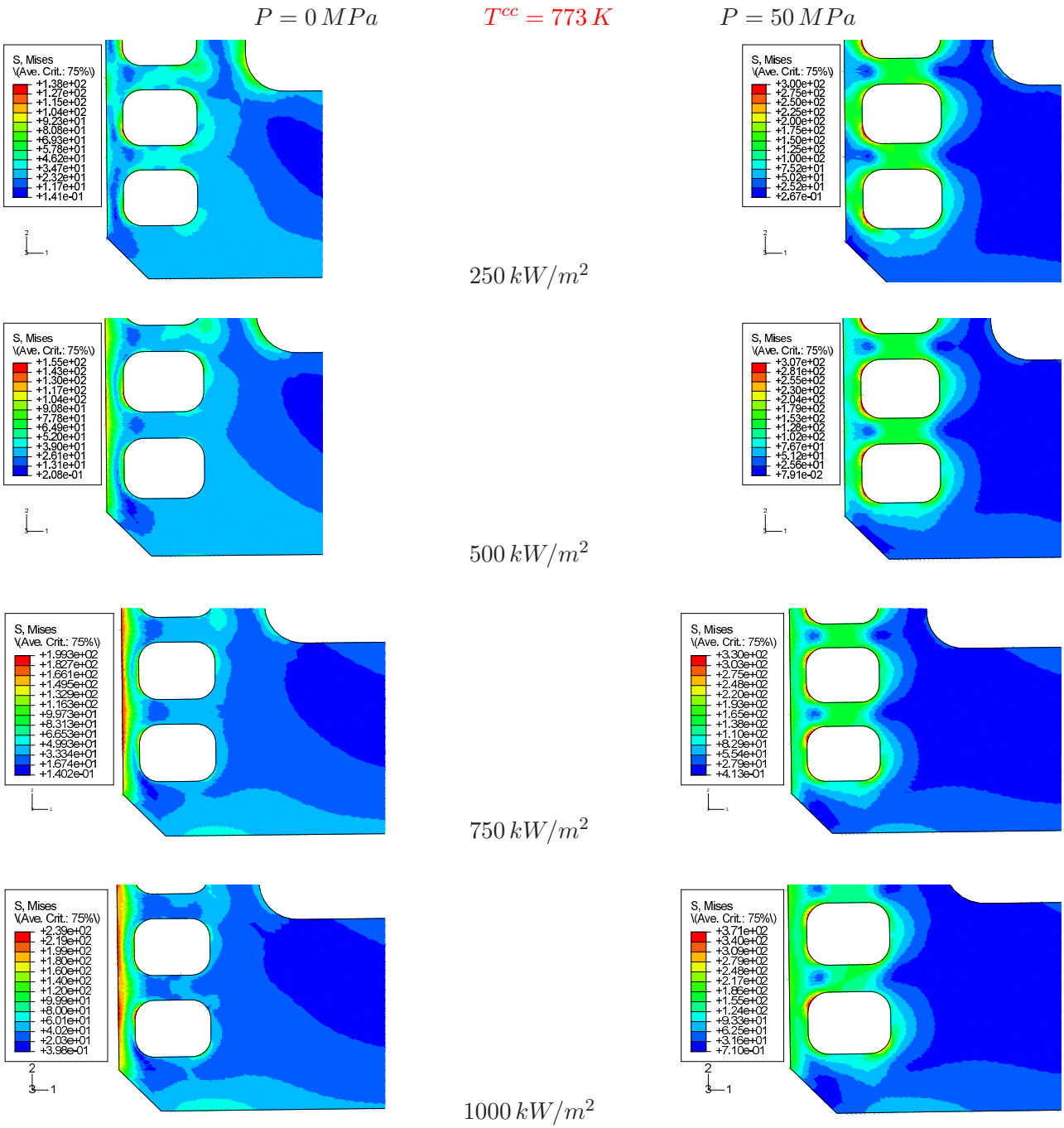

Figure A.2: Distributions of the von Mises stress at $T^{cc} = 773\,K$ under consideration of the plasma heating from $250\,kW/m^2$ up to $1000\,kW/m^2$ without pressure in cooling channels (the left-hand side column) and with the pressure of $50\,MPa$.

A.4 Distribution of the von Mises Stress and the Equivalent Plastic Strain for Different Steps of the Cycle 300 obtained using both Material Models.

cycle 300 $750\,kW/m^2$ $T^{cc} = 873\,K$ $P = 50\,MPa$

ABAQUS UMAT

step1:
after the heating

$\sigma^{max}_{vm\,UMAT} = 154\,MPa$

$\sigma^{max}_{vm\,ABAQ} = 287\,MPa$

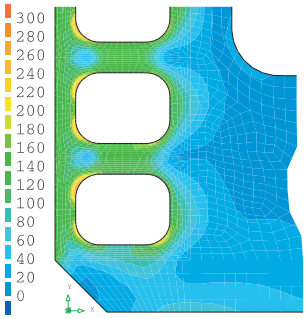

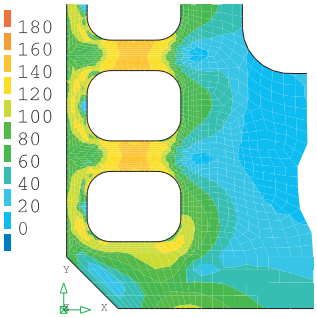

step2:
after the holding at the HT

$\sigma^{max}_{vm\,UMAT} = 154\,MPa$

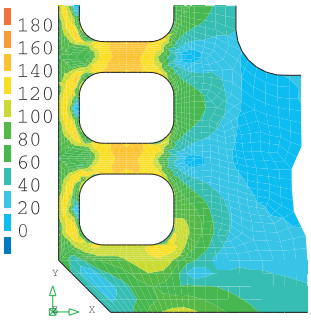

step3:
after the cooling

$\sigma^{max}_{vm\,UMAT} = 212\,MPa$

$\sigma^{max}_{vm\,ABAQ} = 125\,MPa$

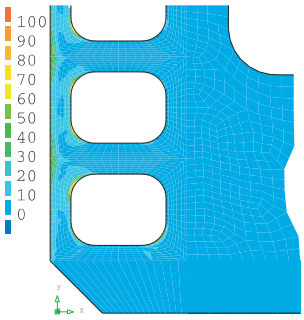

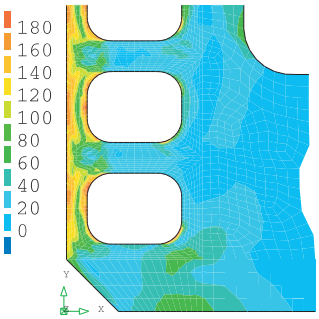

step4:
after the holding at the RT

$\sigma^{max}_{vm\,UMAT} = 192\,MPa$

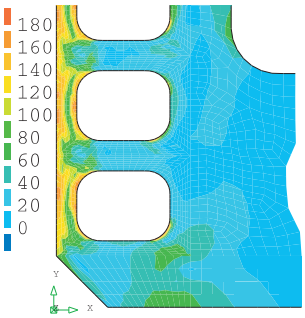

Figure A.3: Distribution of the von Mises stress during the cycle 300 obtained using the ABAQUS standard material model (on the left) as well as the UMAT under consideration of the plasma heating of $750\,kW/m^2$, $T^{cc} = 873\,K$ and the pressure in cooling channels of $50\,MPa$

cycle 300 $750\,kW/m^2$ $T^{cc} = 873\,K$ $P = 50\,MPa$

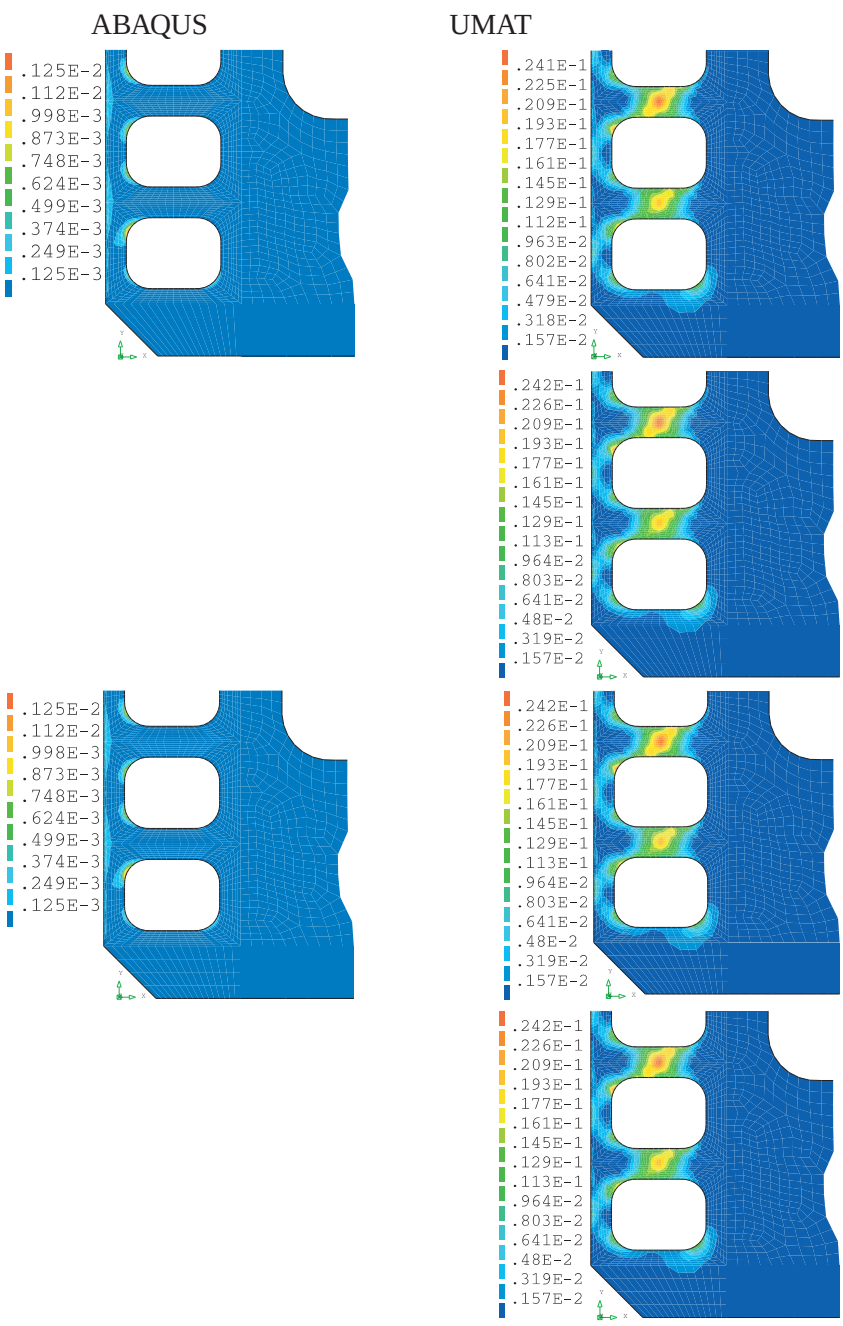

step1:
after the heating

$\overline{\epsilon}^{max}_{pl\ UMAT} = 2.57E-2$

$\overline{\epsilon}^{max}_{pl\ ABAQ} = 1.37E-3$

step2:
after the holding at the HT

$\overline{\epsilon}^{max}_{pl\ UMAT} = 2.58E-2$

step3:
after the cooling

$\overline{\epsilon}^{max}_{pl\ UMAT} = 2.58E-2$

$\overline{\epsilon}^{max}_{pl\ ABAQ} = 1.37E-3$

step4:
after the holding at the RT

$\overline{\epsilon}^{max}_{pl\ UMAT} = 2.58E-2$

Figure A.4: Distribution of the equivalent plastic strain during the cycle 300 obtained using the ABAQUS standard material model (on the left) as well as the UMAT under consideration of the plasma heating of $750\,kW/m^2$, $T^{cc} = 873\,K$ and the pressure in cooling channels of $50\,MPa$

A.5 Distribution of the von Mises Stress, the Equivalent Plastic Strain for Different Steps of Chosen Cycles obtained using both Material Models.

$750\,kW/m^2$ $T^{cc} = 873\,K$ $P = 50\,MPa$

ABAQUS UMAT

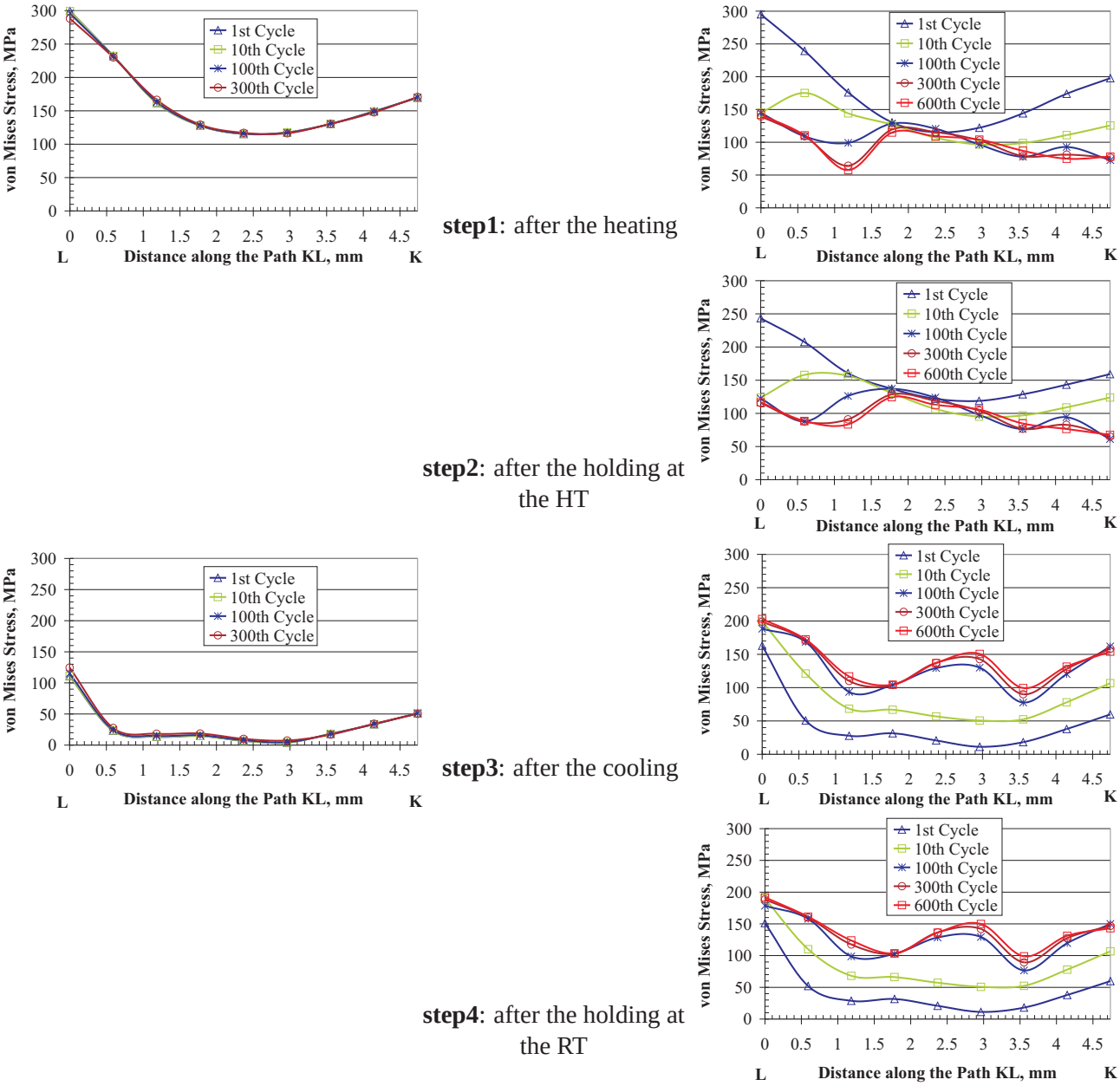

step1: after the heating

step2: after the holding at the HT

step3: after the cooling

step4: after the holding at the RT

Figure A.5: Distribution of the von Mises stress along KL during some chosen cycles obtained using the ABAQUS standard material model (on the left) and the UMAT under consideration of the plasma heating of $750\,kW/m^2$, $T^{cc} = 873\,K$ and the pressure in cooling channels of $50\,MPa$

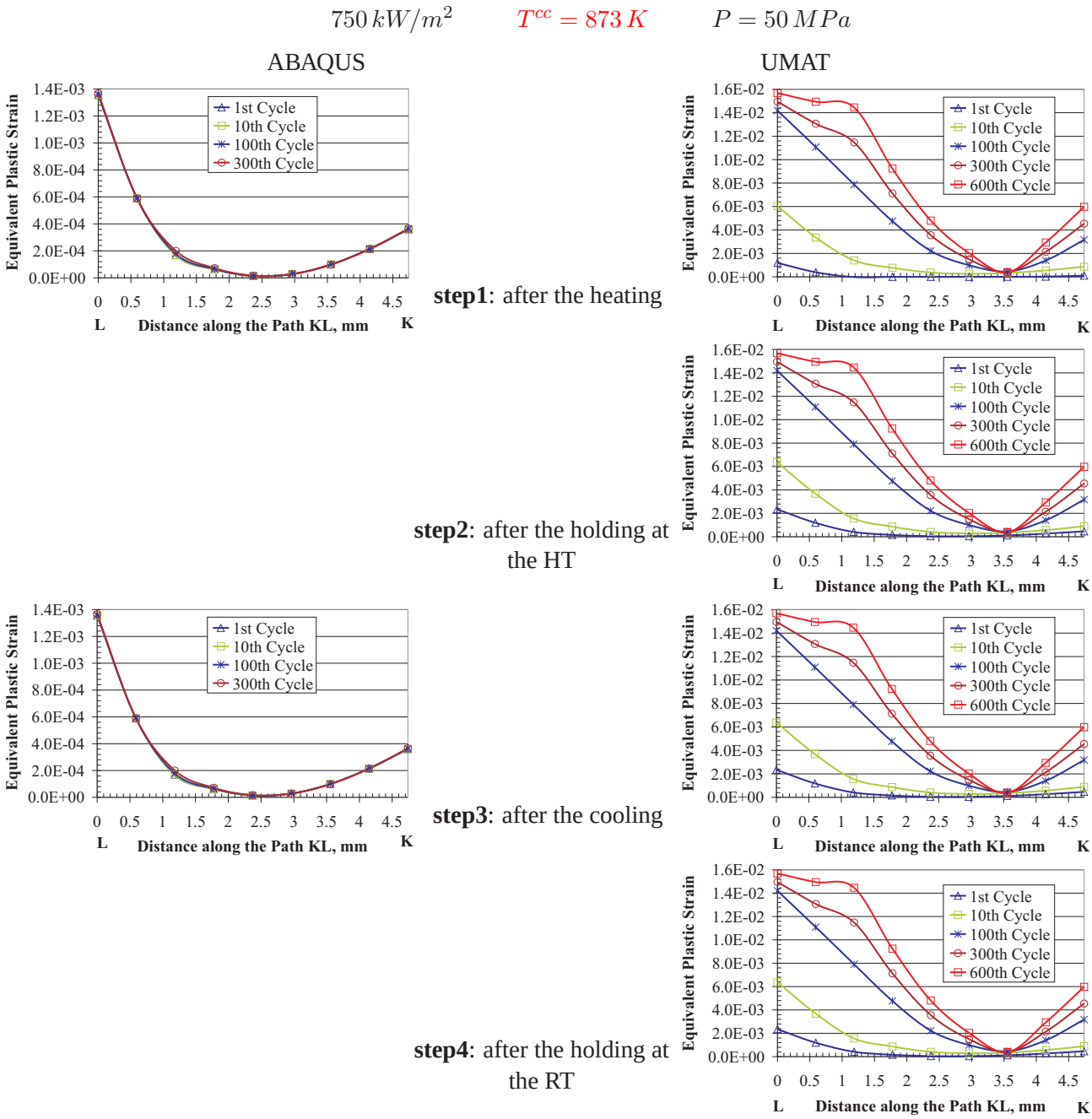

Figure A.6: Distribution of the equivalent plastic strain along KL during some chosen cycles obtained using the ABAQUS standard material model (on the left) and the UMAT under consideration of the plasma heating of $750\,kW/m^2$, $T^{cc} = 873\,K$ and the pressure in cooling channels of $50\,MPa$

Appendix B

Additions to the Mock-Up Part

B.1 Illustrations on the 3D Thermal and Linear-Elastic Simulations

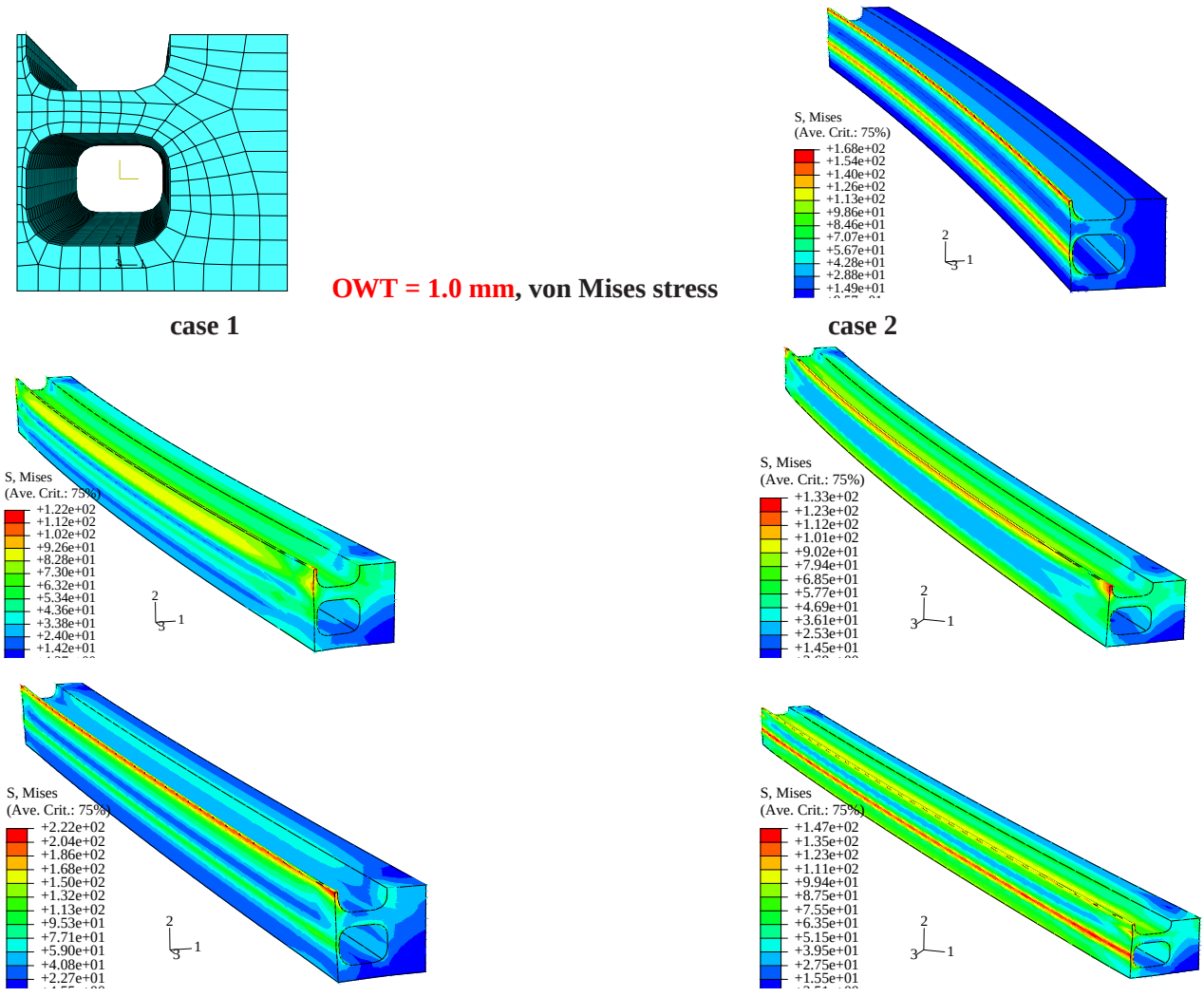

Figure B.1: The discretized FE model (1^{st} row on the left); the v. Mises stress distr. due to only the coolant pressure P^{cc} (1^{st} row on the right); von Mises stress distr. due to only the temperature gradients ΔT (2^{nd} row) and both P^{cc} and ΔT acting simultaneously (3^{rd} row). The left and the right columns correspond to the case 1 and 2 resp.

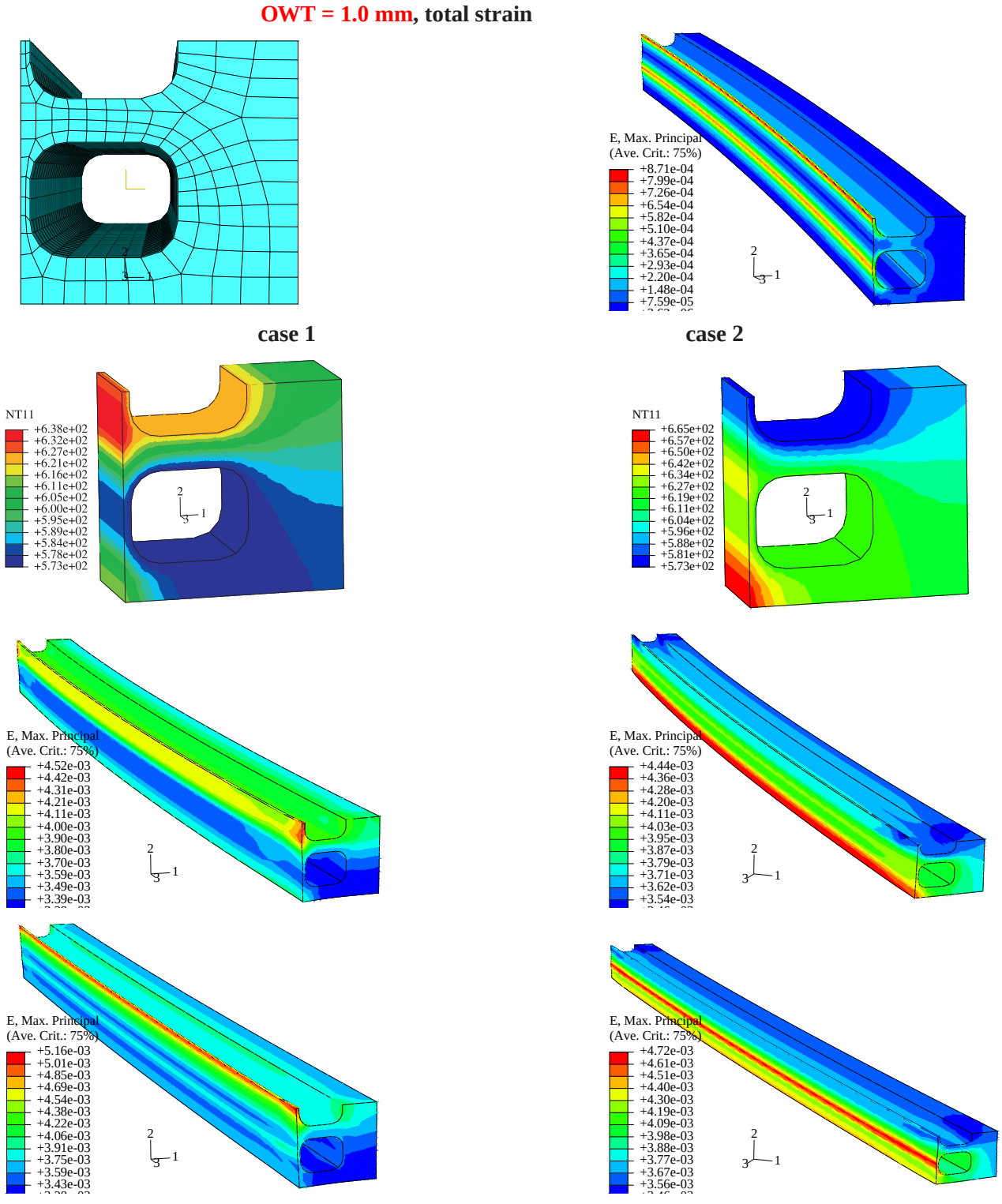

Figure B.2: The discretized FE model (1^{st} row on the left); the maximum principal total strain distribution due to only the coolant pressure P^{cc} (1^{st} row on the right); temperature distributions (in K) for the cases 1 and 2 (2^{nd} row on the left and on the right respectively); maximum principal total strain distributions due to only the temperature gradients ΔT (3^{rd} row) and both P^{cc} and ΔT acting simultaneously (4^{th} row). The left and the right columns correspond to the case 1 and 2 respectively.

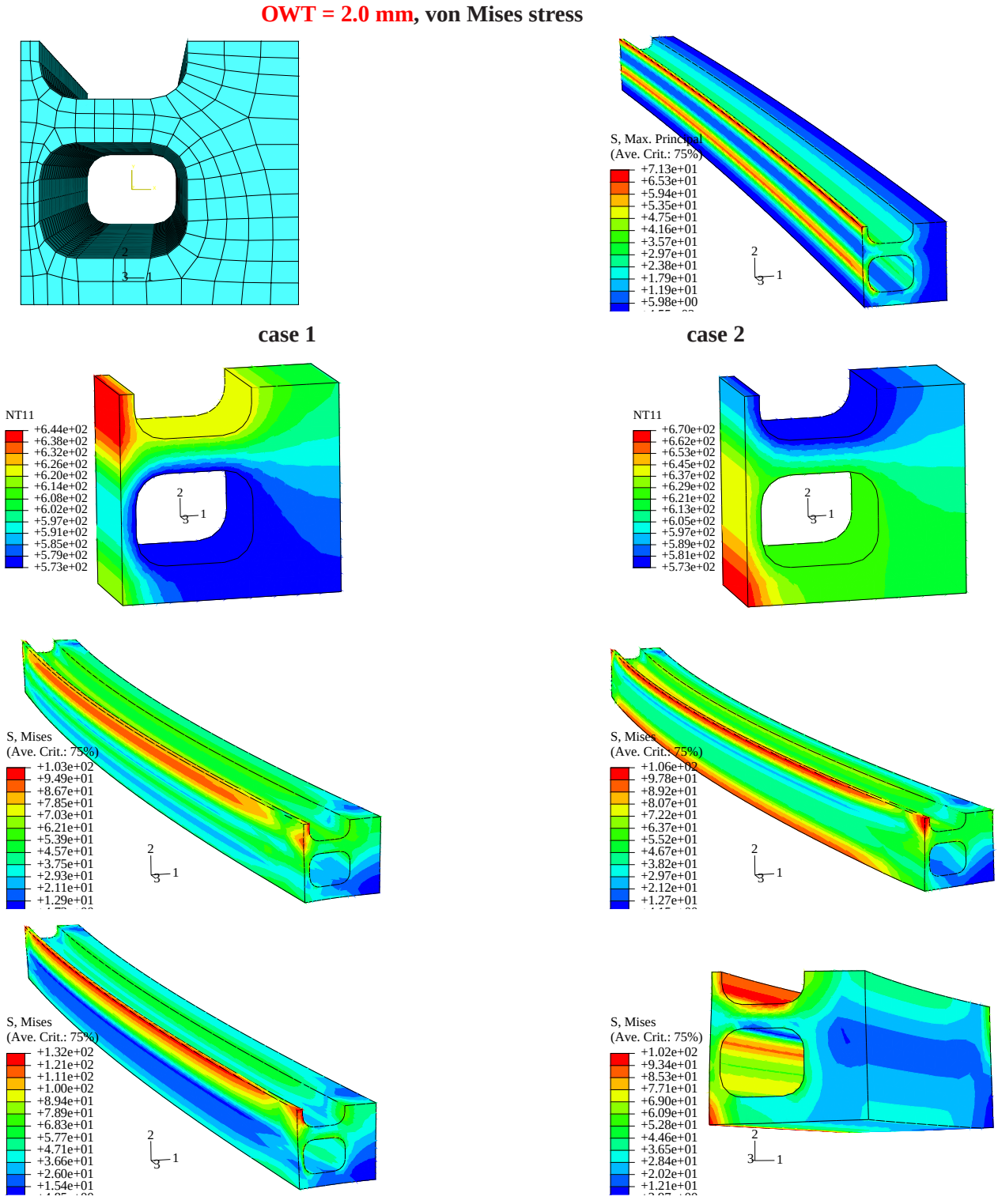

Figure B.3: The discretized FE model (1^{st} row on the left); the von Mises stress distribution due to only the coolant pressure P^{cc} (1^{st} row on the right); temperature distributions (in K) for the cases 1 and 2 (2^{nd} row on the left and on the right respectively); von Mises stress distributions due to only the temperature gradients ΔT (3^{rd} row) and both P^{cc} and ΔT acting simultaneously (4^{th} row). The left and the right columns correspond to the case 1 and 2 respectively.

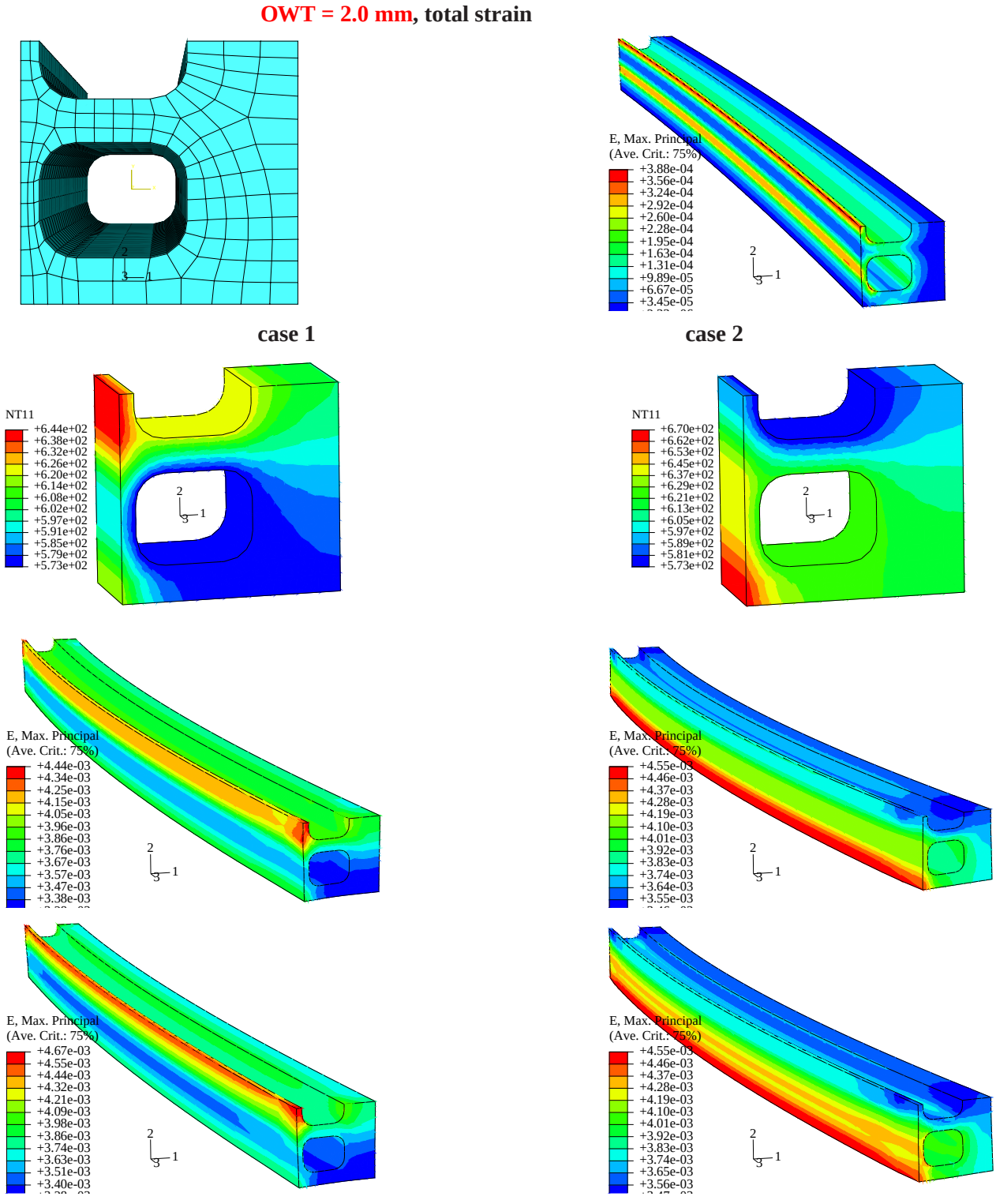

Figure B.4: The discretized FE model (1^{st} row on the left); the maximum principal total strain distribution due to only the coolant pressure P^{cc} (1^{st} row on the right); temperature distributions (in K) for the cases 1 and 2 (2^{nd} row on the left and on the right respectively); maximum principal total strain distributions due to only the temperature gradients ΔT (3^{rd} row) and both P^{cc} and ΔT acting simultaneously (4^{th} row). The left and the right columns correspond to the case 1 and 2 respectively.

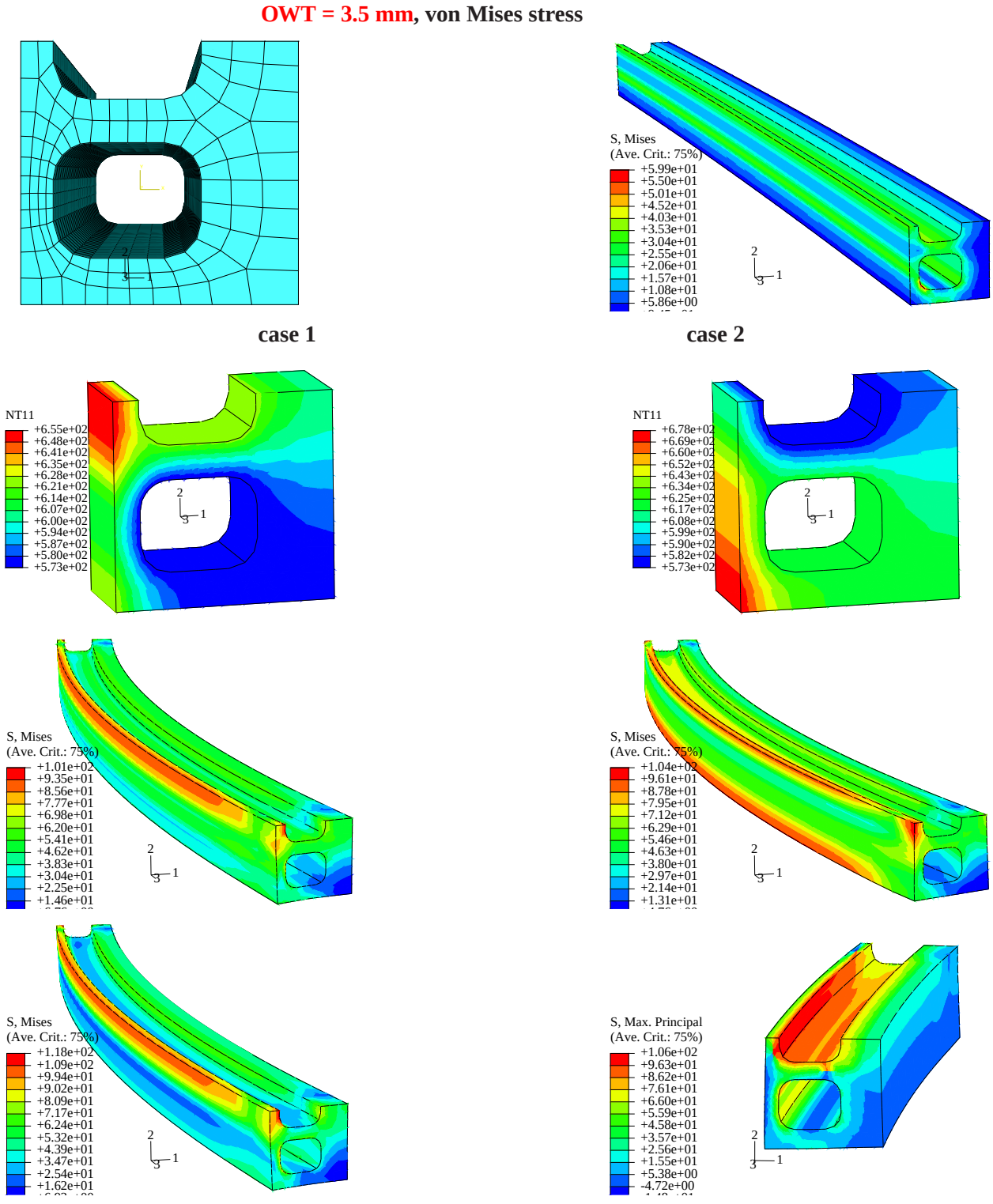

Figure B.5: The discretized FE model (1^{st} row on the left); the von Mises stress distribution due to only the coolant pressure P^{cc} (1^{st} row on the right); temperature distributions (in K) for the cases 1 and 2 (2^{nd} row on the left and on the right respectively); von Mises stress distributions due to only the temperature gradients ΔT (3^{rd} row) and both P^{cc} and ΔT acting simultaneously (4^{th} row). The left and the right columns correspond to the case 1 and 2 respectively.

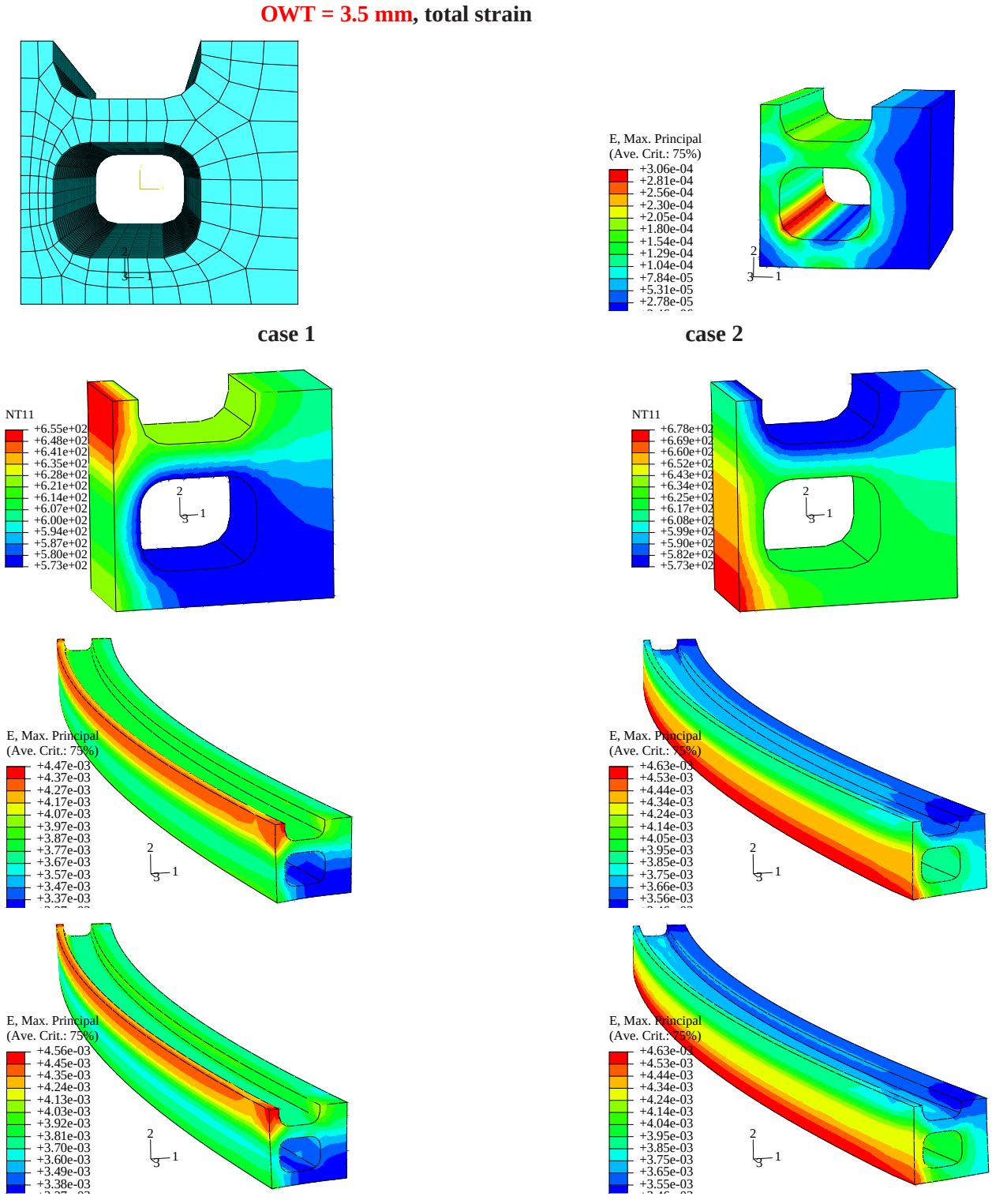

Figure B.6: The discretized FE model (1^{st} row on the left); the maximum principal total strain distribution due to only the coolant pressure P^{cc} (1^{st} row on the right); temperature distributions (in K) for the cases 1 and 2 (2^{nd} row on the left and on the right respectively); maximum principal total strain distributions due to only the temperature gradients ΔT (3^{rd} row) and both P^{cc} and ΔT acting simultaneously (4^{th} row). The left and the right columns correspond to the case 1 and 2 respectively.

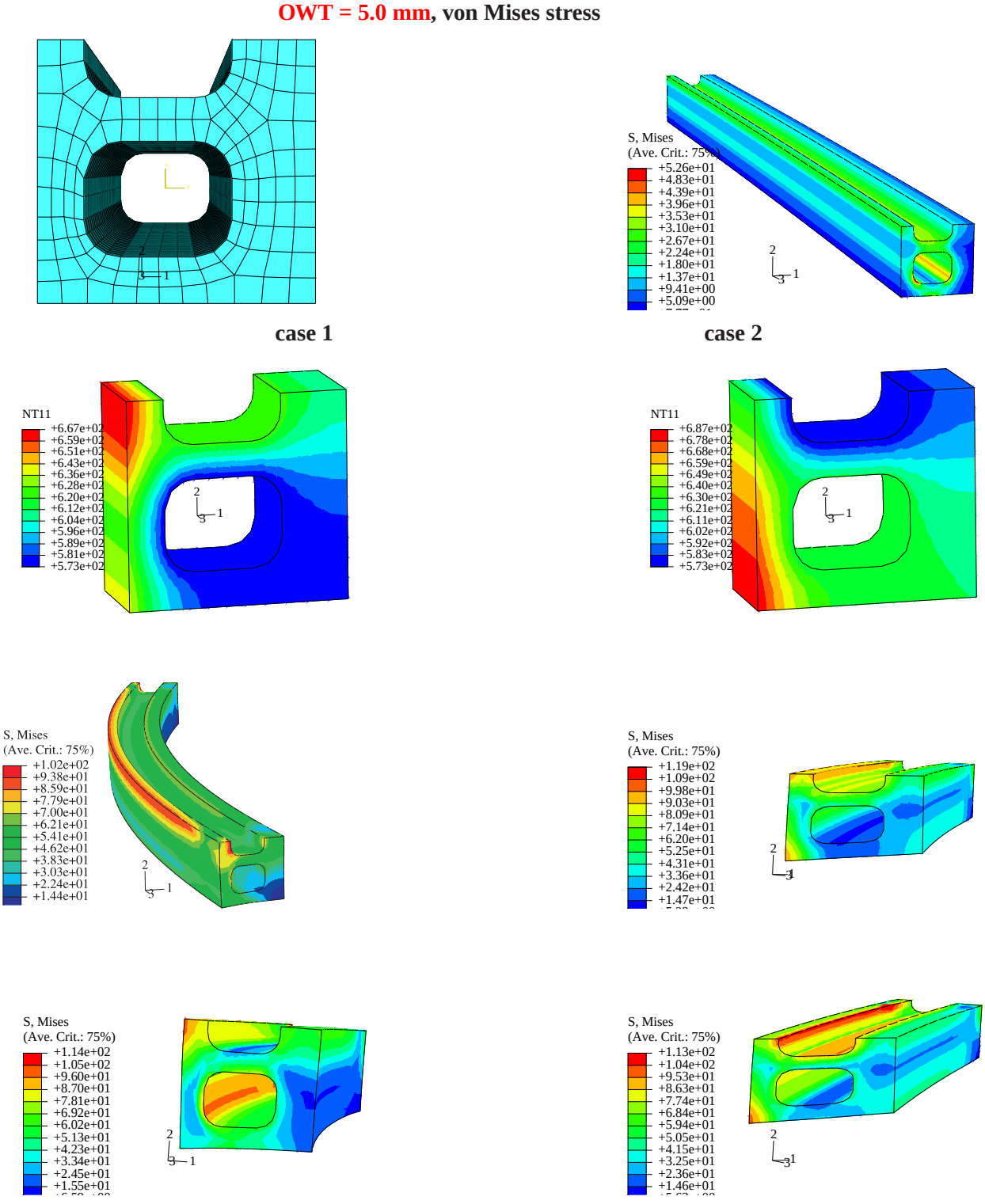

Figure B.7: The discretized FE model (1^{st} row on the left); the von Mises stress distribution due to only the coolant pressure P^{cc} (1^{st} row on the right); temperature distributions (in K) for the cases 1 and 2 (2^{nd} row on the left and on the right respectively); von Mises stress distributions due to only the temperature gradients ΔT (3^{rd} row) and both P^{cc} and ΔT acting simultaneously (4^{th} row). The left and the right columns correspond to the case 1 and 2 respectively.

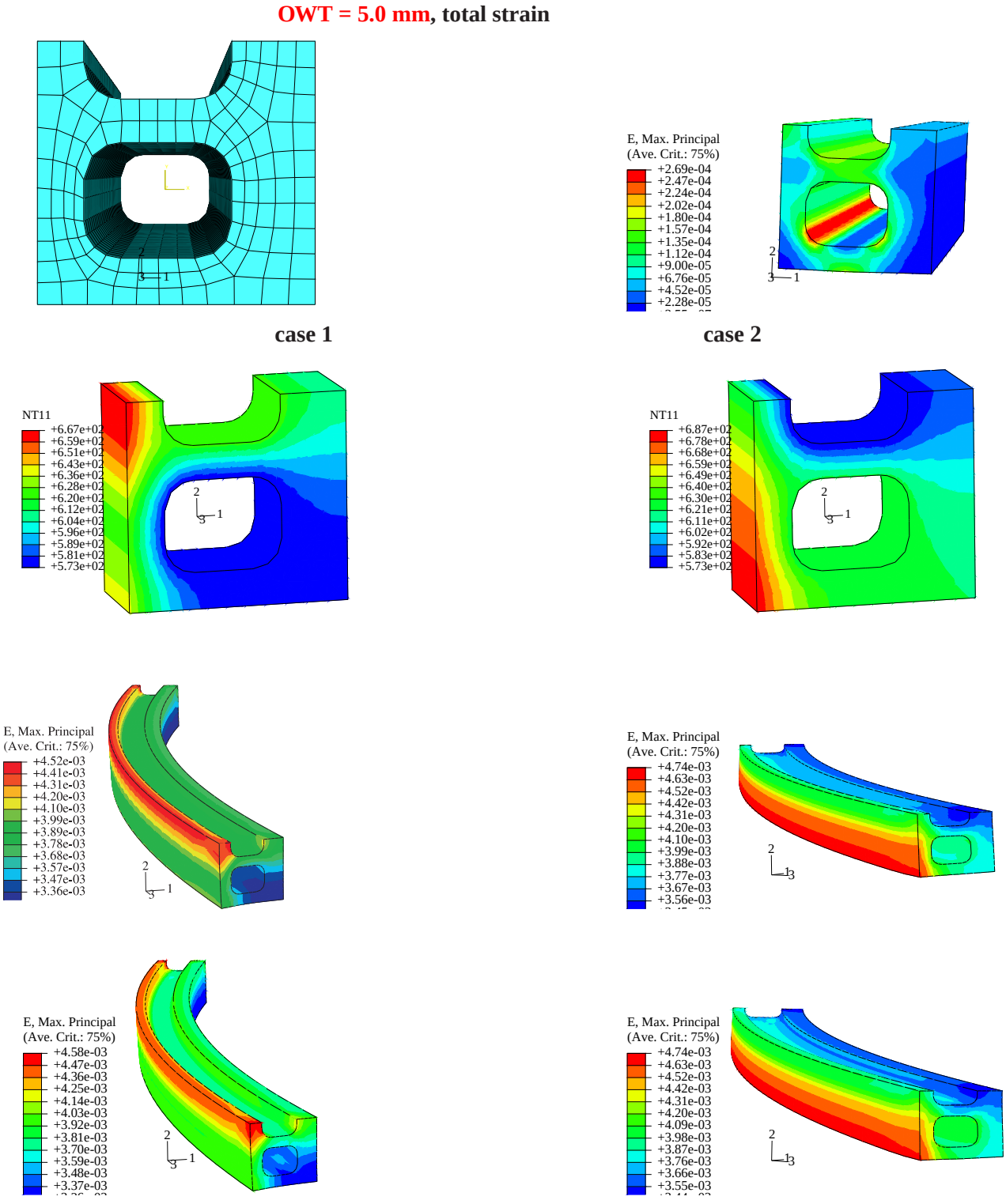

Figure B.8: The discretized FE model (1^{st} row on the left); the maximum principal total strain distribution due to only the coolant pressure P^{cc} (1^{st} row on the right); temperature distributions (in K) for the cases 1 and 2 (2^{nd} row on the left and on the right respectively); maximum principal total strain distributions due to only the temperature gradients ΔT (3^{rd} row) and both P^{cc} and ΔT acting simultaneously (4^{th} row). The left and the right columns correspond to the case 1 and 2 respectively.

B.2 Contour Plots on the Cyclic Simulations using the UMAT, $T_1 = 350°C\,(623\,K)$

cycle 50, step 2, $t_{hold}^{HT} = 7200\,sec$**,** $P^{cc} = 10\,MPa$

case 1 **von Mises stress** **case 2**

$OWT = 1.0\,mm$

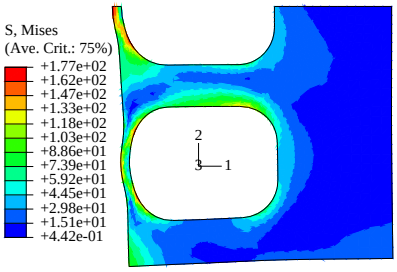

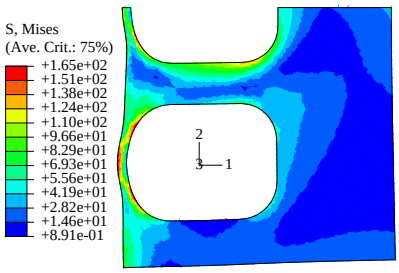

$OWT = 2.0\,mm$

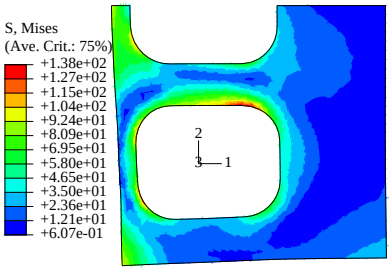

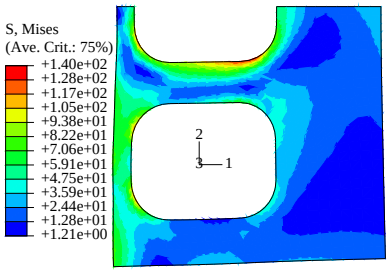

$OWT = 3.5\,mm$

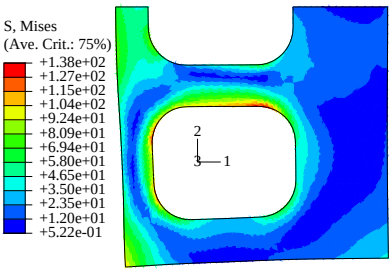

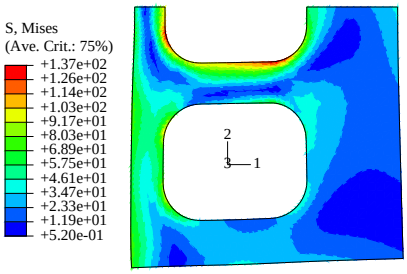

$OWT = 5.0\,mm$

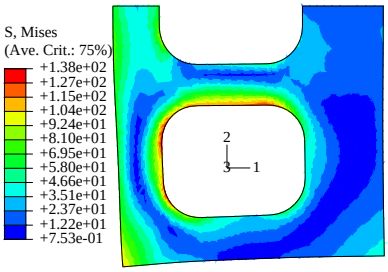

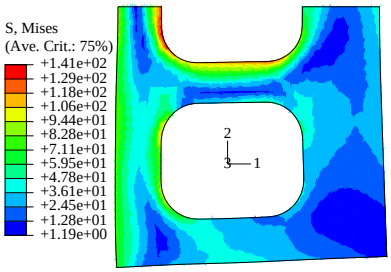

Figure B.9: Distr. of the v. Mises stress after the holding at the HT during the cycle 50 for different values of the OWT if $t_{hold}^{HT} = 7200\,sec$ and $P_{cc} = 10\,MPa$. The left and the right columns correspond to the case 1 and 2 resp..

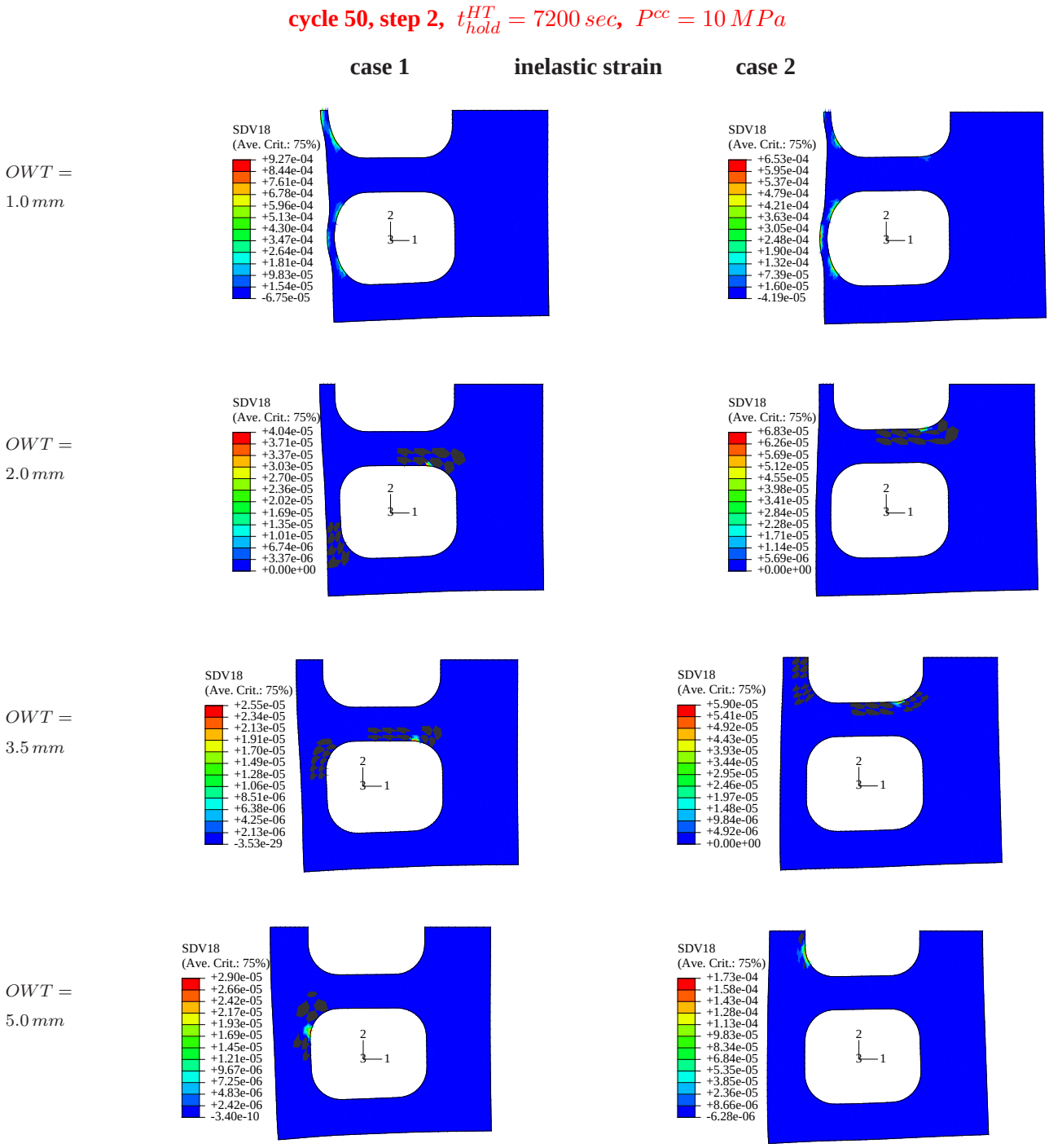

Figure B.10: Distributions of the inelastic strain magnitude after the holding at the HT during the cycle 50 for different values of the OWT if $t_{hold}^{HT} = 7200\,sec$ and $P_{cc} = 10\,MPa$. The left and the right columns correspond to the case 1 and 2 respectively.

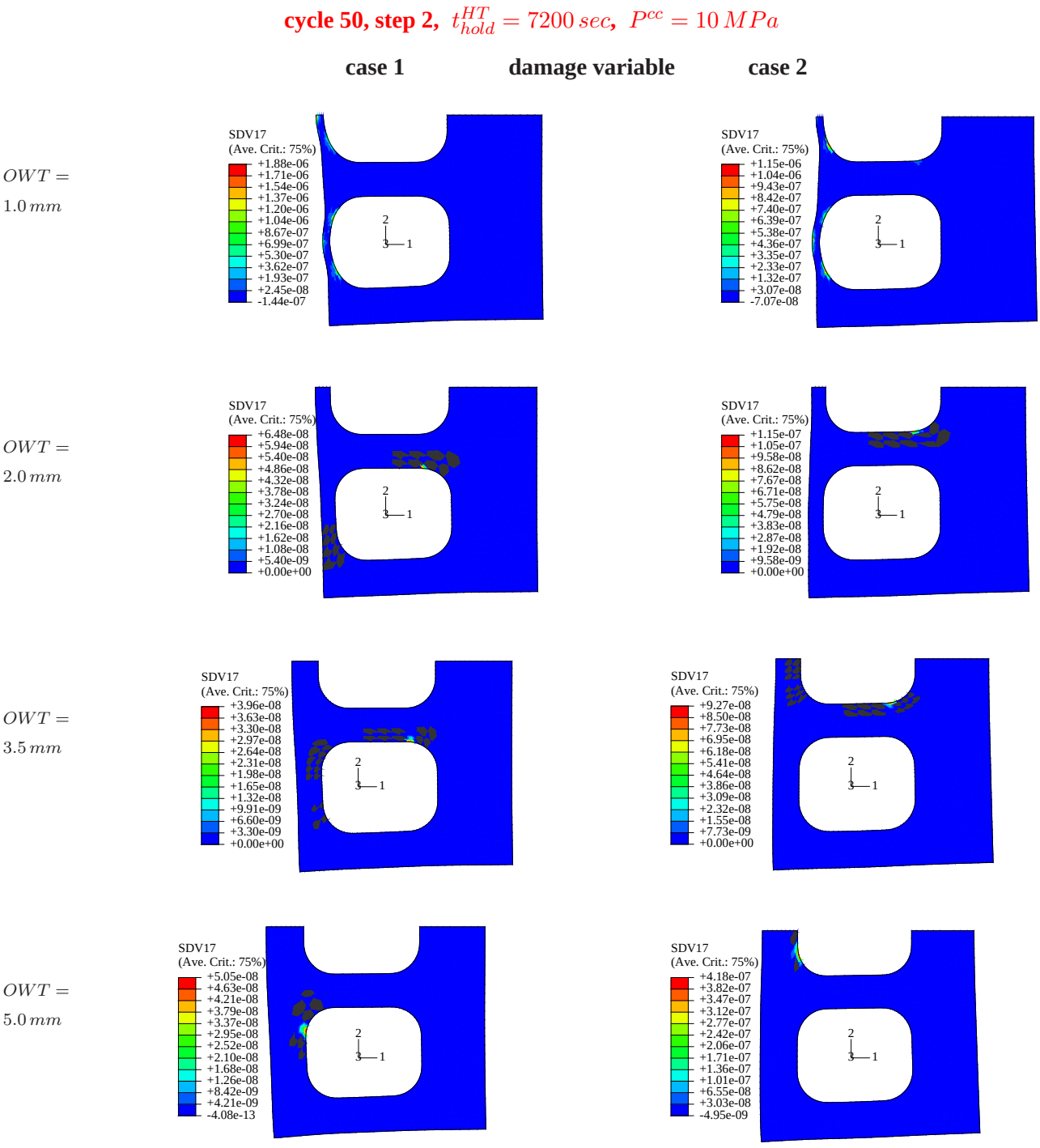

Figure B.11: Distributions of the damage variable after the holding at the HT during the cycle 50 for different values of the OWT if $t_{hold}^{HT} = 7200\,sec$ and $P_{cc} = 10\,MPa$. The left and the right columns correspond to the case 1 and 2 respectively.

B.3 Evolutions of the von Mises Stress, Magnitude of Inelastic Strain and Damage during the first 50 Cycles, $T_1 = 350°C\,(623\,K)$.

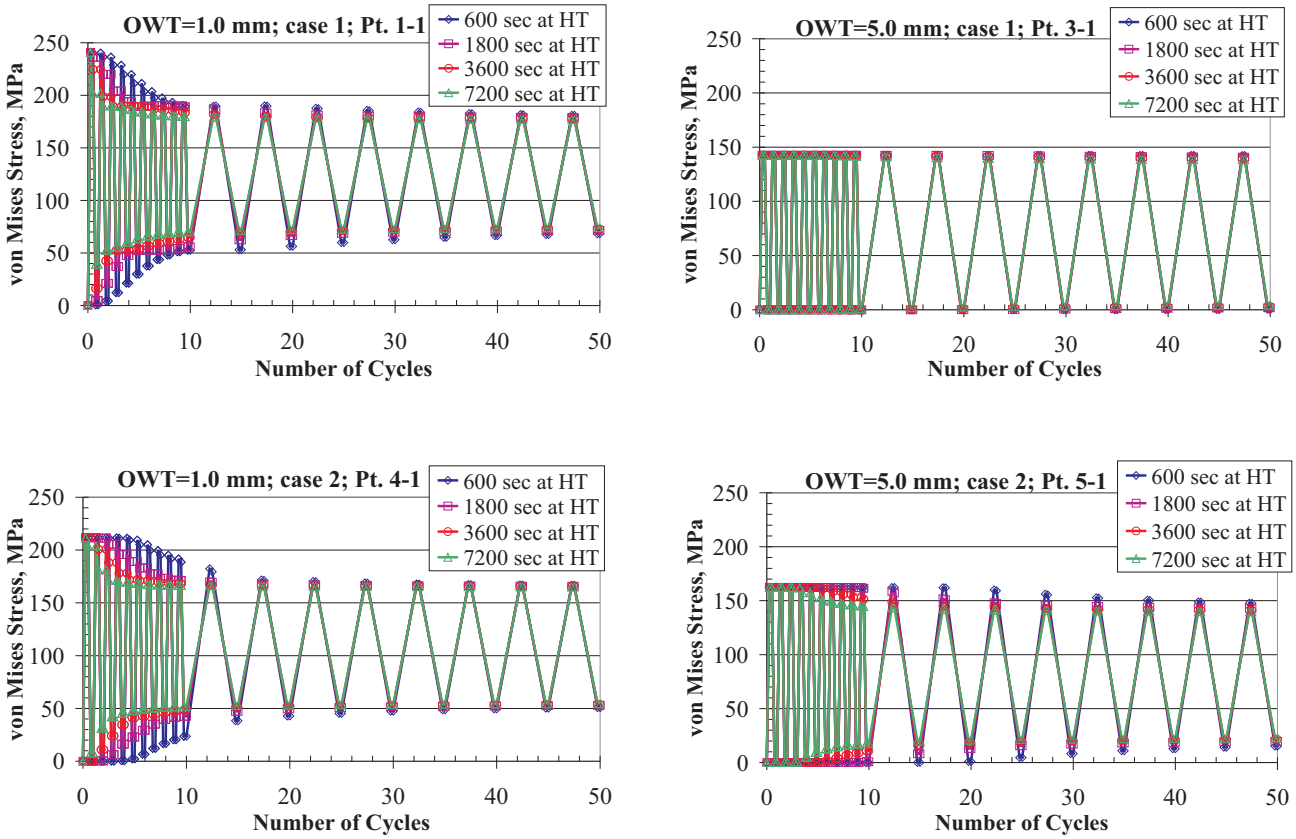

Figure B.12: An evolution of the von Mises stress in the actual critical point during the first 50 cycles with different t_{hold}^{HT}. The upper and the lower rows correspond to the cases 1 and 2 respectively; the left and the right columns correspond to $OWT = 1.0\,mm$ and $OWT = 5.0\,mm$ respectively.

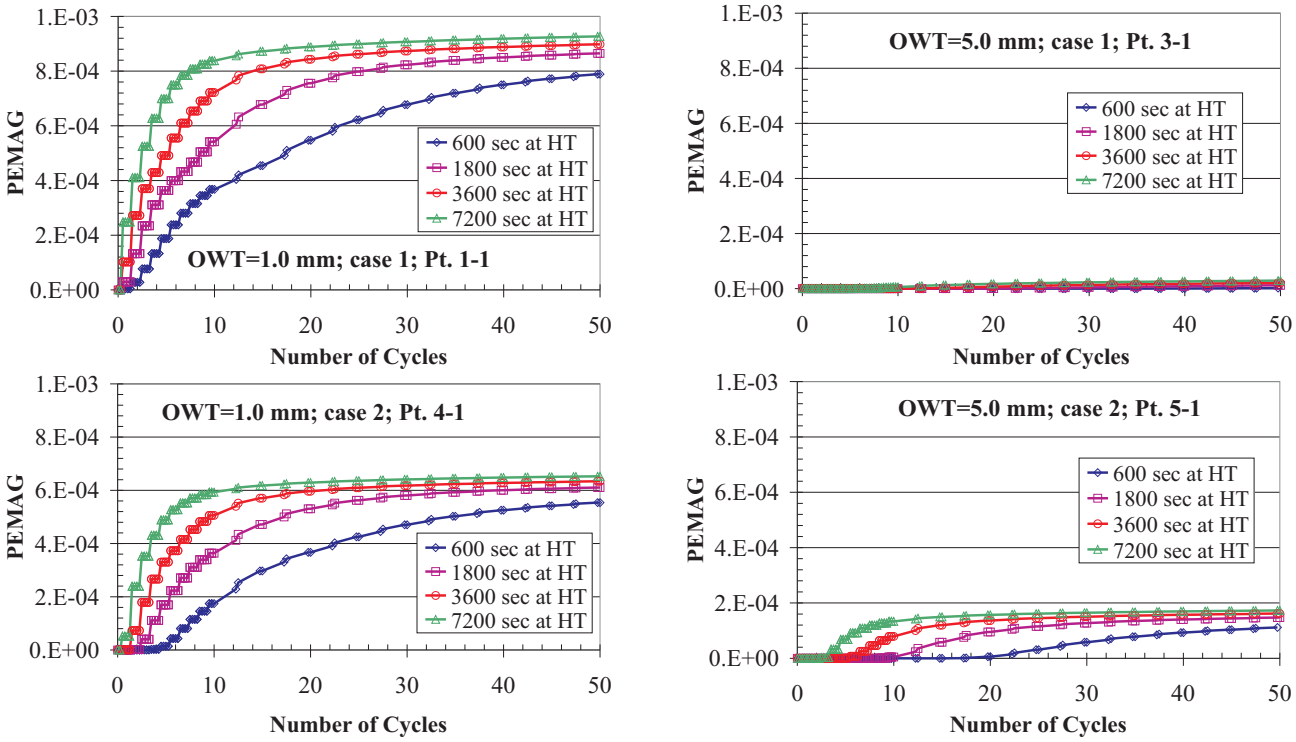

Figure B.13: An evolution of the amount of inelastic strain in the actual critical point during the first 50 cycles with different t_{hold}^{HT}. The upper and the lower rows correspond to the cases 1 and 2 respectively; the left and the right columns correspond to $OWT = 1.0\,mm$ and $OWT = 5.0\,mm$ respectively.

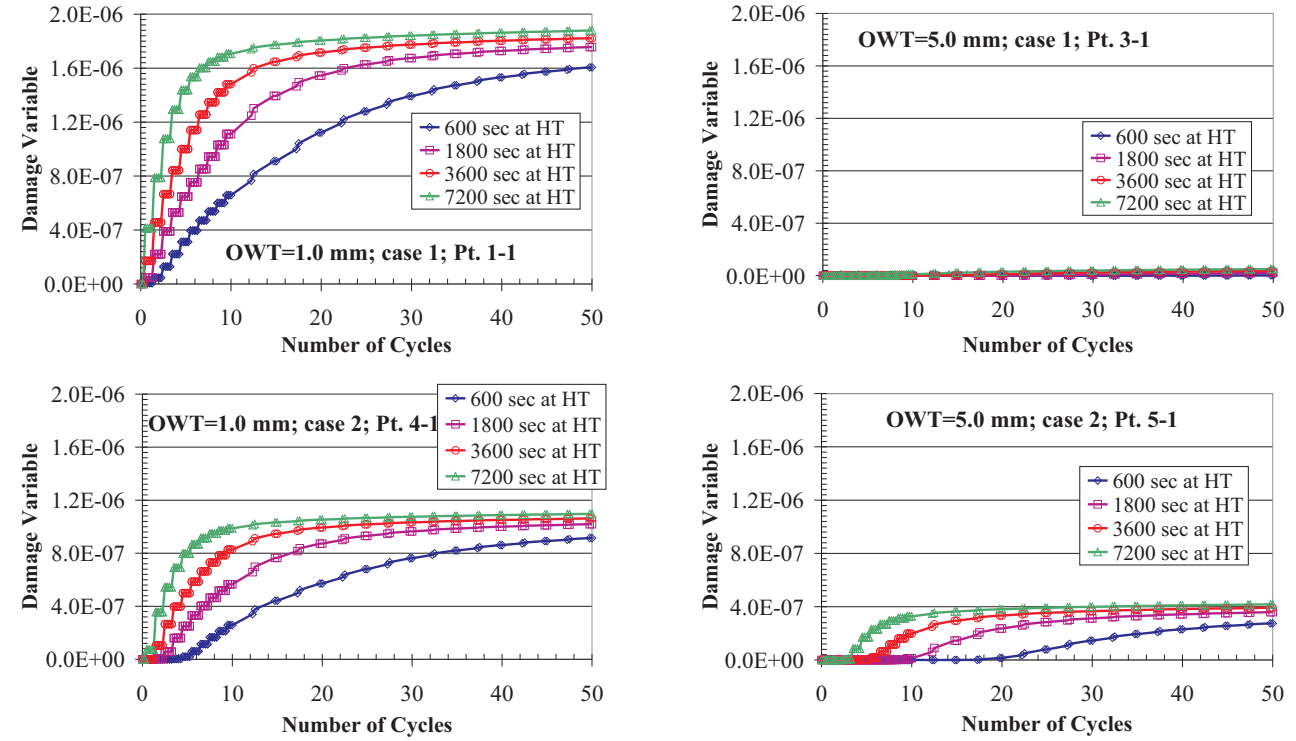

Figure B.14: An evolution of the damage variable in the actual critical point during the first 50 cycles with different t_{hold}^{HT}. The upper and the lower rows correspond to the cases 1 and 2 respectively; the left and the right columns correspond to $OWT = 1.0\,mm$ and $OWT = 5.0\,mm$ respectively.

B.4 Distributions of the von Mises Stress, Accumulated Plastic Strain and Damage Variable during the Cycle 50 for Different Values of P_{cc} and T_1.

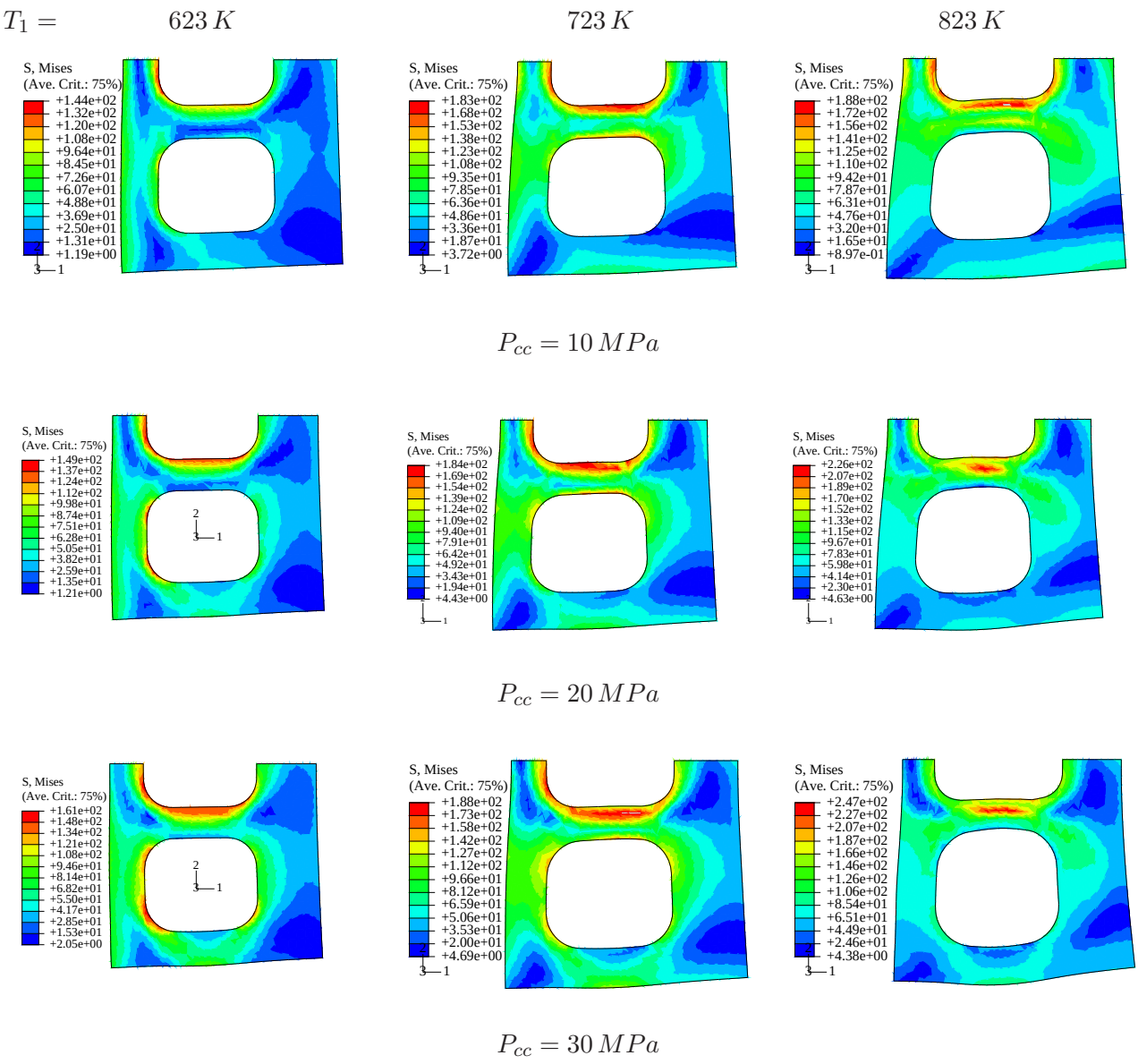

Figure B.15: Distributions of the von Mises stress after the holding at the HT ($t_{hold}^{HT} = 1800\,sec$) during the cycle 50 for different values of T_1 and P_{cc}; $T_2 = 300°C\ \ (573\,K)$ remains thereby constant; all displacements are magnified by factor 100.

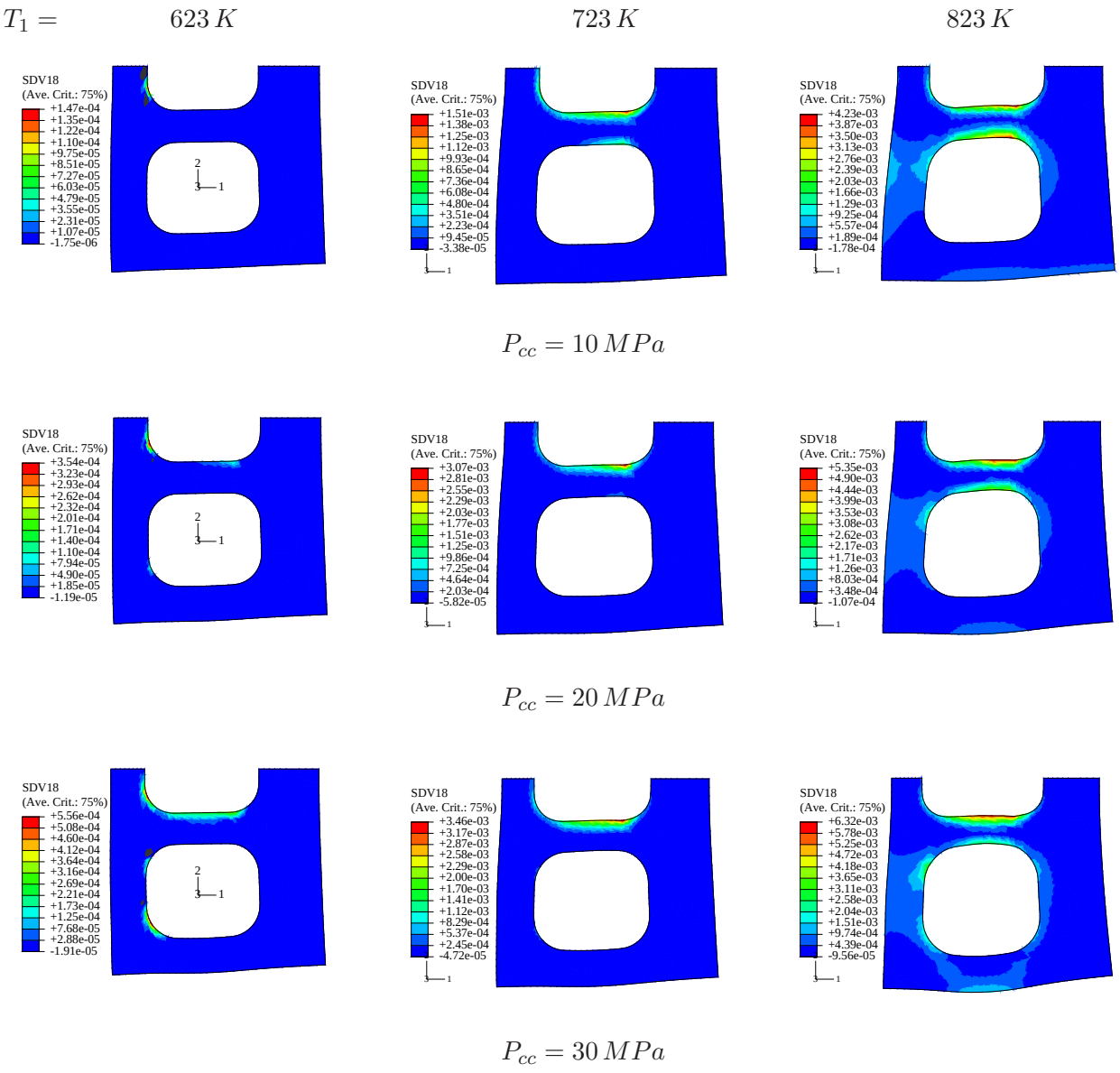

Figure B.16: Distributions of the accumulated plastic strain after the holding at the HT ($t_{hold}^{HT} = 1800\,sec$) during the cycle 50 for different values of T_1 and P_{cc}; $T_2 = 300°C\ \ (573\,K)$ remains thereby constant; all displacements are magnified by factor 100.

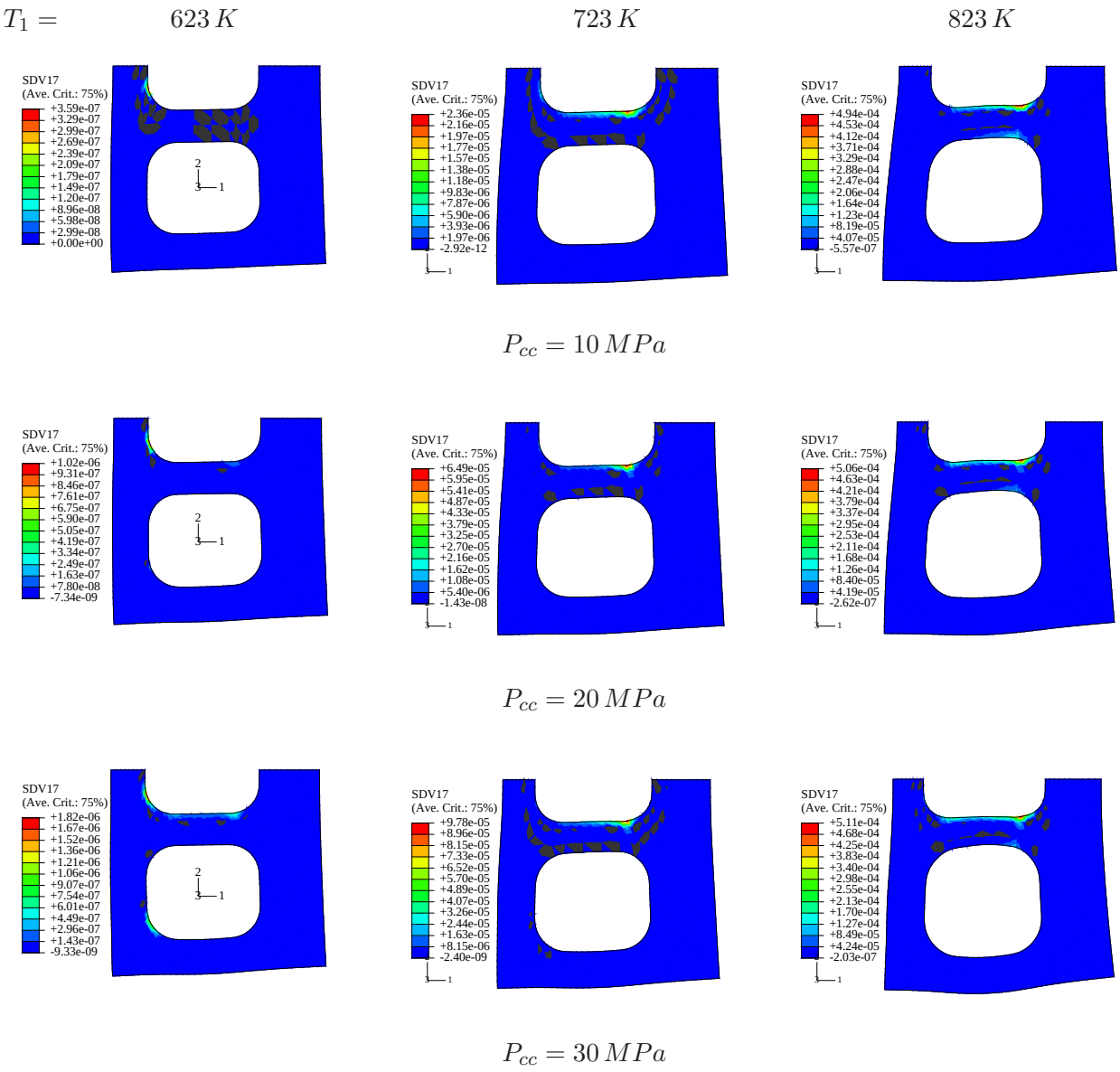

Figure B.17: Distributions of the damage variable after the holding at the HT ($t_{hold}^{HT} = 1800\,sec$) during the cycle 50 for different values of T_1 and P_{cc}; $T_2 = 300°C\ \ (573\,K)$ remains thereby constant; all displacements are magnified by factor 100.

Bibliography

[1] *ITER Structural Design Criteria for In-vessel Components (SDC-IC), ITER Doc. G 74 MA 8 01-05-28 W0.2*. (internal project document distributed to the ITER Participants).

[2] *ABAQUS/Standard User's Manual, v. 6.2*, 2001. Hibbitt, Karlsson & Sorensen Inc.

[3] J. Aktaa. *Kontinuumsmechanische Modellierung der zeitabhängigen Schädigung bei hohen Temperaturen*. PhD thesis, Universität Karlsruhe, 1994. report VDI 20 No. 144, VDI Verlag Düsseldorf.

[4] J. Aktaa, M. G. Horsten, and R. Schmitt. Effects of hold time and neutron irradiation on the low-cicle fatigue behavior of tipe 316-cl and their consideration in damage model. *Nuclear Engng. Design*, 213:111–117, 2002.

[5] J. Aktaa and D. Munz. Modelling of the non-linear deformation and damage behavior of combustor structure materials. In S. Wittig, O. Vöhringer, and S. Kim, editors, *High Intencity Combustors- Steady Isobaric Combustion*, pages 391–416. WILEY-VCH, 2002.

[6] J. Aktaa and B. Schinke. The influence of the hardening state on time dependent damage and its consideration in a unified damage model. *Fatigue Engng. Mater. Struc.*, 19:1143–1151, 1996.

[7] J. Aktaa and R. Schmitt. High temperature deformation and damage behavior of rafm steels under low cycle fatigue loading: experiments and modelling. Fusion Engineering and Design, 2006. corrected proof.

[8] J.-L. Chaboche. Viscoplastic constitutive equations for the description of cyclic and anisotropic behaviour of metals. *Bull. de l'Acad. Polonaise des Sciences, Sc. et Tech.*, 25(1):33–42, 1977.

[9] H. Kiewel, J. Aktaa, and D. Munz. Application of an extrapolation method in thermocyclic failure analysis. *Comput. Methods Appl. Mech. Engrg.*, 182:55–71, 2000.

[10] J. Lemaitre. Evaluation of dissipation and damage in metals submitted to dynamic loading. Proc. I.C.M. 1, Kyoto, Japan, 1971.

[11] J. Lemaitre and J.-L. Chaboche. *Mechanics of Solid Materials*. Cambridge University Press, 1990.

[12] J. R. Rice. Continuum mechanics and thermodynamics of plasticity in relation to microscale deformation mechanisms. In A. S. Argon, editor, *Constitutive Equations in Plasticity*. MIT Press, Cambridge, Massachusetts, 1975.

[13] R. Sunyk and J. Aktaa. Verification of design rules for eurofer under tbm operating conditions. Submitted to J. Nuc. Mat. (special issue).

[14] R. Sunyk and J. Aktaa. Evaluation of material design limits for tbm applications. IEEE/SOFE05 proceedings, 2005. http://216.228.1.34/Conf/sofe05/versions/64291/PID131414.pdf.

[15] K. P. Walker. Research and development for nonlinear structural modelling with advanced time-temperature dependent constitutive relationships, 1981. NASA CR-165533.

[16] M. Weick. private communication, 2004. Forschungszentrum Karlsruhe GmbH.

[17] H. Ziegler. A modification of prager's hardening rule. *Quarterly of Applied Mechanics*, 7:55–56, 1959.